Max-Planck-Institut für Meteorologie
Max Planck Institute for Meteorology

MAX-PLANCK-GESELLSCHAFT

Interannual Climate Variability in the Tropical Indian Ocean: A Study with a Hierarchy of Coupled General Circulation Models

Astrid Baquero Bernal

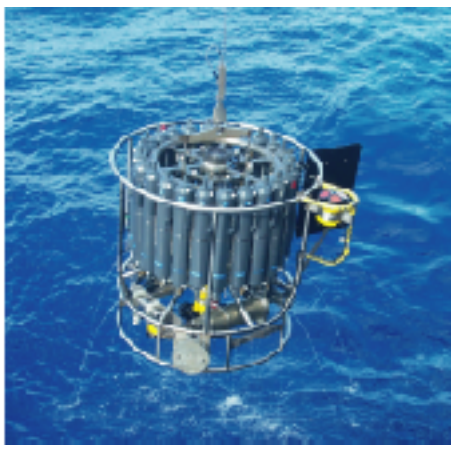

Berichte zur Erdsystemforschung 8/2005

Reports on Earth System Science

Hinweis

Die Berichte zur Erdsytemforschung werden vom Max-Planck-Institut für Meteorologie in Hamburg in unregelmäßiger Abfolge herausgegeben.

Sie enthalten wissenschaftliche und technische Beiträge, inklusive Dissertationen.

Die Beiträge geben nicht notwendigerweise die Auffassung des Instituts wieder.

Die "Berichte zur Erdsystemforschung" führen die vorherigen Reihen "Reports" und "Examensarbeiten" weiter.

Notice

The Reports on Earth System Science are published by the Max Planck Institute for Meteorology in Hamburg. They appear in irregular intervals.

They contain scientific and technical contributions, including Ph. D. theses.

The Reports do not necessarily reflect the opinion of the Institute.

The "Reports on Earth System Science" continue the former "Reports" und "Examensarbeiten" of the Max Planck Institute.

Anschrift / Address

Max-Planck-Institut für Meteorologie
Bundesstrasse 53
20146 Hamburg
Deutschland

Tel.: +49-(0)40-4 11 73-0
Fax: +49-(0)40-4 11 73-298
Web: www.mpimet.mpg.de

Layout:

Bettina Diallo, PR & Grafik

Titelfotos:
vorne:
Christian Klepp - Jochem Marotzke - Christian Klepp
hinten:
Katsumasa Tanaka - Christian Klepp - Clotilde Dubois

Berichte zur Erdsytemforschung 8/2005

Interannuale Klimavariabilität im tropischen Indischen Ozean: Eine Untersuchung mit einer Hierarchie von globalen gekoppelten Ozean-Atmosphären-Modellen

Interannual Climate Variability in the Tropical Indian Ocean: A Study with a Hierarchy of Coupled General Circulation Models

Dissertation zur Erlangung des Doktorgrades der Naturwissenschaften
im Fachbereich Geowissenschaften der Universität Hamburg
vorgelegt von

Astrid Baquero Bernal
aus Bogotá, Kolumbien

Hamburg 2004

Reports on Earth System Science 8/2005

ISSN 1614-1199

Astrid Baquero Bernal
Max-Planck-Institut für Meteorologie
Bundesstrasse 53
20146 Hamburg
Germany

Als Dissertation angenommen
vom Fachbereich Geowissenschaften der Universität Hamburg

auf Grund der Gutachten von
Prof. Dr. Klaus Fraedrich
und
Prof. Dr. Mojib Latif

Hamburg, den 15.Dezember 2004
Professor Dr. Helmut Schleicher
Dekan des Fachbereiches Geowissenschaften

ISSN 1614-1199

Interannual Climate Variability in the Tropical Indian Ocean: A Study with a Hierarchy of Coupled General Circulation Models

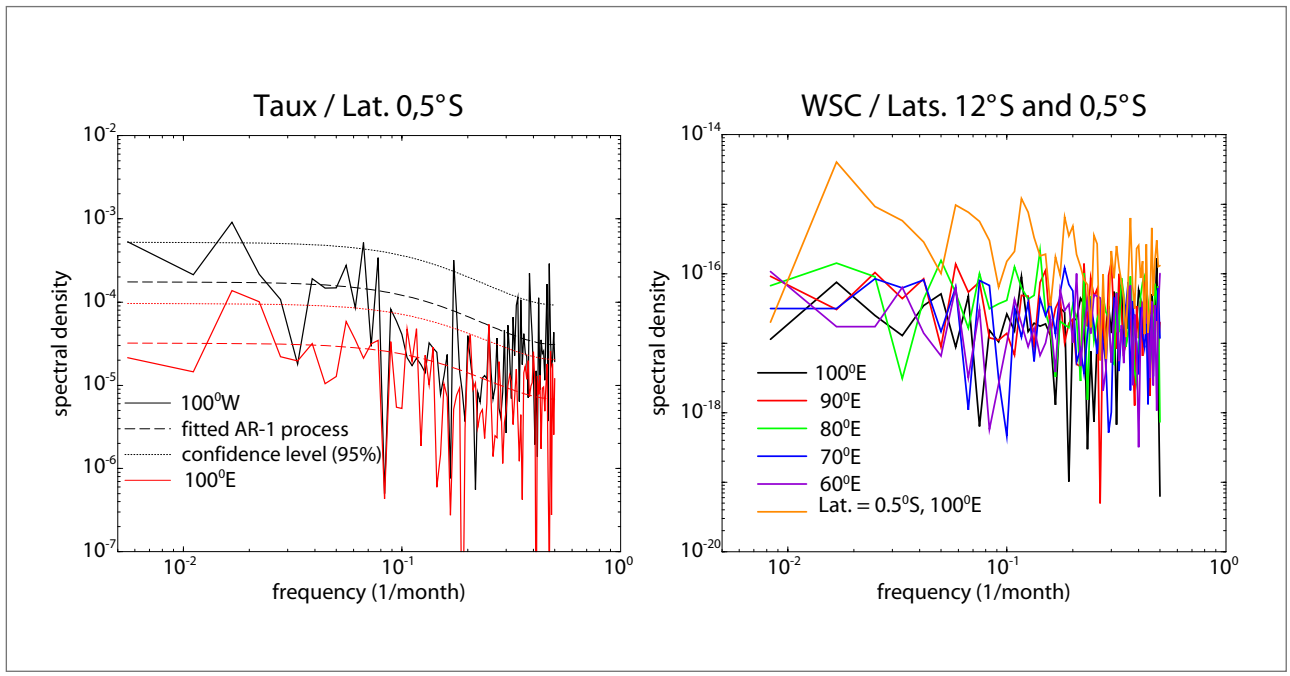

Astrid Baquero Bernal

Hamburg 2004

To Nelly Bernal, my mother

Primero estaba el Mar.
Todo estaba obscuro. No había Sol,
ni Luna, ni gente, ni animales, ni plantas.
El Mar estaba en todas partes.
El Mar era la Madre,
la Madre no era un ser vivo ni cosa alguna.
Ella era espíritu de lo que iba a venir
y ella era pensamiento y memoria.
Tribu Kogui

In the beginning there was blackness. Only the Sea.
In the beginning, there was no sun,
no moon, no people, no animals, no plants.
The Sea was everywhere.
The Sea was the Mother,
the Mother was not a living being,
she was not anything, nothing at all.
She was, when she was -Spirit.
She was memory and possibility.
Kogui Tribe

Zuerst war das Meer.
Alles war dunkel. Es gab keine Sonne,
keinen Mond, keine Menschen,
keine Tiere, keine Pflanzen.
Das Meer war überall.
Das Meer war die Mutter, die Mutter war kein
lebendes Wessen noch irgendwas.
Sie war der Geist alles Kommenden,
und sie war Gedanke und Erinnerung.
Volksstamm Kogui

Contents

Abstract

The Indian Ocean shows significant climate variability at interannual timescales. This variability is affected by the El Niño–Southern Oscillation (ENSO) phenomenon. A hierarchy of coupled model simulations is used as well as observational datasets and reanalysis products to investigate the role ENSO plays in determining the interannual climate variability in the Indian Ocean and to investigate the spatial and temporal characteristics of the ENSO–independent climate variability. The hierarchy of coupled model simulations comprises three experiments. Two experiments are conducted with the ECHO-G model, which is a state–of–the–art ocean–atmosphere general circulation model (CGCM). The first experiment with ECHO-G is a standard integration, which serves as a control integration. The second experiment with ECHO-G is similar to the control experiment, but the interannual ocean–atmosphere interactions have been inhibited in the tropical Pacific Ocean, so that in this experiment the ENSO signal is excluded by definition. The third experiment is conducted with a fixed–depth mixed–layer model coupled to the same atmosphere model that has been used in the two experiments with ECHO-G. This integration allows the investigation of the role of ocean dynamics in the generation of interannual sea surface temperature (SST) variability.

It is shown that the variability of several atmospheric and oceanic fields in the Indian Ocean region, including SST, is consistent with a cycle only if ENSO is included in the simulation. The ENSO signature in the Indian Ocean includes both a dynamical and a thermodynamical response. ENSO influences the Indian Ocean at two different interannual timescales and provides conditions favorable for coupled ocean–atmosphere interactions in the Indian Ocean. In contrast, the climate variability that is independent of ENSO shows a response of the ocean to the atmospheric forcing that is not significantly more energetic than expected from a stochastic forcing approach, thereby reflecting either a passive oceanic response or weak coupling in the ENSO–independent Indian Ocean variability.

Zusammenfassung

Der indische Ozean weist eine signifikante interannuale Klimavariabilität auf. Diese Klimavariabilität wird durch das El Niño–Southern Oscillation (ENSO) Phänomen beeinflußt. Eine Hierarchie von gekoppelten Ozean–Atmosphäre Modellsimulationen, Beobachtungsdatensätze und Reanalyse–Produkte werden verwendet, um zu erforschen, welche Rolle ENSO in der interannualen Klimavariabilität des Indischen Ozeans spielt und was die räumlichen und zeitlichen Eigenschaften der ENSO–unabhängigen Klimavariabilität sind. Die Hierarchie von gekoppelten Ozean–Atmosphäre Modellsimulationen besteht aus drei Experimenten. Zwei dieser Experimente wurden mit dem ECHO-G Modell durchgeführt. ECHO-G ist ein gekoppeltes Ozean–Atmosphäre Zirkulationsmodell, das dem neuesten Stand der Technik entspricht. Das erste Experiment mit ECHO-G ist eine Standardintegration, die als Kontrolllauf dient. Das zweite Experiment mit ECHO-G ist der Kontrollintegration ähnlich, aber die interannuale Ozean–Atmosphäre Interaktionen werden im tropischen Pazifik unterbunden, so daß es per Definition kein ENSO Signal in diesem Experiment gibt. Das dritte Experiment ist eine Simulation mit einem "mixed-layer" Ozeanmodell mit konstanter Deckschichttiefe, das an das gleiche Atmosphäre Modell gekoppelt wird, wie es in den beiden ECHO-G Experimenten mit ECHO-G verwendet wird. Diese Integration erlaubt die Untersuchung der Rolle der Ozeandynamik für die Erzeugung der interannualen Variabilität der Meeresoberflächentemperatur (mit der englischen Abkürzung SST für sea surface temperature).

Es wird gezeigt, daß die Variabilität verschiedener atmosphärischer and ozeanischer Felder in der Region Indischer Ozean, einschließlich der SST, nur dann konsistent mit einem zyklischen Ablauf ist, wenn ENSO in der Simulation enthalten ist. Das ENSO–Signal im Indischen Ozean schließt sowohl eine dynamische als auch eine thermodynamische Reaktion ein. ENSO beeinflußt den Indischen Ozean auf zwei unterschiedlichen interannualen Zeitskalen und führt zu Bedingungen, die vorteilhaft für die gekoppelten Ozean–Atmosphäre–Interaktionen sind. Die Experimente erlauben eine Unterscheidung zwischen ENSO und ENSO–unabhängiger Variabilität. Bei letzterer ist die Reaktion des Ozeans auf den atmosphärischen Antrieb nicht energetischer als die von einem stochastischen Antrieb erwartet würde. Dadurch zeigt diese ENSO–unabhängige Reaktion, daß sie entweder einer passiven ozeanischen Reaktion oder einer schwachen Ozean–Atmosphäre Kopplung entspricht.

Chapter 1

Introduction

The study of the climate variability of the Indian Ocean region has important implications since several hundred million people inhabit the region and the economies of many of the surrounding countries depend strongly on agriculture. On interannual timescales, the climate over the Indian Ocean region is influenced by El Niño–Southern Oscillation (ENSO) phenomenon. For instance, Webster et al. (1998), showed that some periods of rice-production deficit in India are associated with the El Niño years in the Pacific Ocean while some abundant years are associated with "cold" ENSO extrems in the Pacific.

The ENSO phenomenon is the strongest interannual climate fluctuation and has its largest signature in and over the tropical Pacific. ENSO is recognized as a coupled ocean–atmosphere phenomenon and is characterised by an irregular interannual oscillation of sea surface temperature (SST) in the tropical Pacific. The warm phase is referred to as "El Niño", while the cold phase is referred to as "La Niña" (Philander 1990). El Niño is associated with a large-scale weakening of the trade winds and warming of the surface layers in the eastern and central equatorial Pacific Ocean. During El Niño, unusually high atmospheric sea level pressures develop in the western tropical Pacific and Indian Ocean regions, and unusually low sea level pressures develop in the southeastern tropical Pacific (McPhaden et al. 1998, and references therein).

Although ENSO originates in the tropical Pacific, it has an effect not only upon regional climate but also upon global climate (e.g. Ropelewski and Halpert 1989; Glantz and Katz 1991). ENSO is associated with shifts in the location and intensity of deep convection and rainfall in the tropical Pacific. These shifts in the pattern of deep convection also affect the general circulation of the atmosphere and extend the impacts of ENSO to other

tropical ocean basins and to midlatitudes. The impacts include changes in temperature, storm tracks, and rainfall all over the globe, often producing droughts in some regions and floods in other regions (McPhaden et al. 1998; Wallace et al. 1998; Trenberth et al. 1998, and references therein). Thus, tropical and extratropical regions have identifiable signals associated with both phases of ENSO as a result of changes in the atmosphere and surface fluxes. In addition to this, in tropical and extratropical oceans there is a direct ENSO-related signal through wave propagation such as Kelvin wave propagation along the west coast of the Americas. The ENSO–response in the Indian Ocean region includes anomalous easterly winds near the equator and a basin-wide warming (Klein 1999; Lau and Nath 2000).

The most widely accepted explanation for ENSO dynamics is that it arises through an ocean-atmosphere interaction within the tropical Pacific basin. There is an interaction between the trade winds and the ocean dynamics, which maintains both a shallow thermocline and upwelling in the eastern Pacific. The ocean, with its longer timescales of adjustment, provides the memory that produces the turnabout between warm and cold phases (Neelin et al. 1998, and references therein).

A prominent aspect of ENSO is its quasiperiodicity. This can be inferred, for instance, from spectra of typical ENSO indices, such as the time series of eastern equatorial Pacific SST. This index exhibits enhanced variability at interannual timescales, with a dominant peak at around 3 to 5 years and a secondary quasi–biennial peak (Rasmusson and Carpenter 1982). The existence of these peaks suggests that ENSO may be predictable (Latif et al. 1998) and indicates that ENSO is based on a cycle (Neelin et al. 1998). Different competing hypotheses were offered to explain the temporal nature of ENSO and the role of noise in ENSO dynamics. One hypothesis assigns a fundamental role of weather noise to the existence of ENSO (Penland and Sardeshmukh 1995). Other hypotheses propose that ENSO is an unstable mode leading to a self-sustained cycle but with noise producing the irregularity (e.g. Jin et al. 1996). Still, there is no agreement about the role of weather noise and both hypotheses seem to be plausible (Neelin et al. 1998).

Many advances in understanding and predicting the tropical oceans and the global atmosphere have been made through international cooperation under programs such as the Tropical Ocean-Global Atmosphere (TOGA) program. However, there are limitations with regard to the availability of sufficiently long observational datasets for the Indian

Ocean region, even for studies of variability at interannual timescales, and many issues are still unresolved. The two most important questions are: what mechanisms produce the variability in the Indian Ocean and what is their relationship with ENSO? Two recent studies by Saji et al. (1999) and Webster et al. (1999) proposed that large-scale coupled ocean-atmosphere interactions cause interannual climate variability in the tropical Indian Ocean and that this variability is independent of ENSO. This variability, known as the Indian Ocean dipole, is characterized by an east-west equatorial SST gradient with negative SST anomalies offshore Sumatra and positive SST anomalies in the western Indian Ocean, anomalous easterly surface winds along the equator, increased rainfall over the western tropical Indian Ocean, and decreased rainfall over the oceanic tropical convergence zone. Saji et al. (1999) argue that the reduced eastward transport of mass and heat by the equatorial current is important for the coupled variability. On the other hand, Webster et al. (1999) argue that equatorial Rossby and Kelvin ocean waves are associated with the intensification, duration and demise of the temperature anomaly in a dipole event. Additionally, Saji et al. (1999) propose that the Indian Ocean dipole has a biennial periodicity and Webster et al. (1999) proposed that the SST gradient has long-period oscillations at interannual timescales. Both propositions imply potential predictability for SST and rainfall. The review presented in the preceding paragraphs concerns the interannual variability related to equatorial processes. However, variability in the tropical South Indian Ocean could also imply coupled ocean-atmosphere interactions at interannual timescales.

Another perspective of the interannual climate variability in the tropical Indian Ocean was proposed by Xie et al. (2002). They showed that curl associated with anomalous easterlies force downwelling Rossby waves with a maximum amplitude around 10°S, which interact with the atmosphere, and that these waves are forced by ENSO and Sumatra SST variability.

Many questions emerge from the studies mentioned above, for example:

- Is the east-west dipole an unequivocal sign of equatorial coupled ocean-atmosphere variability?

- What is the spectral signature of the SST anomalies, and is it consistent with a cycle?

- Given that the ENSO phenomenon involves the Indo-Pacific region, how is the Indian Ocean variability affected by ENSO?
- What is the nature of the coupled ocean-atmosphere interactions in the tropical Indian Ocean?
- What mechanisms can generate Rossby waves around 10°S, and can they be described as stochastically forced?

The objective of this thesis is to contribute to answer these questions. In order to do so, two simulations with the Coupled General Circulation Model (CGCM) ECHO-G (Legutke and Voss 1999) were used. The simulations will be described in chapter 2.

Each of the chapters 3 to 5 is designed to be an independent and full paper, thus some repetitions may inevitably occur in data and method descriptions. Note that the references from all chapters will be gathered together into a reference list at the end of the thesis.

Chapter 3 is focused on the interannual SST variability in the Indian Ocean, its relationship with ENSO, and its spectral signature. Chapter 4 is dedicated to interannual variability in general, including the mechanisms behind coupled ocean-atmosphere variability and Rossby waves and how ENSO influences them. Chapter 5 concentrates on the study of the variability related to Rossby waves around 10°S. In particular, it is explored how well a stochastic model of wind-driven Rossby waves fits to the observations and to the simulated variability in an experiment without ENSO signal. Conclusions and an outlook for future work are given in chapter 6.

Chapter 2

The ECHO-G Simulations

The analyses presented in the following chapters are mostly based on simulations with the coupled general circulation model (CGCM) ECHO-G. The CGCM ECHO-G consists of version 4 of the Hamburg atmosphere general circulation model, ECHAM4 (Roeckner et al. 1996), and the global version of the Hamburg Ocean Primitive Equation general circulation model, HOPE–G (Wolff et al. 1997), which is a primitive–equation z–level ocean model, and incorporates a dynamic–thermodynamic sea–ice model with snow cover. The component models are coupled by using the OASIS coupling software developed at CERFACS (Terray et al. 1998). The ECHO-G model is described in detail in Legutke and Voss (1999).

For the ECHO-G simulations presented in this study, ECHAM4 employs a 19-level hybrid sigma-pressure vertical coordinate system, and a horizontal resolution of T30, which corresponds approximately to a horizontal gridpoint distance of 3.75°. HOPE-G employs a zonal resolution of 2.8° in the whole domain. The meridional resolution is 2.8° in the extratropics, and is gradually increased until it reaches 0.5° within 10° of the equator. The increased resolution in low latitudes is intended for a better representation of equatorial dynamics. The vertical resolution is 20 levels. The atmosphere component model passes heat, fresh water and momentum to the ocean and receives surface conditions. These conditions are SST, sea-ice concentration, sea-ice thickness and snow depth. Annual mean heat and freshwater fluxes, as diagnosed from a 155-year coupled spin–up integration, are used as flux corrections. However, no momentum flux corrections are used. The ECHO-G model has been used in studies of paleoclimatic (Zorita et al. 2002) and Antarctic variability (Marsland et al. 2003).

As it will be shown in the following chapters, interannual variability in the tropical Indian Ocean can be affected by both local and remote factors. One of the remote factors is ENSO. To identify the relative effectiveness of different mechanisms, it is necessary to separate local and remote effects. For this purpose, a coupling strategy is employed in the ECHO-G model where the effects of the air-sea interactions in the tropical Indian Ocean are isolated from the ENSO influence by prescribing climatological SST over the tropical Pacific Ocean. In particular, the SSTs are prescribed in the Pacific region that stretches from 40°N to 40°S. This was realized by replacing the actual SST field simulated by the ocean component by a time-constant SST field before passing it to the atmosphere component. This simulation will be called non-ENSO experiment in the following.

In the folllowing chapters, the tropical Indian Ocean climate variability will be examined in two simulations with the ECHO-G model One simulation is the non-ENSO experiment and the other is a control experiment in which air-sea interactions are allowed everywhere (control experiment).

Chapter 3

Interannual Variability of the Sea Surface Temperature in the Tropical Indian Ocean

3.1 Introduction

Since the interannual variability in the tropical Indian Ocean sea surface temperature (SST) is much weaker than that in the Pacific, it has not received as much attention and is less well understood than the variability in the Pacific. The latter is dominated by the El Niño/Southern Oscillation (ENSO) phenomenon. Although ENSO originates in the tropical Pacific, it affects the global climate. Several investigations have suggested that ENSO also influences the Indian Ocean in different ways (Latif and Barnett 1995; Meyers 1996; Tourre and White 1997; Chambers et al. 1999; Venzke et al. 2000). Other studies have suggested that a significant fraction of the SST variability is related to ENSO but that there are other factors that are also important in determining the SST anomalies (SSTAs) (Reverdin et al. 1986; Murtugudde and Busalacchi 1999). Recently, Saji et al. (1999) and Webster et al. (1999) have proposed the existence of a coupled ocean-atmosphere mode that originates in the Indian Ocean climate system, which has a characteristic seasonal phase locking and may induce anomalous rainfall over eastern Africa and Indonesia. Furthermore, it is argued that the mode is independent of ENSO. The mode is referred to as the "Dipole Mode (DM)". The DM spatial structure they

proposed is characterized by SSTAs of one sign in the southeastern tropical Indian Ocean (SETIO: 90°E - 110°E, 10°S - 0°) and SSTAs of the opposite sign in the western tropical Indian Ocean (WTIO: 50°E - 70°E, 10°S - 10°N). However, the existence of a dipole as a mode of SST variability independent of ENSO is currently a subject of discussion. Allan et al. (2001) show evidence that supports the dependence, rather than independence, of ENSO and Indian Ocean dipole.

In this chapter the interannual variability in the tropical Indian Ocean SST and its relationship to ENSO are investigated in more detail. SST observations and results from a series of coupled model integrations are used. Correlation analyses using area-averaged anomalies were performed and the technique of Principal Oscillation Patterns (POPs) was used to remove the ENSO signal. The POP analysis is designed to extract the characteristic space-time variations within a complex multi-dimensional system (Hasselmann 1988; von Storch et al. 1988; Xu and von Storch 1990). The modeling and observational results presented in the following suggest that, associated with the ENSO cycle, there is a dipole-like structure in the tropical Indian Ocean that oscillates. Besides this, a dipole-like variability exists in the Indian Ocean independent of ENSO. However this type of variability does not oscillate and might be understood within a stochastic framework where there is a red-noise response of the SST to surface heat flux forcing.

The chapter is organized as follows. The results of the analyses of the observed SSTs are presented in section 3.2. The results of the coupled model simulations are described in section 3.3. The chapter is concluded with a discussion of the main findings in section 3.4. The work presented in this chapter has been published in the Journal of Climate (Baquero-Bernal et al. 2002).

3.2 SST observations

The following analyses are based on the monthly SST dataset of the Hadley Center for Climate Prediction and Research (Folland et al. 1999). Although the dataset covers the period 1870 to 1998, only the period 1949 to 1998, which is commonly believed to be the most reliable period, is analyzed. The SSTAs were calculated by subtracting the mean annual cycle and the linear trend at each grid point. This procedure was used for the analyses of the observations and simulations. The analysis will be restricted to the region

from 40°E to 60°W and from 30°S to 30°N, which corresponds to the tropical Indian and Pacific Oceans. For the calculation of the correlations between global and box-averaged SSTAs, mean seasonal values are used. For each correlation map the 95% significance level is calculated by applying a t-test. The estimation of the number of degrees of freedom was performed based upon the approximation by Zwiers and von Storch (1995). Additionally, a POP analysis based on monthly values was performed in order to identify the ENSO-related SST variability and to remove it from the full observational dataset.

3.2.1 Analysis considering all seasons

The correlations of the Indo-Pacific SSTAs with box averaged SSTAs in SETIO and WTIO are shown in Fig. 3.1. The WTIO box shows significant correlations with equatorial SSTAs in the Pacific Ocean, but it has no negative correlation with the anomalies in SETIO (Fig. 3.1a). The SETIO box does not show either any significant positive or negative correlation with the SSTAs in WTIO, and the correlations with the SSTAs in the Pacific are smaller. Both correlation maps (Fig. 3.1a and b) lead to the conclusion that the SSTAs in SETIO and in WTIO are not significantly negatively correlated with each other at lag zero, which is consistent with the results of Dommenget and Latif (2002). Additionally, lagged cross-correlation analyses between the SSTAs in SETIO and those in WTIO were performed. Maximum cross-correlation (r=0.43) occurs when the SST variations in SETIO lag those in WTIO by 1 season. Higher correlations are found when the cross-correlation analysis is performed with respect to the Niño3 time series. Maximum cross-correlation (r=0.65) takes place when the SSTAs in the western Indian Ocean lag those of the eastern Pacific by about 1 season, which is consistent with the results of Venzke et al. (2000). Maximum cross correlation (r=0.48) is obtained when the SSTAs in the eastern Indian Ocean lag those of the eastern Pacific by 2 seasons. This lag of 2 seasons is consistent with the fact that the SSTAs in SETIO lag those in WTIO by 1 season. At lag zero, the correlation between WTIO and Niño3 time series is positive and close to the maximum value of about 0.60. It should be noted that the correlation between the SSTAs in SETIO and Niño3 at lag zero is also positive.

All seasons:

a) Observations, correlation with western box

b) Observations, correlation with eastern box

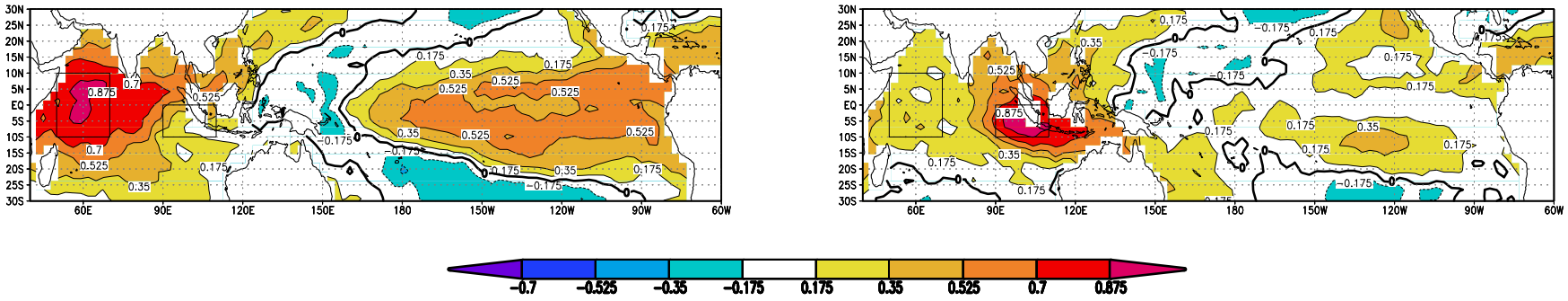

Figure 3.1: Correlation of (a) WTIO box-averaged SST anomalies, and (b) SETIO box-averaged SST anomalies with Indo-Pacific SST anomalies for all seasons. SST anomalies from the Hadley Center observational dataset, 1949-1998. Correlations exceeding 0.31 for (a) and 0.30 for (b) are significant at the 95% confidence level.

Boreal fall season (SON):

a) Observations, correlation with western box

b) Observations, correlation with eastern box

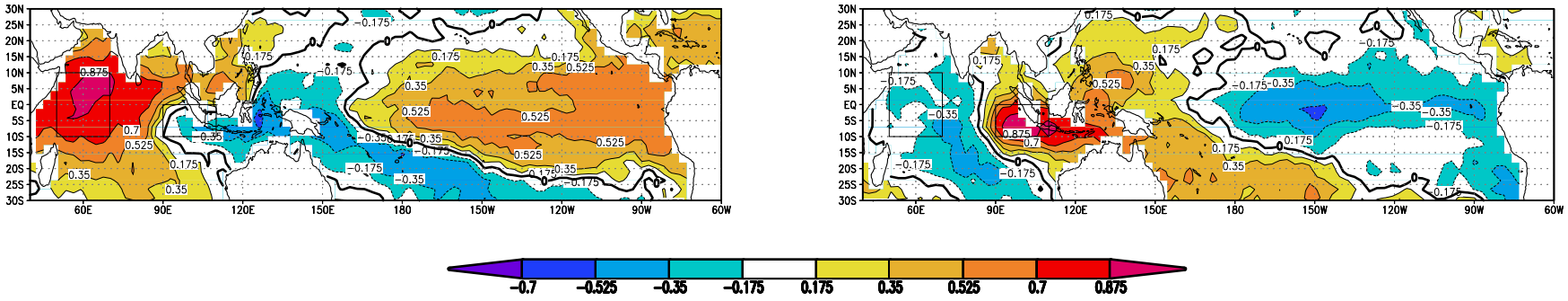

Figure 3.2: Correlation of (a) WTIO box-averaged SST anomalies, and (b) SETIO box-averaged SST anomalies with Indo-Pacific SST anomalies for SON. SST anomalies from the Hadley Center observational dataset, 1949–1998. Correlations exceeding 0.27 for (a) and (b) are significant at the 95% confidence level.

In summary, the results of the correlation analyses and the cross-correlation analyses with respect to the SSTA in the eastern Pacific (Niño3) reveal tha the SST variability in the Indian Ocean is strongly remotely forced by the ENSO phenomenon. Furthermore, a dipole-like mode can not be identified if all seasons are considered.

3.2.2 Seasonal analyses

In the next step, correlation maps for every season were computed separately (like those shown in Fig. 3.1). No negative correlation was found between the SSTAs in SETIO and WTIO neither in winter nor in spring (not shown). For the boreal summer season, there is a very weak negative correlation between the SSTAs in the WTIO and those near the western coast of Indonesia and the north-western coast of Australia (not shown). Some stronger cross Indian Ocean gradient, however, was found in boreal fall. More importantly, this is the season when a strong correlation between the surface westerlies over the equatorial Indian Ocean and the rainfall at the coast of East Africa can be found (Hastenrath et al. 1993). Accordingly, the boreal fall season (SON) will be considered in detail.

3.2.3 Analysis for SON

For the boreal fall season the SSTAs in WTIO show negative correlations with those in the eastern Indian Ocean, but they are restricted to a small region (Fig. 3.2a). The SETIO SSTAs do show negative correlations with those in the central Indian region, which are strongest south of the equator (Fig. 3.2b). Both correlation maps, however, show that the SSTAs in SETIO and in WTIO are not strongly negatively correlated with each other. Furthermore, the SSTAs in the two boxes, SETIO and WTIO, are strongly correlated with the SSTAs in the Pacific.

Figure 3.3 shows the composites for El Niño and La Niña events. Figure 3.3a shows the composite for the six recent El Niño events (1957, 1965, 1972, 1982, 1986 and 1997) and Fig. 3.3b that for the seven recent La Niña events (1955, 1970, 1971, 1973, 1975 and 1988). ENSO-related variability in the Indian Ocean in the boreal fall season looks like a seesaw: for the El Niño events, there are positive SST anomalies west of 80°E and negative anomalies east of 80°E. The situation is reversed during La Niña conditions, but

Observations:

a) Composite for SON for El Niño b) Composite for SON for La Niña

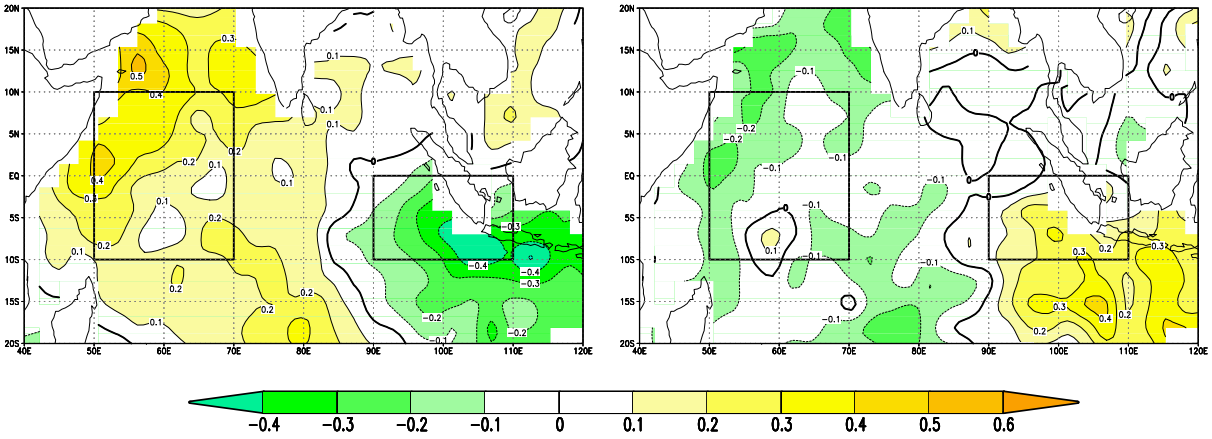

Figure 3.3: Composites for SON for El Niño and La Niña events. (a) Composite of the SST anomalies in SON for the six recent El Niño events. (b) Composite of the SST anomalies in SON for the six recent La Niña events. Units are given in °C.

the magnitude of the anomalies is smaller in the western region. Figs. 3.2 and 3.3 show that ENSO-related variability in the tropical Indian Ocean in SON commonly has a dipole appearance.

3.2.4 ENSO-removed analyses

The aforementioned analyses may be influenced by the presence of the strong ENSO signal. In this section, therefore, the ENSO signal is removed prior to the correlation analyses. There is no unique way to do this. Here, the leading POP mode was subtracted from the monthly SSTA since it includes the ENSO signal as described below. Seasonal mean values were then computed from the residual dataset.

The POP analysis of the monthly SSTAs revealed one dominant POP pair (the ENSO mode, not shown) accounting for 26.4% of the total variance. The rotation period of this POP pair amounts to 42 months, with a decay time of 10 months. All other POPs were statistically insignificant. The dominant POP pair is clearly associated with ENSO, which can be inferred from the correlation of the complex coefficient time series (not shown) with the Niño3 (5°S - 5N, 150°W -90°W) SSTA time series. The zero-lag correlation of the real part time series with the Niño3 time series amounts to 0.94 and the 4-months lag correlation of the imaginary part time series with the Niño3 time series amounts to

0.74. A cross-spectral analysis of the two coefficient time series (not shown) showed the theoretically expected result that they are highly coherent (above the 99% significance level) with a phase shift of about -90° for periods between 20 and 70 months.

Analysis considering all seasons

The correlations of the Indo-Pacific SSTAs with the averaged SSTAs in SETIO and WTIO based on seasonal values are shown in Fig. 3.4. Again (as shown in Fig. 3.1 by retaining the full data set), the correlation maps obtained from the "ENSO-removed" data show that the SSTAs in the eastern and western parts of the Indian Ocean are not significantly correlated with each other, when all 4 seasons are considered together.

Analysis for SON

Fig. 3.5 shows the correlations of the Indo-Pacific SSTAs with box averaged SSTAs in SETIO and WTIO for the boreal fall season. A negative correlation between the SSTAs in SETIO and those in the central (but not western) Indian Ocean is seen in Fig. 3.5b. These negative correlations are larger than those in Fig. 3.2b and they extend to the north of the equator. In conclusion, Figs. 3.2, 3.4 and 3.5 show that SSTAs in the eastern and western parts of the Indian Ocean are not strongly negatively correlated, and that there is a significant negative correlation between the SSTAs in the eastern and central parts of the Indian Ocean during the boreal fall season. This negative correlation between the eastern and central regions exists also when the ENSO signal is removed from the data. In the next section, the mechanisms that may explain this dipole–like variability are discussed by analyzing a suite of coupled model simulations.

ENSO signal removed/ all seasons:

a) Observations, correlation with western box

b) Observations, correlation with eastern box

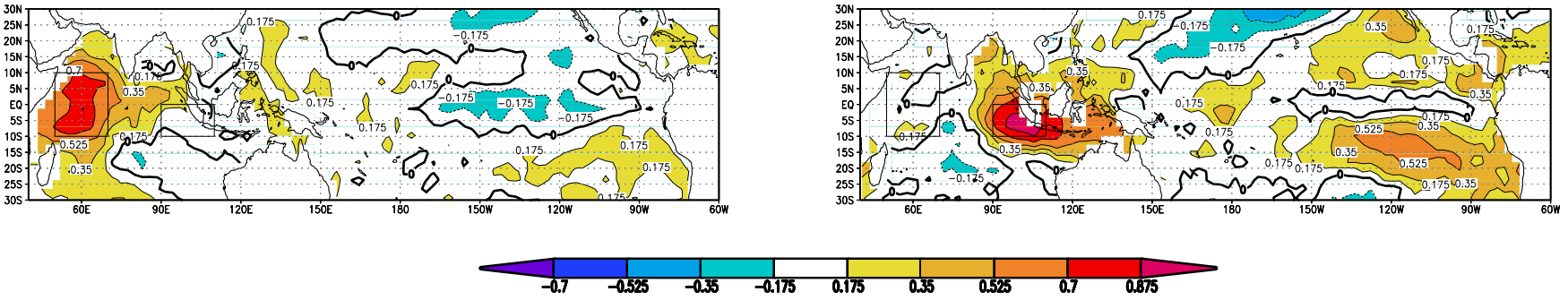

Figure 3.4: Correlation of (a) WTIO box-averaged SST anomalies, and (b) SETIO box-averaged SST anomalies with Indo-Pacific SST anomalies for all seasons. SST anomalies from the Hadley Center observational dataset, 1949-1998. The ENSO signal was subtracted. Correlations exceeding 0.21 for (a) and 0.30 for (b) are significant at the 95% confidence level.

ENSO signal removed/ boreal fall season (SON):

a) Observations, correlation with western box

b) Observations, correlation with eastern box

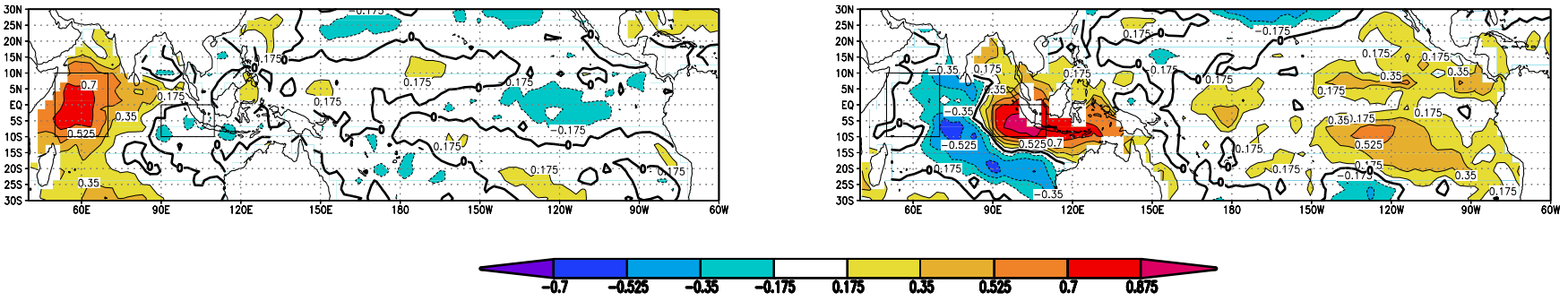

Figure 3.5: Correlation of (a) WTIO box-averaged SST anomalies, and (b) SETIO box-averaged SST anomalies with Indo-Pacific SST anomalies for SON. SST anomalies from the Hadley Center observational dataset, 1949-1998. The ENSO signal was subtracted prior to the analysis. Correlations exceeding 0.32 for (a) and 0.27 for (b) are significant at the 95% confidence level.

3.3 Coupled model simulations

Three different coupled model simulations were analyzed to investigate the roles of ENSO and ocean dynamics in the generation of the interannual SST variability of the tropical Indian Ocean. The first coupled run is a standard integration with the coupled ocean-atmosphere general circulation model (CGCM) ECHO-G (Legutke and Voss 1999). This run serves as a control integration. The second coupled run is similar to the control run, but the interannual ocean-atmosphere interactions have been inhibited in the tropical Pacific Ocean by setting the sea surface temperature to climatological values in this region (non-ENSO experiment). The ocean general circulation model is replaced by a fixed-depth mixed layer model in the third coupled run. For details of the two experiments with the ECHO-G model the reader is referred to chapter 2. In addition to the two experiments with the ECHO-G model, a simulation with a mixed layer ocean model coupled to the ECHAM4 atmosphere model (Roeckner et al. 1996, the same atmosphere model that has been used in the control and non-ENSO experiments with ECHO-G) was used. The mixed layer model has a constant depth of 50 m and does not carry any ocean dynamics by definition. In such a model, only variations in the surface heat flux can produce SST anomalies. For each one of the three coupled simulations, a sequence of 100 years was available for analysis.

The standard deviations of the SST anomalies for the observations and for the three coupled model simulations are shown in Fig. 3.6. The observations (Fig. 3.6a) exhibit a north-south gradient in the values of the standard deviation, with largest values near 30°S. The variability in the mixed layer run (Fig. 3.6b) compares well to observations (Fig. 3.6a). The non-ENSO and control simulations (Figs. 3.6c and 3.6d) display somewhat larger standard deviations. Compared with the control run, the non-ENSO run shows a reduction of about 0.1°C in the SST variability almost everywhere in the tropical Indian Ocean basin. For the tropical Pacific Ocean, the variability in the control run is about ten times larger than the variability in the non-ENSO run (not shown). In addition, the standard deviation maps for the boreal fall season were calculated separately (not shown). They exhibit similar patterns to those shown in Fig. 3.6: the SST variability increases with the complexity of the ocean model and a large part of the SST variability can be already produced in the mixed layer simulation, where the forcing mechanism is only due to surface heat flux anomalies.

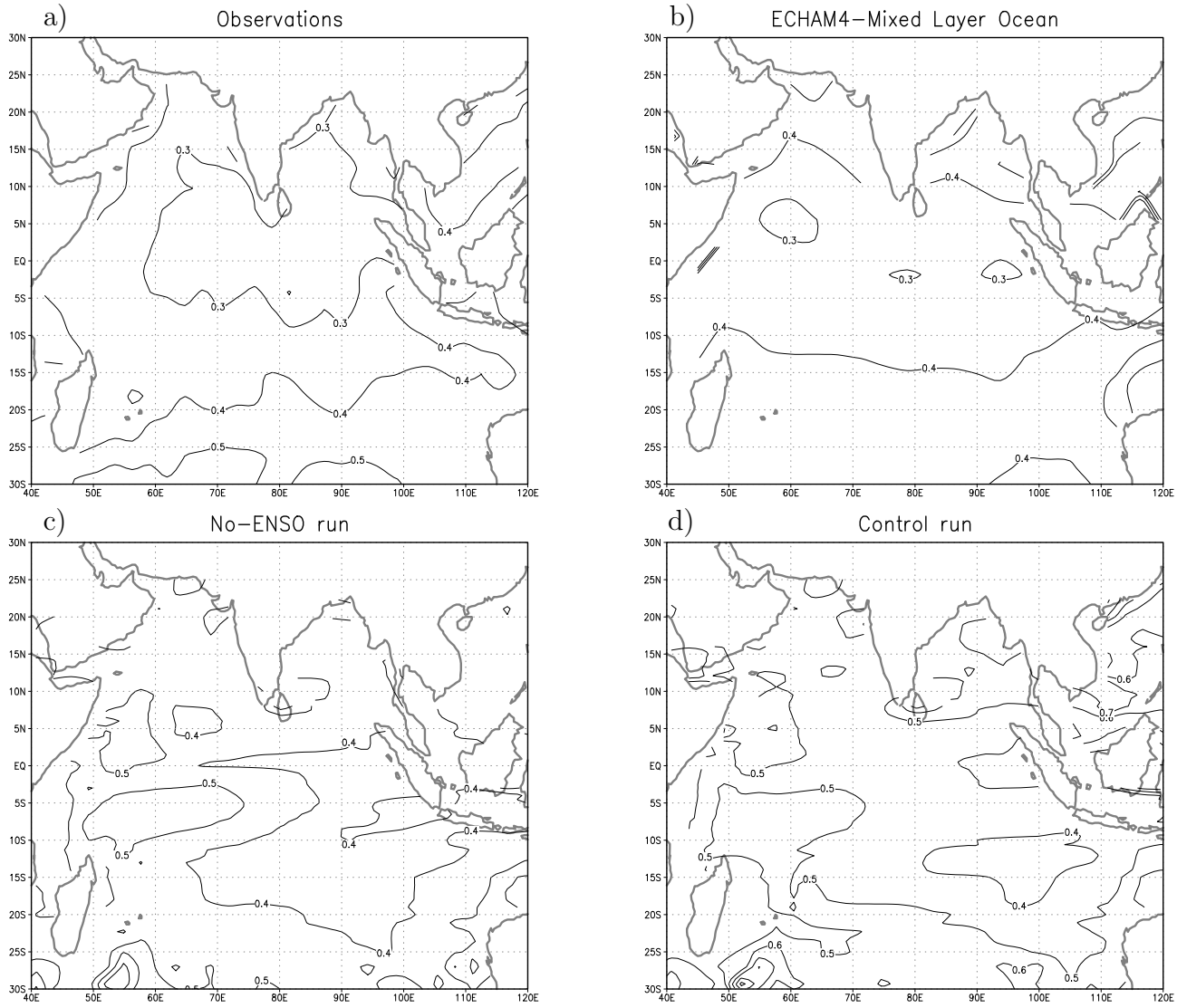

Figure 3.6: Spatial distribution of the standard deviation of the SST anomalies. (a) for the Hadley Center observational dataset, (b) for the ECHAM4–mixed layer ocean simulation, (c) for the non-ENSO run of the CGCM ECHO-G and (d) for the control run. Units are given in °C.

3.3.1 Fully coupled ocean-atmosphere GCM

To examine the interannual variability independent of ENSO, the subtraction of the leading POP pair may not be the best method, therefore the outputs of the two experiments with the ECHO-G model were additionally analyzed. Fig. 3.7 shows the SSTA-correlation maps with the box averaged SST anomalies in the SETIO and WTIO regions when all seasons are considered. Both simulations, the control run (Fig. 3.7a and 7b) and the non-ENSO run (Figs. 3.7c and 3.7d), show positive correlations almost everywhere in

the Indian Ocean. In particular, as in the observations, there is no negative correlation simulated in the two coupled runs between the western and eastern Indian Ocean. These model results support the observational results. It is suggested further that the results do not depend on the way of subtracting the ENSO signal.

Fig. 3.8 shows the spectra of box-averaged SST anomalies in the SETIO and WTIO regions for the control and non-ENSO runs. Each spectrum is tested against the hypothesis that the spectrum is produced by a first order autoregressive process (red noise spectrum), and a 95% confidence level for accepting the red noise hypothesis is also shown. For the control run, the spectra of the two boxes (Figs. 3.8a and 3.8b) show enhanced variability for periods of 5-10 seasons, i. e. about 1-3 years (the coupled model simulates a quasi-biennial ENSO period). In contrast, the spectra of the non-ENSO run (Figs. 3.8c and 3.8d) are consistent with red noise spectra. This result implies also that a dipole mode independent of ENSO and associated with a specific timescale does not seem to exist.

The correlation maps for boreal fall (SON) are shown in Fig. 3.9. Both the control run and the non-ENSO run yield similar correlation maps. Although the correlations between the box averaged SSTAs in SETIO and WTIO and the SSTAs in the Indian Ocean are low, there is some indication of dipole-like variability. This means that although ENSO was removed physically in the non-ENSO run, there is still a mechanism which produces a dipole-like structure in the SST anomalies in the boreal fall season. The correlation maps for the other seasons (not shown) do not exhibit a dipole-like structure.

All seasons:

a) Control run, correlation with western box

b) Control run, correlation with eastern box

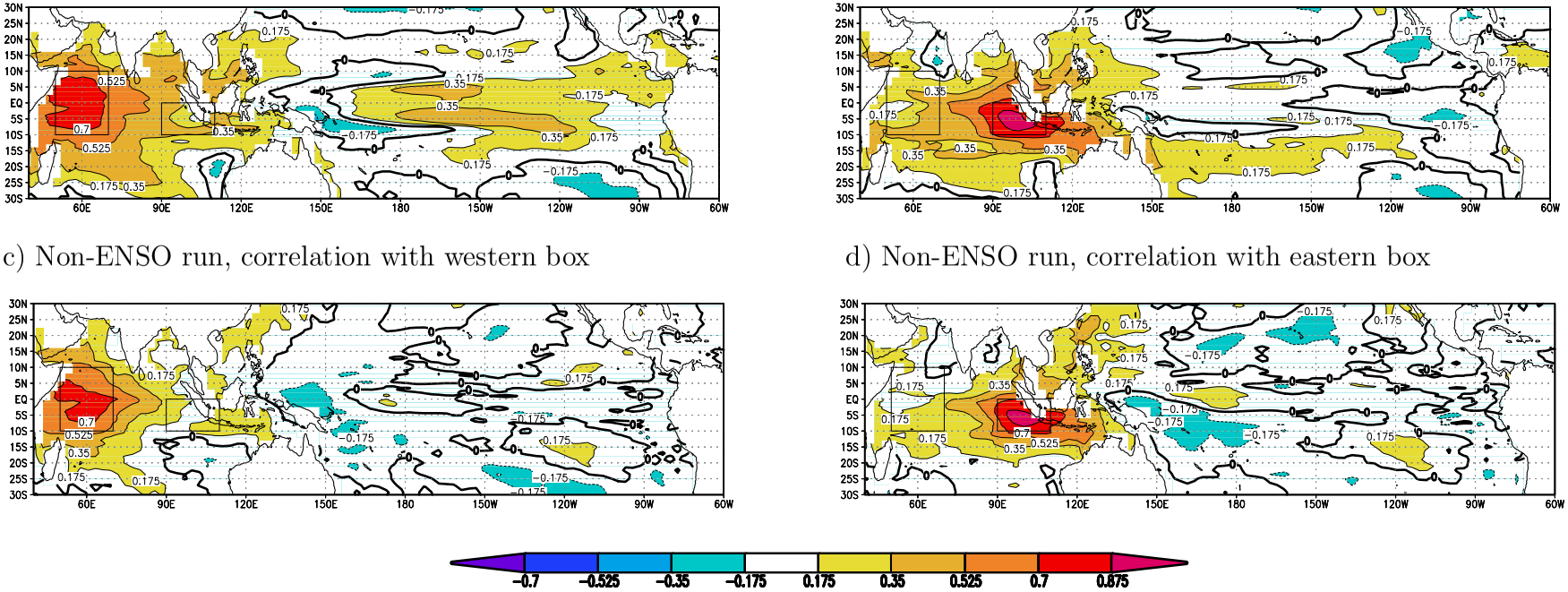

c) Non-ENSO run, correlation with western box

d) Non-ENSO run, correlation with eastern box

Figure 3.7: Correlation of WTIO box-averaged SST anomalies and SETIO box-averaged SST anomalies with Indo-Pacific SST anomalies for all seasons. (a) and (b) for SST anomalies from the control run of the CGCM ECHO-G. (c) and (d) for SST anomalies from the non-ENSO run. In (a) and (c) correlations are with respect to the WTIO. In (b) and (d) correlations are with respect to SETIO. Correlations exceeding 0.15 for (a), 0.16 for (b), 0.12 for (c) and 0.13 for (d) are significant at the 95% confidence level.

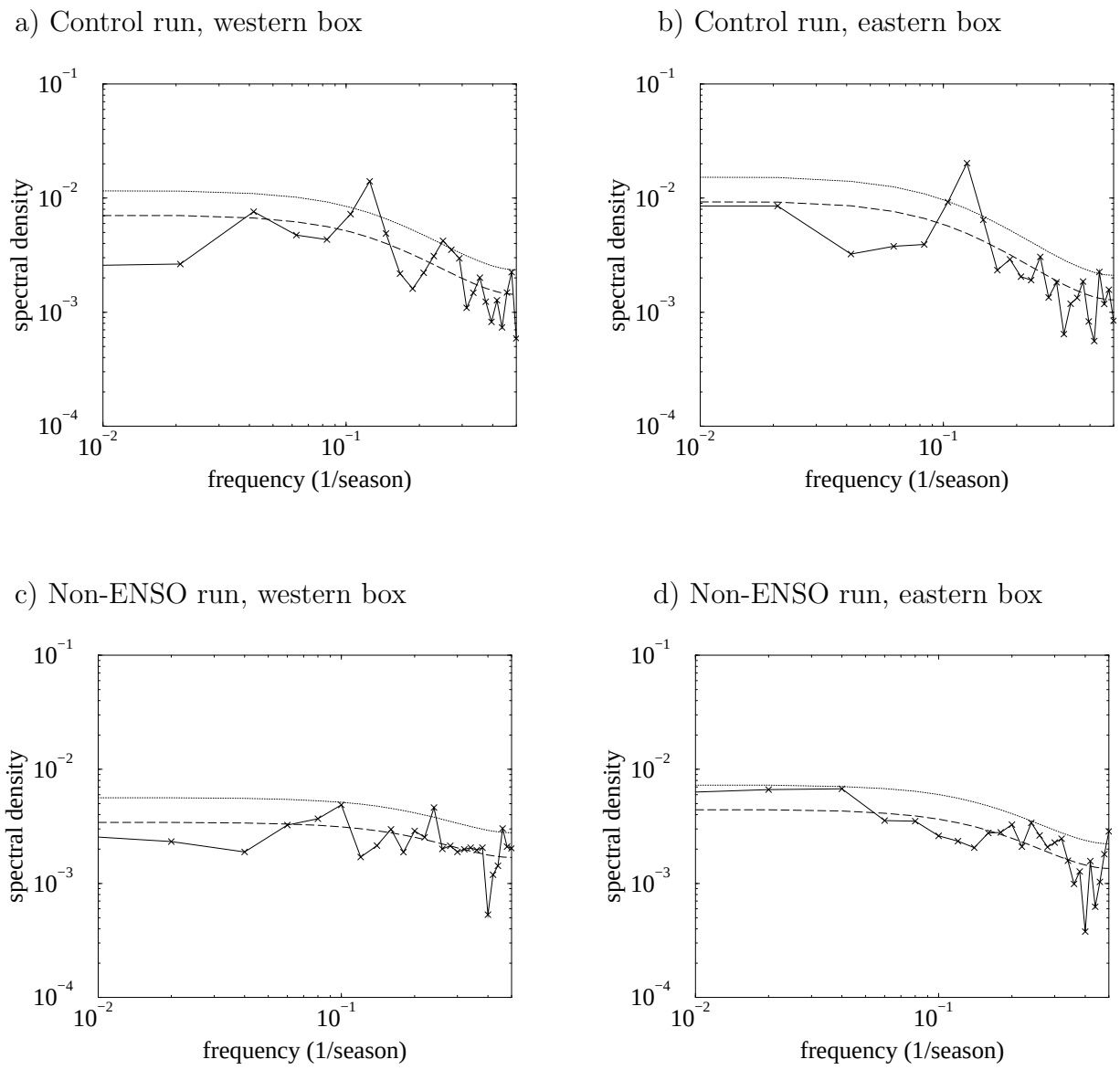

Figure 3.8: Spectra of box-averaged SST anomalies in the SETIO and WTIO regions when all seasons are considered. (a) and (b) for SST anomalies from the control run with the CGCM ECHO-G. (c) and (d) for SST anomalies from the non-ENSO run. In (a) and (c) spectra are for WTIO. In (b) and (d) spectra are for SETIO. The dotted lines are the expected red noise spectra. The dashed lines are the 95% confidence level for the null hypothesis of a red noise spectra.

Boreal fall season (SON):

a) Control run, correlation with western box

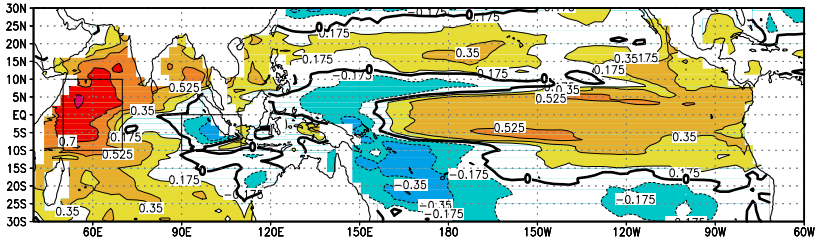

b) Control run, correlation with eastern box

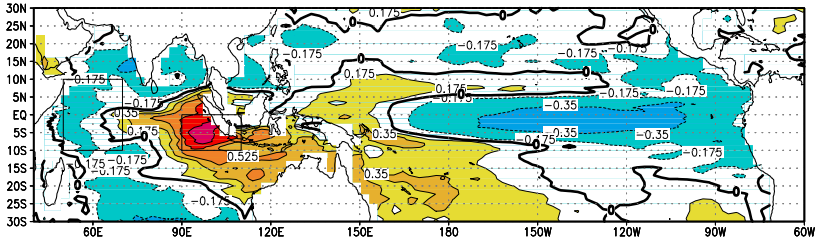

c) Non-ENSO run, correlation with western box

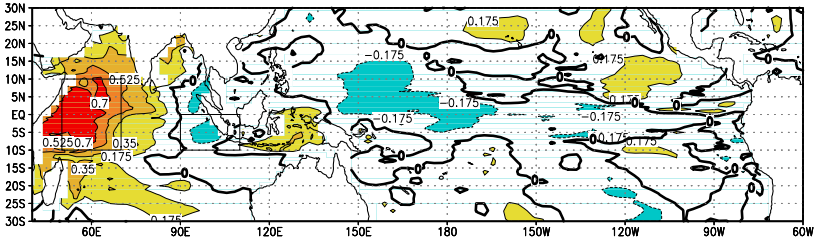

d) Non-ENSO run, correlation with eastern box

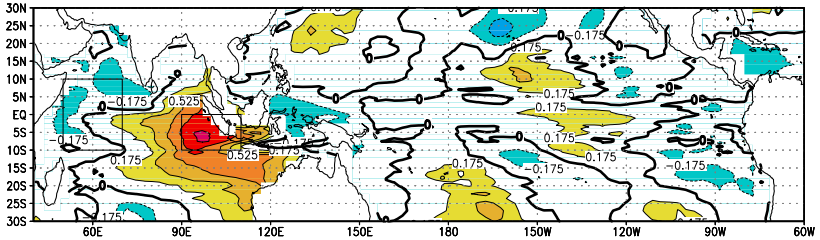

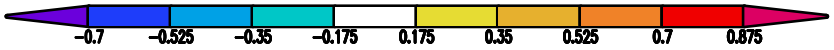

Figure 3.9: Correlation of WTIO box-averaged SST anomalies, SETIO box-averaged SST anomalies with Indo-Pacific SST anomalies for SON. (a) and (b) are for SST anomalies from the control run of the CGCM ECHO-G. (c) and (d) for SST anomalies from the non-ENSO run. In (a) and (c) correlations are with respect to the WTIO. In (b) and (d) correlations are with respect to SETIO. Correlations exceeding 0.20 for (a), (b), and (d) and 0.24 for (c) are significant at the 95% confidence level.

All seasons:

a) ECHAM4–mixed layer, correlation with western box

b) ECHAM4–mixed layer, correlation with eastern box

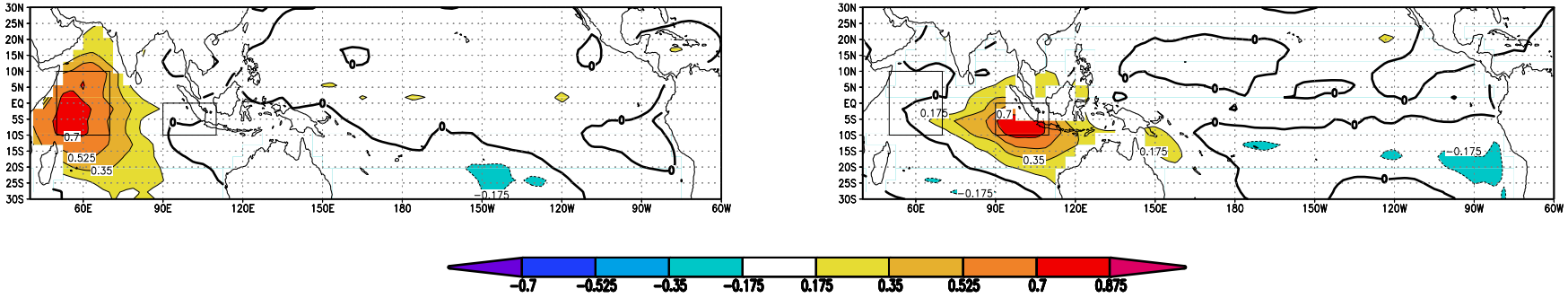

Figure 3.10: Correlation of (a) WTIO box-averaged SST anomalies, and (b) SETIO box-averaged SST anomalies with Indo-Pacific SST anomalies for all seasons. The SST anomalies are from the ECHAM4–mixed layer ocean simulation. Correlations exceeding 0.16 for (a) and 0.20 for (b) are significant at the 95% confidence level.

Boreal fall season (SON):

a) ECHAM4–mixed layer, correlation with western box

b) ECHAM4–mixed layer, correlation with eastern box

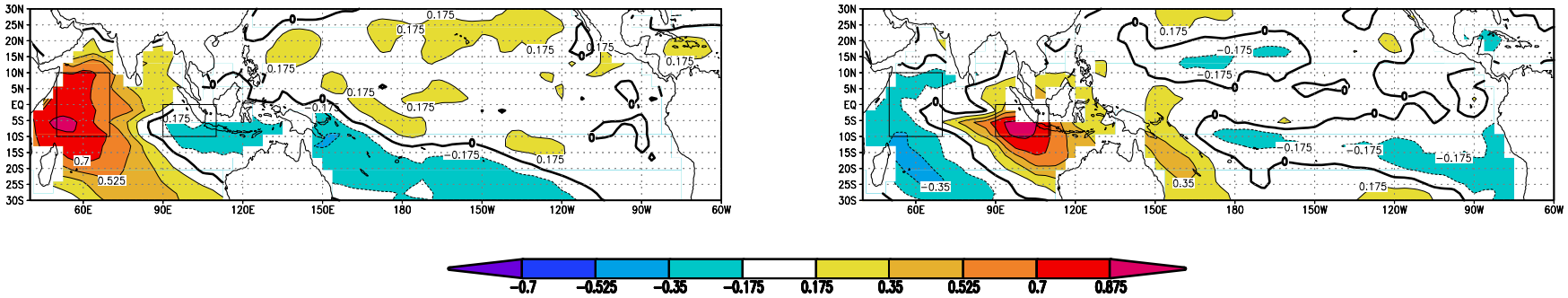

Figure 3.11: Correlation of (a) WTIO box-averaged SST anomalies, and (b) SETIO box-averaged SST anomalies with Indo-Pacific SST anomalies for SON. SST anomalies are from the ECHAM4–mixed layer ocean simulation. Correlations exceeding 0.20 for (a) and 0.22 for (b) are significant at the 95% confidence level.

3.3.2 ECHAM4 coupled to a mixed layer ocean

The basic idea of a simulation with an atmosphere model (in this case ECHAM4) coupled to a fixed–depth mixed–layer ocean model is that SST variability for each grid point of the ocean is forced only by the local vertical air–sea fluxes from the atmosphere. This occurs because the grid points of the ocean model do not interact with each other and the depth of the mixed layer is constant, so that ocean dynamics is not simulated. Thus, such a simulation represents the Null hypothesis of SST variability described by the Hasselmann's stochastic climate model (1976). This model assumes that the SST variability reflects the response of the oceanic surface mixed layer to the day–to–day changes in the local air–sea fluxes, which act as a stochastic forcing.

Is the dipole-like variability in the non-ENSO run a result of ocean dynamics or of forcing by air–sea fluxes? In order to answer this question, correlation analyses were performed for the SST anomalies from the mixed layer run.

Correlation analyses of SST anomalies from the mixed layer simulation are shown in Figs. 3.10 and 3.11. Figure 3.10 corresponds to the case when all the seasons are considered and Fig. 3.11 when only fall (SON) is considered. Both Fig. 3.10 and Fig. 3.11 show some correspondence with the maps derived from the observations (Figs. 3.1 and 3.2), and with those for the coupled runs (Figs. 3.7 and 3.9). The spectra of the SST anomalies in the boxes SETIO and WTIO considering all seasons are consistent with the red noise assumption (not shown). It can be concluded from the results of the mixed layer simulation that an ENSO-independent dipole-like SST anomaly pattern exists in the boreal fall season, which can be explained by atmospheric forcing. Dynamical processes in the ocean are not necessary to produce this type of bipolar SST variability. However, dynamical processes in the ocean and coupled ocean-atmosphere interactions may modify this type of variability.

3.4 Discussion and conclusions

Correlation analyses of seasonal SST anomalies from the Hadley Center SST observations during the period 1949-1998 and from three different CGCM runs show consistent results. The dominant SST variability in the tropical Indian Ocean is related to ENSO. The ENSO-related SST response of the Indian Ocean in the boreal fall season is a dipole.

However, evidence of the existence of an SST dipole mode with temporal oscillatory behavior was not found. Yet, there is dipole-like SST variability in the tropical Indian Ocean that is independent of ENSO. However, this type of variability is not significantly different to an autoregressive process of first order, and does not necessarily involve ocean dynamics. That implies that the ocean is: either responding passively to the atmospheric forcing by simply integrating the atmospheric noise due to the large heat capacity of the ocean's mixed layer, according to the stochastic theory of climate variability proposed by Hasselmann (1976); or the feedback implied in the equatorial SST dipole is weak and not significantly more energetic than expected from the stochastic forcing approach.
Most studies so far described the ENSO response in the Indian Ocean as a homogeneous response: During El Niño events, the Indian Ocean exhibits basin wide warm SST anomalies and during La Niña conditions, the SST anomalies are of opposite sign. This is true for some seasons, especially for the boreal winter season (DJF), but for the borealfall season (SON), this is generally not the case. It was found that in the boreal fall season, on average, the ENSO signal can be seen as a dipole-like pattern: During El Niño events, cold anomalies are observed east of 80°E and warm SST anomalies west of 80°E, during La Niña events, the reverse SST anomaly pattern is observed .

In summary, the results show that there is dipole-like variability in the SST of the Indian Ocean. This variability can be associated with the ENSO phenomenon and may also be forced stochastically by the atmosphere. The analysis of observations and simulations with a hierarchy of coupled models show no evidence of an ENSO-independent dipole mode. A dipole SST pattern is, however, seen in the boreal fall season in both situations when ENSO is included and when ENSO is removed. The spectral characteristics of the SST variability in the tropical Indian Ocean when ENSO is included are consistent with an oscillatory forcing by ENSO. When ENSO is removed, the spectral characteristics of the SST variability are consistent with a stochastic forcing, and the variability can be generated without ocean dynamics. The only mode-like dipole variability (in the physical sense that air-sea interactions lead to a temporal oscillation) that could be found is associated with the ENSO phenomenon.

Chapter 4

South Indian Ocean Rossby Waves and their Interaction with the Atmosphere

4.1 Introduction

The dominant interannual variability in the tropics is the El Niño–Southern Oscillation (ENSO) phenomenon, which has its largest amplitude over the Pacific and Indian Oceans (Philander 1990). ENSO has a detectable impact on the circulations of the Indian and Atlantic Oceans via wind stress anomalies induced over these oceans (Latif and Barnett 1995). During ENSO episodes, sea surface temperature (SST) anomalies in the tropical eastern/central Pacific affect the surface atmospheric circulation and precipitation patterns over the Indian and western Pacific Oceans through displacements of the near-equatorial Walker circulation. These atmospheric perturbations, in their turn, influence the underlying ocean not only through wind stress anomalies but also by modulating the surface heat and radiative fluxes, thereby generating SST anomalies in the Indian Ocean and western Pacific regions (Lau and Nath 2003). Thus, the atmosphere acts as a 'bridge' that connects SST anomalies in the eastern equatorial Pacific with those in remote tropical oceans (Klein 1999; Venzke et al. 2000).

Some studies have shown that in the relationship between rainfall variability in regions adjacent to the Indian Ocean and ENSO, the local SST is an essential component. For

example, the modeling studies with atmospheric general circulation models (AGCM) of Latif et al. (1999) and Goddard and Graham (1999) show that the Indian Ocean SST plays an active role in forcing ENSO-related rainfall anomalies over eastern and southern Africa.

Other studies suggest that the Indian Ocean is an active player in climate variability on seasonal to interannual timescales (Webster et al. 1999; Saji et al. 1999; Murtugudde et al. 2000, and others). These studies suggest that there is a mechanism of variability, whose dynamics is internal to the Indian Ocean and is independent of ENSO. The mechanism is characterized by anomalous east-west gradients in SST and sea surface height (SSH) in the tropical Indian Ocean, accompanied by wind and rainfall anomalies. Webster et al. (1999) proposes additionally that this mechanism gives rise to a mode of variability that is oscillatory. The modeling study by Baquero-Bernal et al. (2002), however, shows that the ENSO signal in the boreal fall season can be seen as an east-west contrast and that variability with an east-west SST contrast is oscillatory only when ENSO is present. This topic has been discussed in the previous chapter.

In a study with oceanic and atmospheric data from reanalysis products Xie et al. (2002, hereafter XASM) showed that an open-ocean upwelling zone exists in the tropical western South Indian Ocean (SIO), and that there is a strong influence of thermocline movements on SST in this upwelling zone. The thermocline effect on SST in the western tropical SIO is made possible by the presence of both upwelling and a shallow thermocline in this region. Additionally, the authors found that ENSO and processes offshore West Sumatra, Indonesia, are the dominant forcing for the SIO thermocline variability through the forcing of SIO Rossby waves, which propagate westward and interact with the atmosphere. The interaction consists of a switch from a *positive* thermocline feedback to a *negative* thermocline feedback. Both feedbacks include the propagation of SST and wind stress curl (WSC) anomalies with the positive thermocline depth anomalies produced by the Rossby waves. For the *positive* (*negative)* feedback, the WSC anomalies reinforce (dissipate) the thermocline depth anomalies. Thus, through the effect of the SIO downwelling Rossby waves on SST, the waves offer potential predictability for SST and tropical cyclons in the western SIO in the boreal winter and spring seasons.

Several studies, which have identified ENSO-related and ENSO-independent mechanisms for Indian Ocean variability, have been focused on analysis based on ENSO-related

indices. These studies either have generalized the results to what could be produced by ENSO-independent mechanisms, or have used ENSO-related indices but have identified these indices as ENSO-independent. Thus, many questions about the effect of ENSO-independent mechanisms remain to be resolved. In the present study, the mechanisms for SIO climate variability are investigated by using a set of two experiments that allows to address the roles of the ENSO-related and ENSO-independent mechanisms separately.

The purpose of this study is to investigate the thermocline variability, its relationship with the interannual variability in the tropical Indian Ocean and the relationship of both of these with the ENSO cycle in the Pacific. Emphasis in this chapter is given to the spatial structures. The temporal behavior is considered in chapter 5. Data from oceanic and atmospheric reanalysis products and from the output of two experiments with the coupled general circulation model (CGCM) ECHO-G have been analyzed. In the control experiment, air-sea interactions are allowed everywhere, whereas in the non-ENSO experiment climatological SST are specified in the tropical Pacific. It will be shown that the major forcing of the SIO Rossby waves is associated with the interannual SST variability in the Pacific and that only in the presence of ENSO, spring SST anomalies in the western SIO region have some potential predictability associated with SIO Rossby wave activity. It will also be shown that the ENSO signal in the Indian Ocean includes both a dynamical and a thermodynamical response, that ENSO influences the Indian Ocean at two different interannual timescales and that the interannual variability in the Indian Ocean region is consistent with a cycle only if ENSO is included in the simulations.

This chapter is organized as follows. Section 4.2 introduces the datasets used. Section 4.3 describes the capability of the ECHO-G model to simulate the main features of the observed patterns of climatological mean and variance in the tropical Indian Ocean. Furthermode, Rossby wave propagation is identified through a statistical analysis of the space-time structure of HC anomalies in the tropical Indian Ocean. Sections 4.4, 4.5 and 4.6 examine how the Rossby waves interact with the atmosphere and their relationship with the ENSO phenomenon. Section 4.7 is a summary, including a discussion of the implications of the results in this chapter.

4.2 Data

Two experiments with the coupled ocean-atmosphere general circulation ECHO-G model are used: in one experiment, air-sea interactions are suppressed in the tropical Pacific Ocean (non-ENSO experiment) and in the other experiment, interactions are allowed everywhere (control experiment). A detailed description of the two experiments is given in chapter 2. The model results are compared with those obtained from a reference dataset that is based on the SST from the Hadley Center for Climate Prediction and Research (Folland et al. 1999) for the period 1949-1998, the 20°C thermocline depth fom the Bureau of Meteorology Research Centre (BMRC) (Smith et al. 1989; Smith 1995), the heat content from the Simple Ocean Data Assimilation SODA product (Carton et al. 2000), the wind stress from the National Center for Environmental Prediction (NCEP) reanalysis (Kalnay et al. 1996), and the TOPEX/Poseidon sea surface height measurements for the period 1993-1998 (AVISO 1998). For each variable, the monthly mean climatology was calculated and then subtracted from the basic time series to compute the interannual anomalies. The heat content (HC) has been computed by the integration of ocean temperature from the surface to 206m depth for the two experiments. From the SODA dataset, only the HC of the upper 125m was available for analysis.

4.3 The interannual variability

4.3.1 Covariability of SST and heat content

Figure 4.1 shows the SST standard deviation along with annual-mean SST and surface wind stress for the control experiment and for the Hadley Center dataset. In the western tropical SIO (Fig. 4.1a), enhanced SST variability is found between 5°S and 15°S and 50°E and 70°E.

In the equatorial and North Indian Ocean the monsoons are a major cause of variability. During the summer monsoon season, strong coastal upwelling takes place offshore Somalia and offshore Southwest of Sumatra, causing a local SST standard deviation maximum. In the SIO, the southeasterly trade winds are present throughout the year and peak between 15°S and 20°S. The curl between the southeasterly trades and equatorial westerlies implies that an upwelling zone is present from 5°S to 15°S year-round, which is consistent with the results in XASM.

The annual mean distribution of the 20°C thermocline depth (z20) and the local correlation of HC and SST anomalies for the control experiment are shown in Fig. 4.2a. The correlation between interannual variability in SST and z20/SSH gives an estimation of upwelling. In the ECHO-G model, high correlations are found in the upwelling zone off Somalia and in the western SIO. The western SIO upwelling zone is collocated with both a shallow thermocline and a local SST variability maximum. The z20 minimum in the control experiment (Fig. 4.2a) is at about 80 m at 8°S, 55°E. The western SIO upwelling does not lead to a local SST minimum in the annual mean, because it is relatively weak compared to other major upwelling zones (XASM).

In general, the results described above are in relative good agreement with the observations (Figs. 4.1b and 4.2b). However, some differences are noted. In the observations, there is a relationship between the annual mean SST and SST standard deviation, with lowest variability coinciding with the warmest SST. In the model, however, no such relationship exists. In the model, the SST standard deviation is overall larger (approximately 0.2 °C) than in the Hadley Center dataset and the SST south of the equator in the control experiment is about 1°C larger than in the observations. The model simulates an annual mean distribution of z20, which is approximately 20m deeper than in the BMRC dataset. The model does not exhibit high correlation between SST and z20 in the zone off Indonesia, a zone of upwelling and the western tropical SIO active upwelling zone is confined more to the west than in the observations. This is most likely caused by a deep thermocline in these regions in the model. Additionally, the model shows high correlations between HC and SST south of 15°S and in the Arabian Sea region that are not shown by the observations. The reason for this difference is not clear and deserves further investigation. It is likely, however, that errors in the simulation of the wind stress play a role since this quantity is not flux corrected.

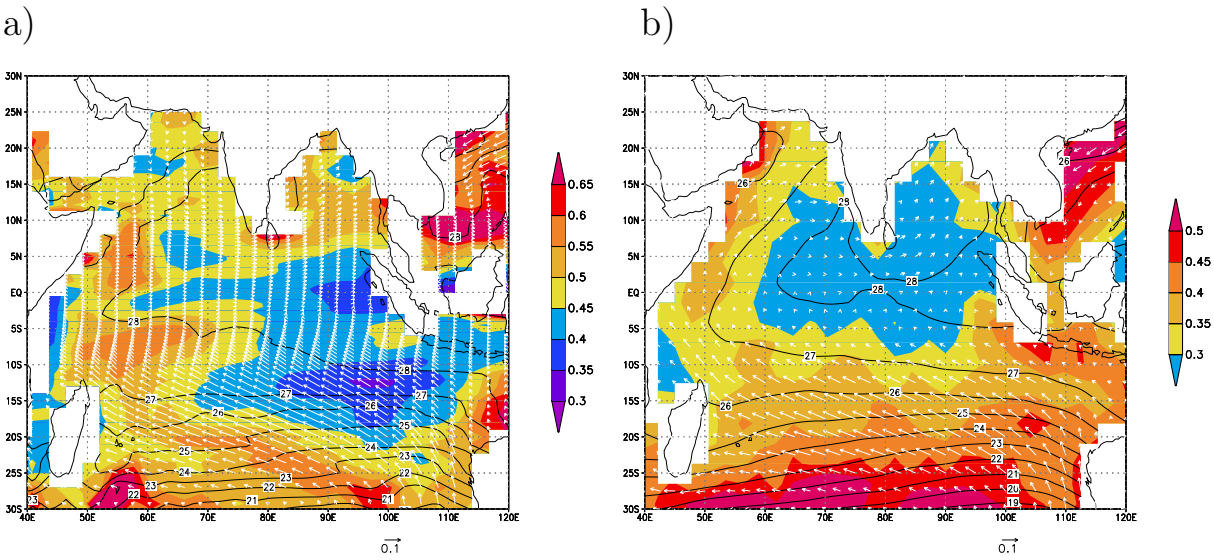

Figure 4.1: Annual-mean distributions of wind stress (vectors in Nm^{-2}), SST (contours in °C) and SST standard deviation (shaded) (a) for the control experiment and (b) for the Hadley Center dataset. Note that the color bars have different scales.

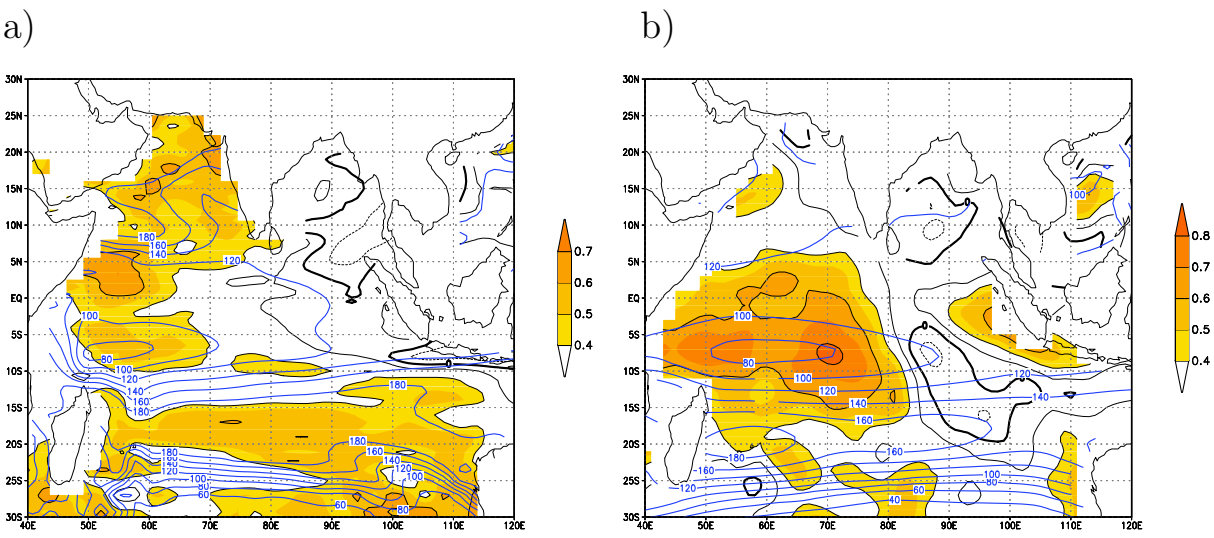

Figure 4.2: (a) Annual-mean distribution of the 20°C thermocline depth (z20;blue contours in m) and local correlation of heat content and SST anomalies (shaded and black contours, contour interval 0.2), for the control experiment; and (b) Annual-mean distribution of z20 (blue contours in m) from the BMRC dataset and local correlation of TOPEX/Poseidon sea surface high and Hadley Center SST anomalies (shaded and black contours, contour interval 0.2).

4.3.2 Rossby waves

The statistical investigation of the space-time structure of HC anomalies in the tropical Indian Ocean is based on the method of Principal Oscillation Patterns (POPs; Hasselmann 1988; von Storch et al. 1988; Schnur et al. 1993). In general, POPs are complex patterns with real and imaginary parts p^R and p^I. The corresponding complex coefficient time series (z^R,z^I) describe the time evolution of the POPs and satisfy the standard damped harmonic oscillator equation, so that the evolution of the system in the two-dimensional POP space can be interpreted as a cyclic sequence of spatial patterns

$$... - p^R \rightarrow p^I \rightarrow p^R \rightarrow -p^I \rightarrow -p^R ... \tag{4.1}$$

The POP pairs for the control and non-ENSO experiments are shown in Figs. 4.3 and 4.4, respectively. For the control experiment, the POP analysis reveals two dominant interannual POP pairs, pop1 and pop2 (Fig. 4.3). The pop1 pair (p_1^I, p_1^R) accounts for 12% of the total variance and has a rotation period of 17 months. The pop2 pair (p_2^I, p_2^R) has a period of 30 months, explains 16% of the total variance and is clearly associated with the ENSO phenomenon. This can be inferred from the correlation of the two time series z_2^R, z_2^I with the Niño3 index: 0.63 when Niño3 lags z_2^I by 2 months and 0.63 when Niño3 leads z_2^R by 3 months. The local explained variance by each of the two POP pairs for the control experiment is shown in Figs. B.1a and b.

The POP analysis of the HC anomalies in the non-ENSO experiment produces only one dominant interannual POP pair (pop1' pair: $p_{1'}^I, p_{1'}^R$; Fig. 4.4), which bears resemblance to the pop1 pair in the control experiment south of 5°S. This POP pair has a rotation period of 16 months and accounts for 6% of the total variance. The local explained variance by this POP pair is shown in Fig. B.2.

For both the control and non-ENSO experiments, the POP analysis reveals one intraseasonal POP pair (not shown). This POP pair accounts for 5% (19%) of the total variance and has a rotation period of 8 (5) months in the control (non-ENSO) experiment. The spatial patterns of this POP pair are consistent with equatorial wave dynamics within 5° of the equator (i.e. consistent with eastward propagating Kelvin waves and westward propagating Rossby waves). A detailed discussion of this intraseasonal POP pair is beyond the scope of this paper.

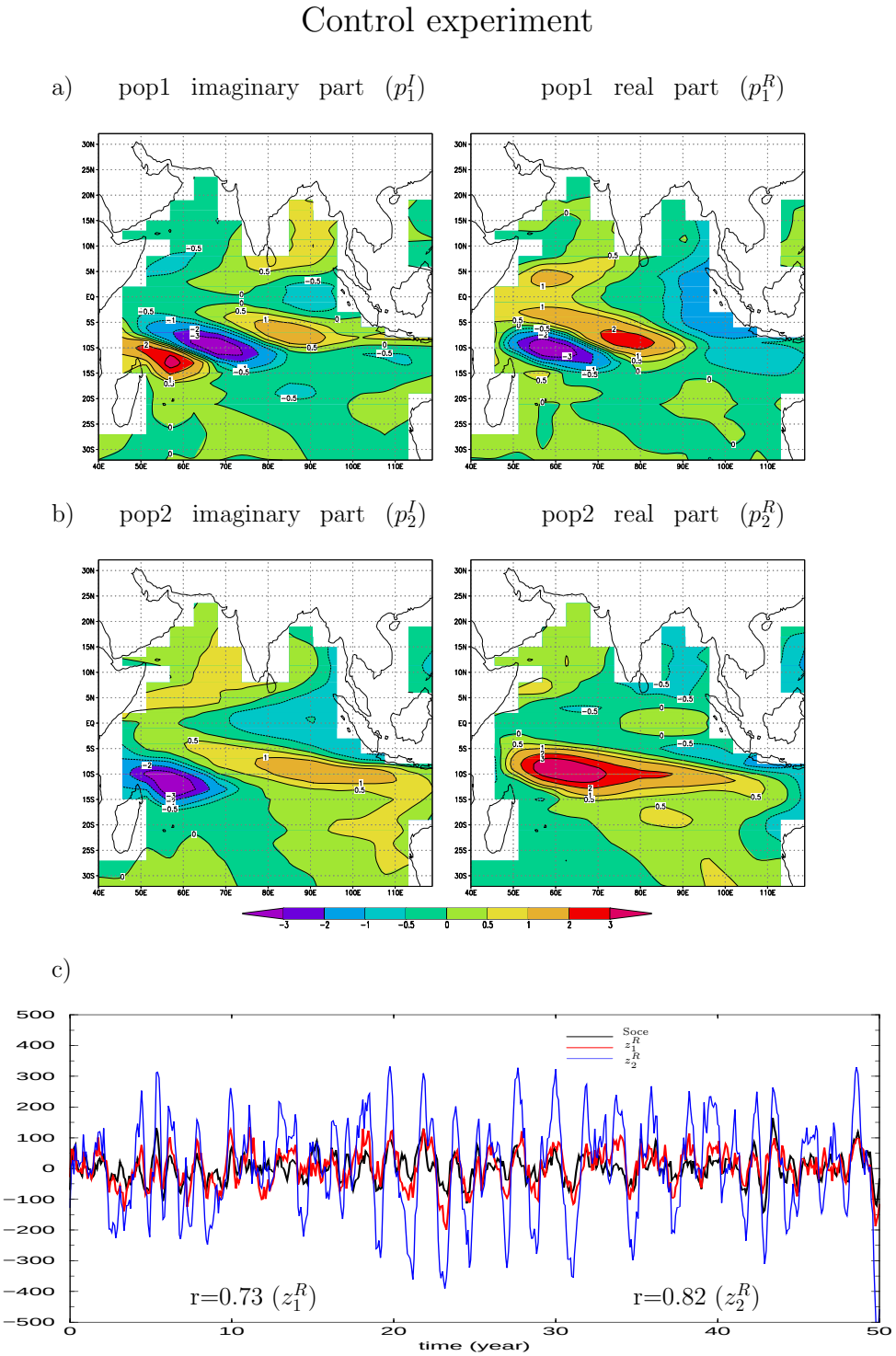

Figure 4.3: Dominant POPs of HC anomalies simulated in the control experiment. (a) pop1, (b) pop2 and (c) Soce index along with z^R time series (only the first 50 years of the time series are shown; correlations between Soce and each time series are shown in the lower part). Pop1 has a period of 17 months and explained variance of 12%. Pop2 has a period of 30 months and explained variance of 16%. The correlation between z_1^R and z_2^R is 0.6.

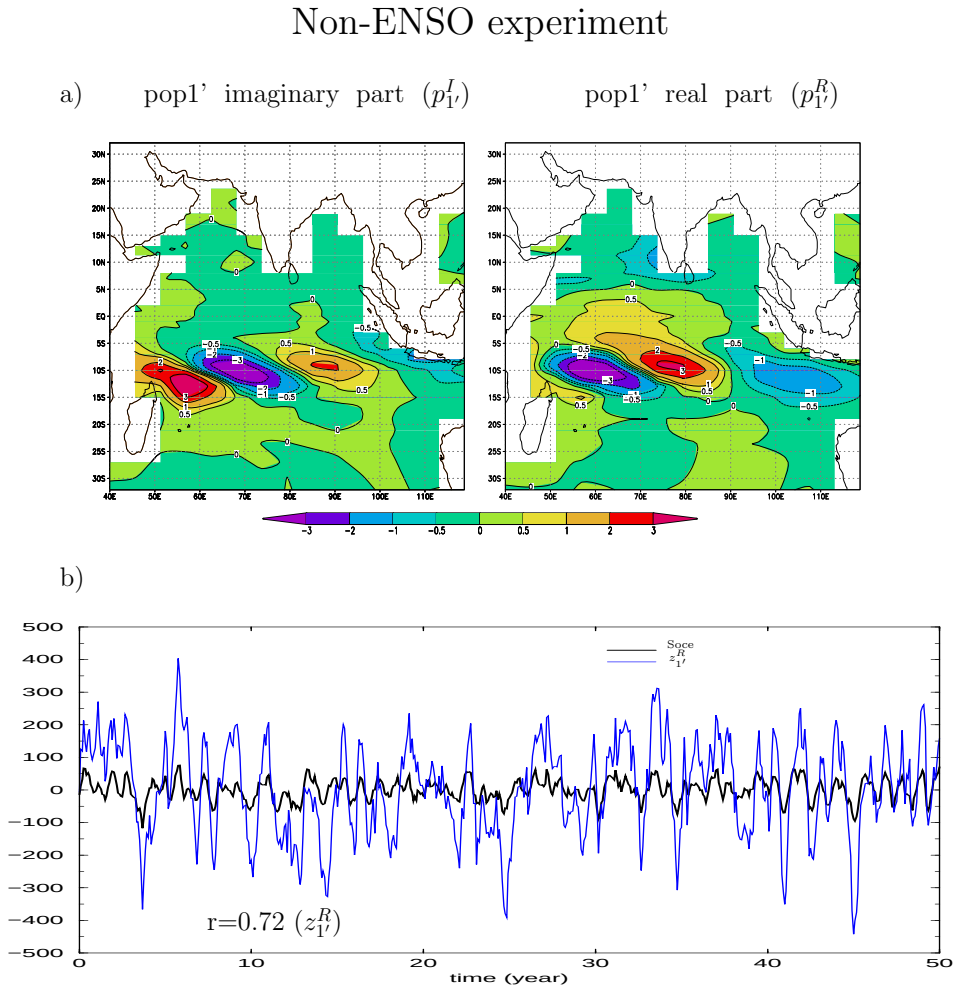

Figure 4.4: Dominant POP of HC anomalies simulated in the non-ENSO experiment. Pop1' has a period of 16 months and explained variance of 6% (a) pop1' and (b) Soce index along with $z^R_{1'}$ time series (only the first 50 years of the time series are shown; correlation between Soce and $z^R_{1'}$ is shown in the lower part).

The overall patterns of the interannual POP pairs in the two experiments are reminiscent of a westward propagating signal. This propagation has been studied using observations and ocean models and identified as Rossby waves (Perigaud and Delecluse 1993; Masumoto and Meyers 1998). The p^I_1 (p^I_2) pattern of pop1 (pop2) is followed after 4 (7) months by the p^R_1 (p^R_2) pattern. The p^I_1 (p^I_2) pattern exhibits positive HC anomalies between 5°S and 15°S that are located in the middle (eastern) part of the basin. A band of negative HC anomalies is found in the eastern equatorial zone. The positive anomalies of the p^I_1 (p^I_2) pattern have moved westward in the p^R_1 (p^R_2) pattern. Negative anomalies are found in the eastern part of the basin on (off) the equator in the p^R_1 (p^R_2) pattern. The structure of the pop1' pair in the non-ENSO experiment resembles pop1 of the control

experiment and is also reminiscent of a Rossby wave packet south of the equator. The main difference between these two pairs is that pop1' of the non-ENSO experiment does not have positive and negative HC anomalies at and north of the equator.

To track the variability associated with Rossby waves in the two experiments and in the SODA dataset, an index is constructed from the monthly HC anomalies averaged over 8°S to 12°S, 75°E to 85°E. This index is referred to as south central index (Soce). The Soce region was selected, since the z^R time series of the interannual POP pairs are highly correlated with the HC anomalies in this region. The correlations of the Soce index with the z^R time series of the dominant POPs in the two experiments are as follow: 0.7 with $z^R_{1'}$, 0.7 with z^R_1 and 0.8 with z^R_2. The pop1' explains 35% of the variance in the Soce region, the pop1 explains 30% and the pop2 explains 47%. The location of the Soce index deduced from the two experiments coincides with the location of a thermocline depth index proposed in Xie et al. (2002). Their index was used to illustrate the time-space evolution of thermocline variability in the SIO in the Simple Ocean Data Assimilation SODA product (Carton et al. 2000). The coincidence in the location of the indices gives confidence in the performance of the ECHO-G model. The POP pairs have been rotated in such a way that z^R has a maximum correlation with the Soce index.

The POP analysis of the HC anomalies in the SODA dataset (not shown) produces a dominant interannual POP pair, which accounts for 12% of the total variance and has a rotation period of 21 months and is partially associated with ENSO. The correlation between Niño3 and z^I is 0.47 at lag=0, and 0.34 when Niño3 lags z^R by 4 months. There is no other POP pair that explains more than 2% of the total variance. The POP analysis for SODA does not reveal any interseasonal POP pair.

The Rossby waves can be seen as the tendency for westward propagation of HC anomalies. The zonal sections of HC anomalies along 10°S for years 24 to 33 in both experiments are compared in Fig. 4.5. As an example of such westward propagation, one wave is followed in each experiment: for the control experiment (non-ENSO experiment) there is a downwelling wave in years 27 to 28 (26 to 27) that has positive anomalies at 95°E (90°E) in May of year 27 (July of year 26), it then travels to the west and can be traced to 50°E in July of year 28 (September of year 27). These waves have an estimated westward speed of about 14 $cm\ s^{-1}$ for both experiments, which is in agreement with the estimates of XASM.

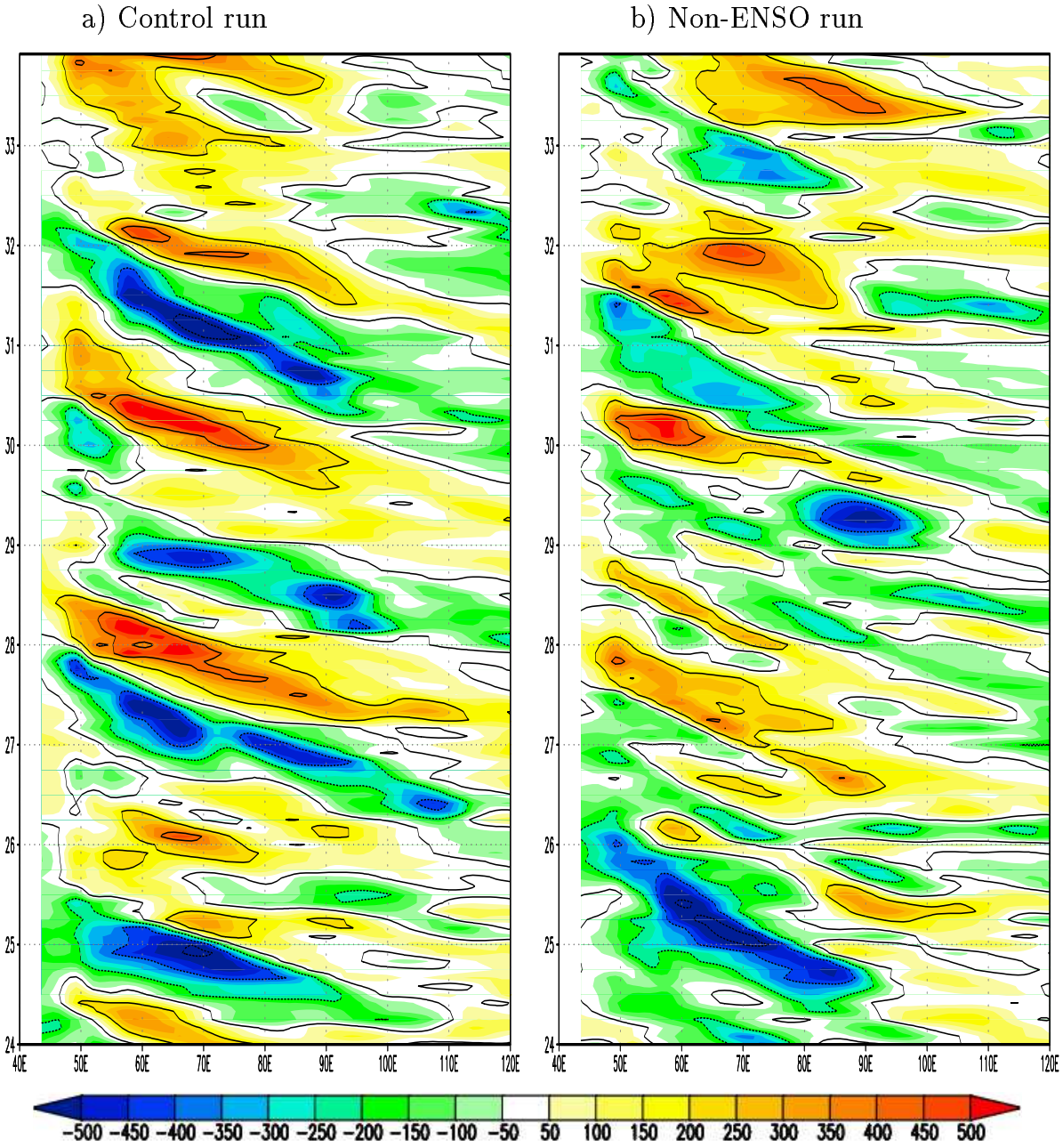

Figure 4.5: Hovmüller diagram of HC anomalies (m°C) at 10°S for years 24 to 33 (a) for the control experiment and in (b) for the non-ENSO experiment (contour interval 200 m°C).

Figure 4.6a shows the standard deviation of the Soce index as a function of calendar month for the two experiments and the SODA dataset. The Soce index shows strong seasonal variations in the three datasets; it reaches the minimum in the boreal summer and the maximum in the boreal winter. In general, the seasonality of the Soce index in the two experiments is in good agreement with the one from the SODA dataset. There are,

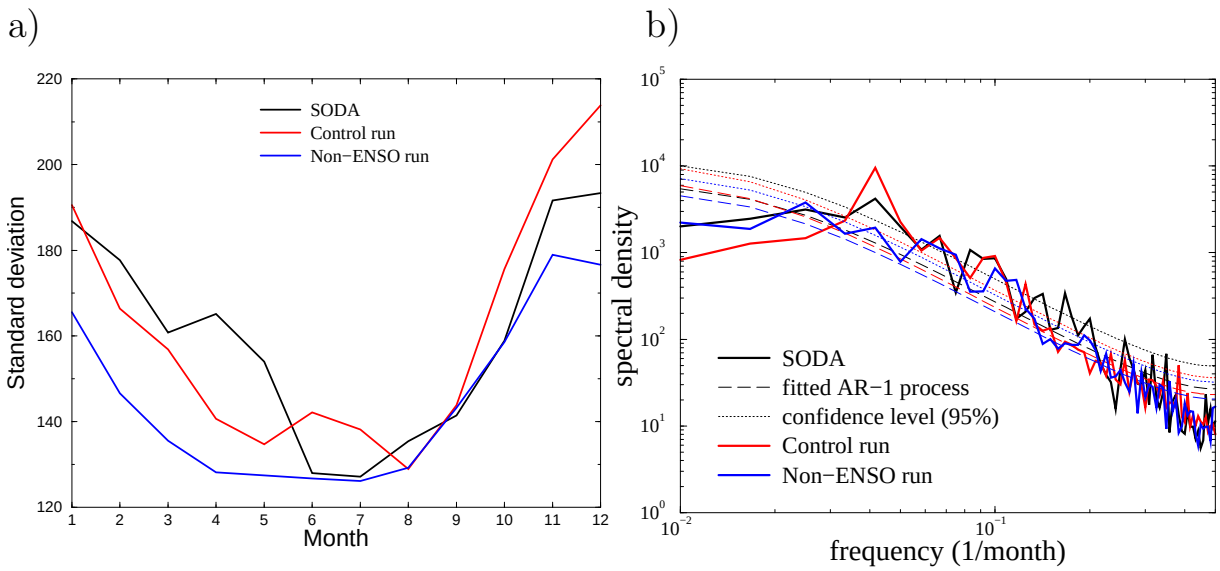

Figure 4.6: (a) Standard deviation of heat content (in m°C) anomalies averaged in the southern central Indian Ocean (Soce index) as a function of calendar month and (b) spectra of the Soce index. Soce index from the SODA dataset, the control experiment and, the non-ENSO experiment. The dashed line denote the spectra of equivalent red noise processes and the dotted lines denote the 95% confidence level for accepting the red noise null hypothesis.

however, differences in phase and strength, with the minimum in the non-ENSO experiment being the broadest, and the variability of the non-ENSO experiment in November, December and January being 10 to 20% weaker than that of the control experiment.

The spectra for the Soce index in the two experiments and in the SODA dataset are shown in Fig. 4.6b. While for both the SODA dataset and the control experiment the index has a peak at a period of 25 months, the interannual variability in the non-ENSO experiment does not exhibit any dominant timescale. Thus, only in the presence of ENSO the Indian Ocean HC variability associated with the SIO Rossby waves has a spectrum that presents a peak of enhanced variability at interannual timescales. In the absence of ENSO, the Indian Ocean variability exhibits a spectrum consistent with red noise. A red noise spectrum implies that the ocean essentially integrates the stochastic forcing produced by the atmosphere, responding more robustly to the lower frequencies and thereby reddening the response spectrum. The 25-month period in the control experiment corresponds well with the ENSO period simulated by the ECHO-G model. The model's ENSO period is rather short; this deficiency could be due to the atmospheric component of the coupled model, as proposed by (Guilyardi et al. 2003). There is enhanced variability at periods of 10 to 20 months in the three datasets.

In summary, the model results suggest that a temporal oscillation, associated with Rossby wave activity is possible only when the coupled interactions are also allowed in the Pacific. These results are in line with the findings in the previous chapter, where it was shown that no peak in the spectrum of equatorial SST anomalies can be found when ENSO is subtracted. In the next sections, the similarities and dissimilarities in the spatial structure of the variability associated with the Rossby waves in the two ECHO-G experiments are investigated. Further insight into the characteristics of the Rossby waves and the associated subsurface temperature anomalies can be obtained by a composite analysis. Composite patterns at latitude 10°S of vertical temperature anomalies in the ocean related to the Rossby wave variability are shown in appendix A.

4.4 Atmospheric covariability with South Indian Ocean Rossby waves

To follow the time evolution of some atmospheric fields and their relationship with the time-space evolution of the HC variability, cross-correlation analyses were carried out. As the Indian Ocean variability exhibits a strong seasonality (see chapter 3), these analyses were performed with data stratified by calendar month. To represent the HC variability the December values of the Soce index (HC anomalies averaged over 8°S to 12°S, 75°E to 85°E; defined in section 4.3.2) are used and referred to as Soce-Dec index.

Figures 4.7, 4.8, and 4.9 show patterns of cross-correlation with respect to the Soce-Dec index for both the control and the non-ENSO experiments. The cross-correlations were computed for a 24-month period around December, Dec(0), namely the period between the previous January, Jan(0) to the next December, Dec(1). Dec(0) is the month for which the value 12 is assigned in the cross-correlation plots and the lag is zero. Dec(1) is the month for which the value 24 is assigned in the cross-correlation plots and Soce-Dec index leads by 12 months. Unless stated otherwise, the correlations in the Pacific sector are computed against equatorial quantities.

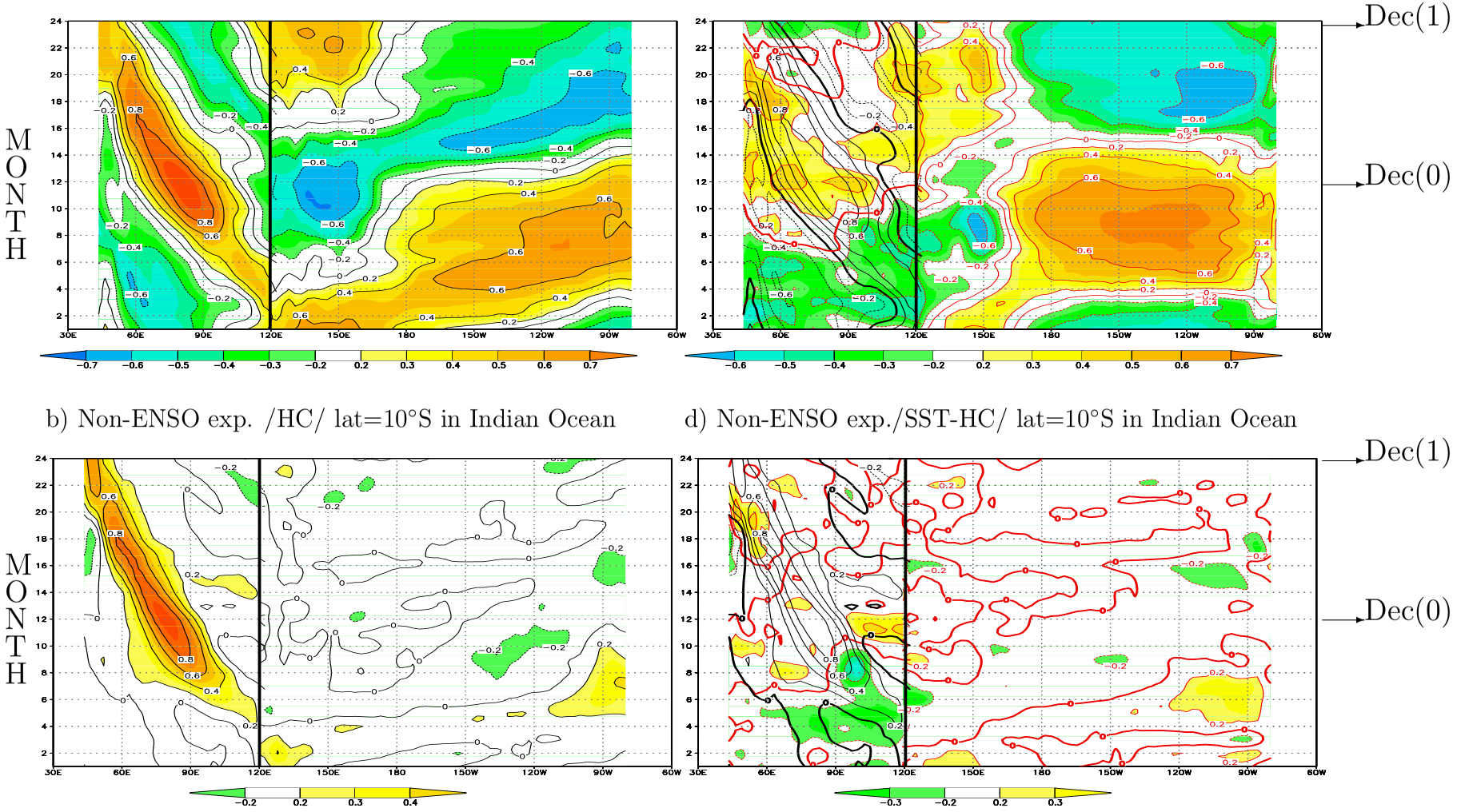

Figure 4.7: Lagged correlations of HC and SST anomalies at latitude 10°S in the Indian Ocean with the Soce-Dec index as a function of longitude and calendar month, for both the control and the non-ENSO experiments. The left panels (a and b) are for correlations of HC anomalies. The rigth panels (c and d) are for correlations of SST anomalies. The top panels are for the control experiment and the bottom plots are for the non-ENSO experiment. SST and HC anomalies in the Indian Ocean sector are at 10°S. In the rigth panels (c and d) the HC correlation at 10°S in the Indian Ocean sector is replotted in black contours. SST and HC correlations in the Pacific Ocean sector are for anomalies are at the equator, and are included to allow a comparison of the correlation magnitudes in the Indian Ocean and Pacific regions.

4.4.1 SST and heat content

The cross-correlations of Soce-Dec and HC anomalies for the control experiment (Figs. 4.7a) and for the non-ENSO experiment (Fig. 4.7b) show the expected westward propagation characteristic of Rossby waves with a maximum that starts at 90°E in Sep(0) and reaches 60°E in Jun(1). For the control experiment, the HC anomalies in the equatorial Pacific are significantly positively correlated with the Soce-Dec index. This correlation starts in Jun(0), six months before Soce-Dec peaks. Along with the high positive correlations of Soce-Dec with HC in the Pacific, high correlations with SST and the atmospheric fields (wind stress, wind stress curl, precipitation) are found in the Pacific (Figs. 4.9a, c, and e). Thus, the model Rossby wave variability in the Indian Ocean is closely related to the changes in the tropical Pacific.

Copropagation of SST and HC anomalies (Figs. 4.7c and 4.7d) west of 60°E is observed between May(1) and Sep(1) for both control and non-ENSO experiments. However, the correlations are smaller in the non-ENSO experiment. This indicates that an upwelling region with a shallow thermocline exists in the control experiment in the region at 10°S, west of 60°E. The effects of the wave propagating at 10°S can be seen 1 to 2 seasons after the Soce-Dec index peaks in Dec(0). Such positive SST anomalies in that region contemporary with or earlier than Soce-Dec's peak in Dec(0) are produced by processes other than the effect of the Rossby wave on the thermocline depth. Such a process could be local Ekman pumping. This topic will be discussed below. Additionally, in the first stage of the Rossby wave propagation at 10°S, from Oct(0) to Apr(1), the correlation patterns for the two experiments are different. While for the non-ENSO there is no copropagation, for the control experiment there is copropagation. However, compared to the SODA dataset (XASM), the control experiment exhibits an SST cross-correlation pattern with lower values. This is likely due to a too deep thermocline in the model (see Fig. 4.2a).

When ENSO is included in the simulations, i.e. in the control experiment, the SST anomalies are positively correlated with upper ocean HC anomalies at zero lag in the central part of the Indian Ocean basin at latitude 10°S (Fig. 4.7c). This reflects the fact that the equatorial SST anomalies are linked to perturbations in the local thermocline depth. At the same zero lag there are high correlations with SST and HC anomalies in the equatorial eastern Pacific, revealing the strong linkage of the anomalies in the Indian

Ocean with ENSO in the Pacific. Note, however, that the highest correlation of Soce-Dec index and SST in the equatorial Pacific occurs with Sep(0) SST in the eastern Pacific. The temporal evolution of upper ocean heat content in the control experiment indicates an oscillatory behaviour of approximately 24 months, which is consistent with the period of enhanced variability in the spectrum of the Soce index for the control experiment (Fig. 4.6b). On the other hand, the non-ENSO experiment fails to reproduce the high zero lag correlation of SST and HC anomalies at 10°S in the Indian Ocean basin and oscillatory behaviour is hardly detectable in this simulation (Fig. 4.7d).

Latif et al. (2001, hereafter LENSIP) performed an intercomparison study of twenty-four coupled models with respect to their performance in the equatorial Pacific. They found that the ENSO variability is too regular in many models. Figure 5 in LENSIP showed that observations reveal a negative correlation of equatorial SST and HC anomalies in the Pacific at lags of about 10 to 20 months, indicating the oscillatory nature of ENSO. Many coupled models, however, overestimate this negative correlation. This shortcoming arises also in the ECHO-G model. The control experiment simulates a quite strong negative correlation in the equatorial eastern Pacific (and in the central and western Indian Ocean at 10°S) at lags greater than 10 months (Fig. 4.7c). Thus, such as found for many other models in the LENSIP study, the variability in ECHO-G is too regular, although the reason for this is unclear. The LENSIP study, based on the studies by Eckert and Latif (1997) and Chang et al. (1994), suggested two potential causes: a too low noise level in the atmospheric component, which may lead to too regular behaviour in SST and the phase-locking of ENSO to the annual cycle. This problem consists in that a simulation may be in a chaotic or strongly phase-locked regime, depending on the strength of the annual cycle.

To check if there is some westward copropagation of anomalies at other south tropical latitudes related with the wave at 10°S, the correlations of SST and HC with Soce-Dec were produced for SST and HC anomalies at 5°S and at the equator (Fig. 4.8). For the control experiment, the correlation patterns at both latitudes (Fig. 4.7a for latitude 5°S and Fig. 4.9c for the equator) indicate copropagation of SST with HC. For both patterns positive SST anomalies are developing in the western Indian Ocean in Jun(0), extending to the entire basin in Dec(0) and staying in the corresponding band of latitude for all longitudes until Jun(1). For the non-ENSO experiment, the SST correlations at both

latitudes (Fig. 4.8b for latitude 5°S and Fig. 4.8d for the equator) are small, so that it is not possible to recognize any propagating structure.

4.4.2 Wind stress and wind stress curl

Figures 4.9a and b show the cross-correlation of Soce-Dec index with wind stress anomalies averaged from 2°S to 8°S in the Indian Ocean and in the Pacific sector. The maximum equatorial south-easterlies in the Indian Ocean occur from Jun(0) to Dec(0) in both simulations. In the non-ENSO experiment they are confined to the east of 60°E, except in Jul(0). In the control experiment, southeasterlies extent to the west of 70°E from Jun(0) to Dec(0). These southeasterlies produce WSC anomalies that force anomalous local Ekman pumping that reduces upwelling and deepens the thermocline in the west. Since the region west of 70°E between 10°S and 5°S is an upwelling region with a shallow thermocline, a deepening in the thermocline leads at least partially to positive SST anomalies, which is consistent to what is shown in Figs. 4.7a, 4.7c, 4.8a and 4.8c.

As expected from the figures showing the wind stress cross-correlations, in both experiments there are positive WSC anomalies in the eastern half of the basin from Jun(0) to Dec(0). However, for the control experiment, from Jun(0) to Dec(0), there are additionally positive WSC anomalies also at the western half of the basin. For both experiments, the strongest anomalous WSC occurs in the eastern half of the basin from Aug(0) to Nov(0), coinciding with the maximum easterlies in the equatorial Indian Ocean (Figs. 4.9a and b). Until Apr(1) the WSC correlation pattern shows a standing structure without any obvious zonal propagation in both the control experiment and non-ENSO experiments. There is, however, a slight propagation of negative WSC anomalies in both experiments from May(1) to Sep(1). For that period, the intensity of the correlations for both experiments is relatively small as it does not exceed 0.4. However, the correlation coefficients are significantly smaller (by 0.2) in the non-ENSO experiment.

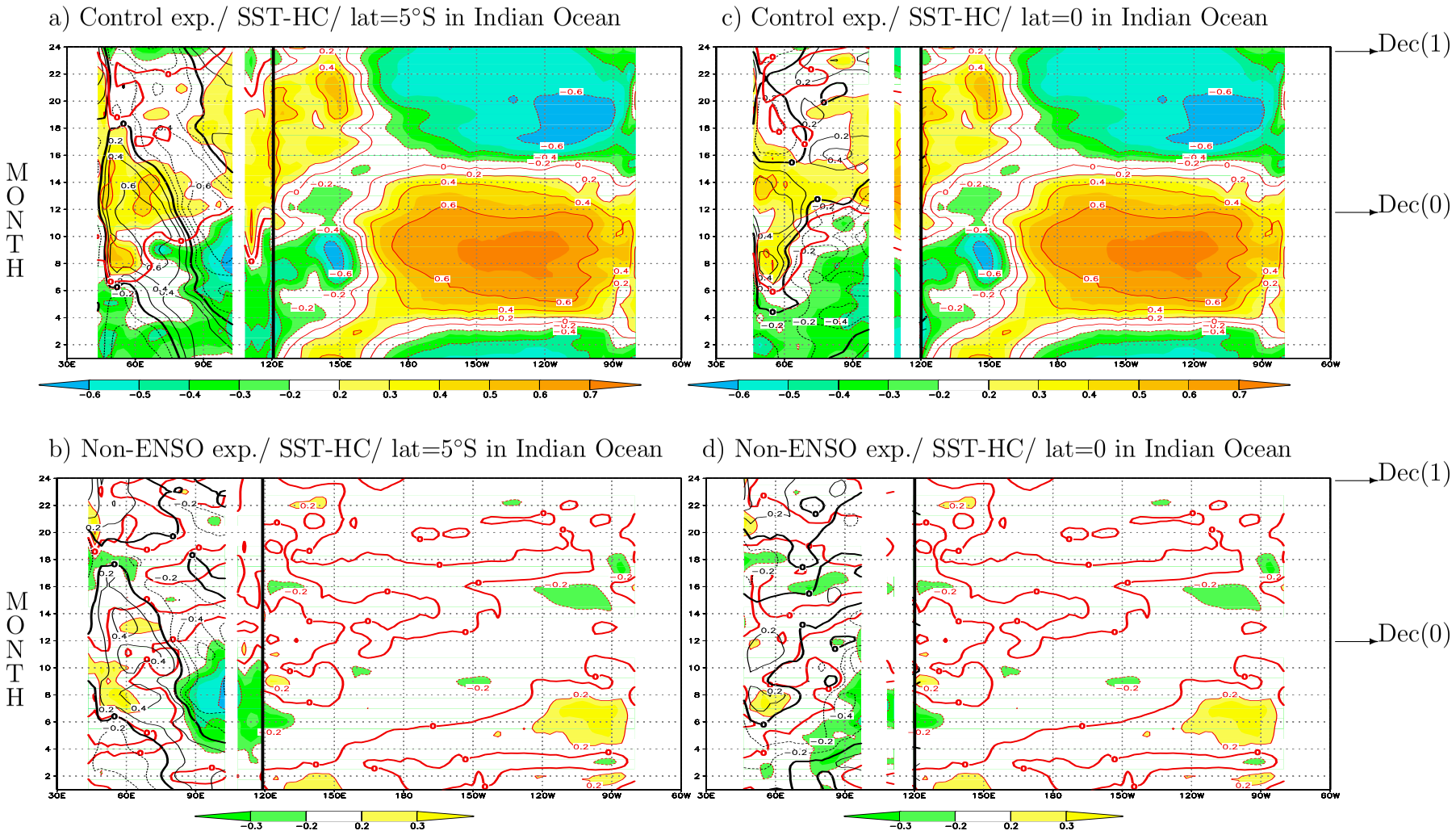

Figure 4.8: Lagged correlations of SST (shaded) and HC (black contours) anomalies at two different latitudes in the Indian Ocean with the Soce-Dec index as a function of longitude and calendar month, for both the control and the non-ENSO experiments. The left panels (a and b) are for SST and HC correlations at latitude 5°S in the Indian Ocean. The rigth panels (c and d) are for SST and HC correlations at the equator in the Indian Ocean. The top panels are for the control experiment and the bottom plots are for the non-ENSO experiment in the Indian Ocean. SST correlations in the Pacific Ocean sector are for anomalies at the equator, and are included to allow a comparison of the correlation magnitudes in the Indian Ocean and Pacific regions. Panels a and c here are comparable with Fig. 4.7c. Panels b and d here are comparable with Fig. 4.7d.

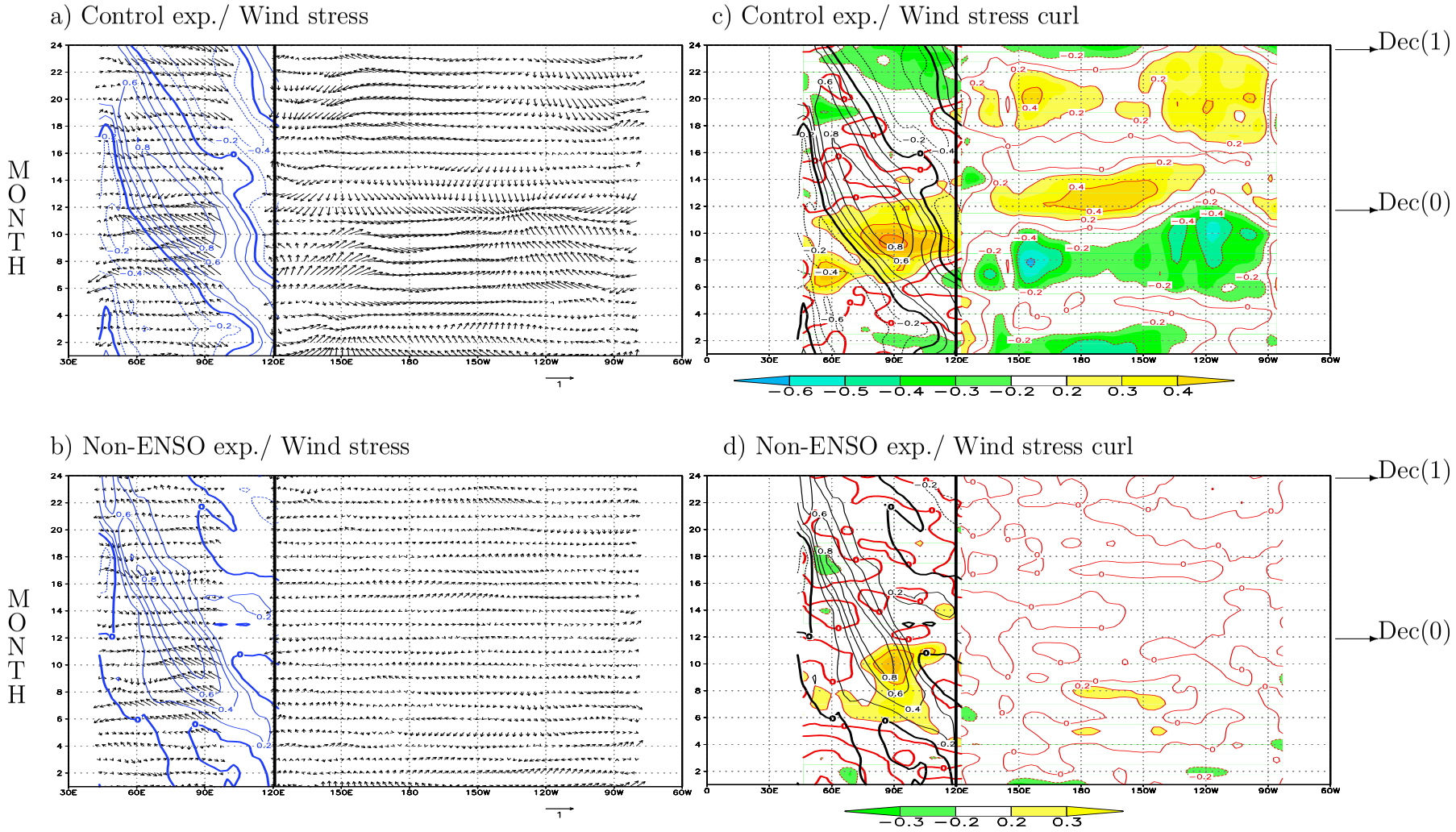

Figure 4.9: Lagged correlations of wind stress (WS) anomalies averaged in 2°S to 8°S and wind stress curl (WSC) anomalies at 10°S in the Indian Ocean with the Soce-Dec index as a function of longitude and calendar month, for both the control and the non-ENSO experiments. The left panels (a and b) are for WS correlations (vectors). The rigth panels (c and d) are for WSC correlations (shaded). The top panels are for the control experiment and the bottom plots are for the non-ENSO experiment in the Indian Ocean. HC correlation at 10°S in the Indian Ocean sector is replotted in black contours. WS and WSC correlations in the Pacific Ocean sector are for anomalies averaged in 3°N to 3°S, and are included to allow a comparison of the correlation magnitudes in the Indian Ocean and Pacific regions.

4.4.3 Precipitation

Figures 4.9e and f show correlation coefficients of precipitation anomalies at 10°S with Soce-Dec. From Jul(0) to Nov(0), there are negative anomalies east of 80°E, in both experiments. From May(1) to Jul(1) there is a weak copropagation of the precipitation anomalies with the Rossby wave in the control experiment. This is an indication of the mechanism found in XASM using SODA and NCEP reanalyses. The mechanism consists

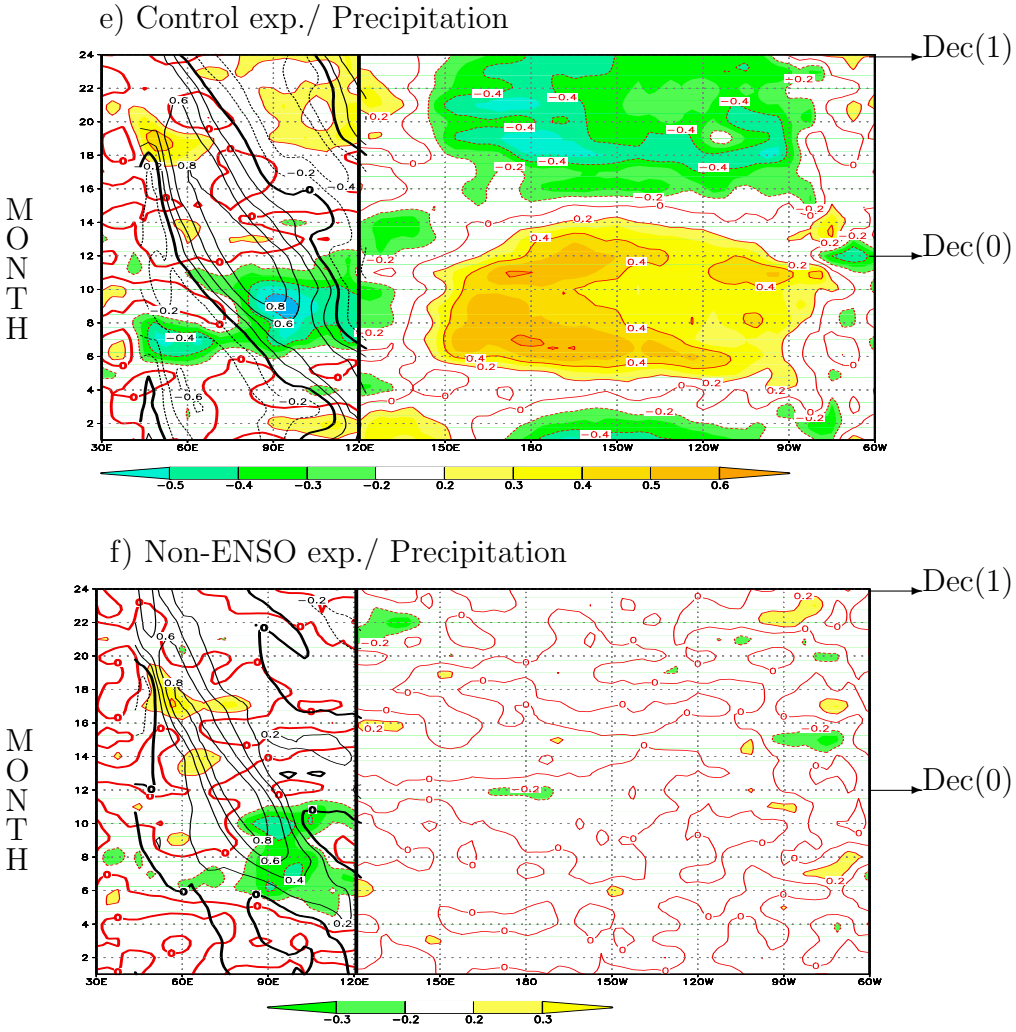

Figure 4.9: (Continued) Lagged correlations of precipitation anomalies at latitude 10°S in the Indian Ocean with the Soce-Dec index as a function of longitude and calendar month, for both the control and the non-ENSO experiments. The top panel (a) is for the control experiment and the bottom panel (b) is for the non-ENSO experiment in the Indian Ocean. HC correlation at 10°S in the Indian Ocean sector is replotted in black contours. Precipitation correlations in the Pacific Ocean sector are for anomalies at the equator, and are included to allow a comparison of the correlation magnitudes in the Indian Ocean and Pacific regions.

of positive precipitation anomalies and a cyclonic surface circulation collocated with a positive thermocline and SST anomalies. The interaction between these fields is a negative feedback that quickly dampens the Rossby wave. However, the mechanism starts to operate in Apr(1) for the datasets used in XASM and two months later for the control experiment.

In summary, for the two experiments, it was not possible to find evidence of positive WSC anomalies copropagating with positive SST anomalies and the downwelling Rossby wave at 10°S. From May(1) to Jul(1) there is a weak copropagation of positive HC-SST-precipitation anomalies with negative WSC anomalies in the control experiment, which is an indication of the *negative* thermocline feedback found by XASM. For the non-ENSO experiment, no copropagation was found.

4.5 Sea level pressure and Rossby wave forcing

Additional insight into the characteristics of the forcing mechanism of Rossby waves can be obtained through the regression maps of mean sea level pressure (SLP) anomalies associated to the precursor patterns of the POP pairs (p^I; left panels in Figs. 4.3a, 4.3b and 4.4a). The regression patterns associated with p_1^I (Fig. 4.10a) and p_2^I (Fig. 4.10b) in the control experiment have a common feature with the regression patterns associated with $p_{1'}^I$ (Fig. 4.10c) in the non-ENSO experiment: the three regression patterns show positive SLP anomalies extending from the south eastern Indian Ocean across Australia to the Pacific region west of Australia. For the control experiment, the regression patterns have lobes of positive SLP anomalies on each side of the equator in the central-western Pacific sector off the equator surrounding negative SLP anomalies in the Niño3 region. The SLP regression patterns associated with the POP patterns bear a great resemblance to the Southern Oscillation in the control experiment. The atmospheric circulation anomalies derived by the SLP regressions (Fig. 4.10) suggest that for both experiments there is a relationship between positive anomalies of SLP over the southeastern tropical Indian Ocean and the excitation of Rossby waves in the SIO. The atmospheric circulation anomalies are associated with positive SLP anomalies, which are related to southeasterlies south of the equator and easterlies at the equator, which can produce both negative SST anomalies in the eastern Indian Ocean through equatorial and coastal upwelling, and westward Rossby waves that deepen the thermocline through anomalous wind stress curl forcing.

The positive anomalies of SLP over the southeastern tropical Indian Ocean might also explain the linkage between ENSO activity and the excitation of Rossby waves. For instance, during an El Niño event, the Southern Oscillation is associated with positive SLP anomalies in the southeastern part of the tropical Indian Ocean. These results show that ENSO produces conditions favorable for the excitation of Rossby waves in the SIO, which is consistent with the analyses by XASM. Thus, the linkage between ENSO and the development of SIO Rossby waves can be explained by the effect of positive anomalies of SLP over the southeastern tropical Indian Ocean through anomalous wind stress curl forcing.

The development of SIO Rossby waves in the SIO seems to imply interannual variability in the Pacific at two different timescales. One timescale corresponds to the dominant timescale of ENSO (in the model, it is about 25 months) and the other one corresponds to the secondary timescale (17 months approximately). This is supported by the good agreement between SLP spatial pattern characteristic of the Southern Oscillation and the two regression patterns of the SLP anomalies (Fig. 4.10a and b) corresponding to p_1^I (Fig. 4.3a) and p_2^I (Fig. 4.3b) patterns. Experiments with coupled models simulating a more realistic ENSO period will be required to confirm this finding.

The major forcing of the SIO Rossby waves is associated with interannual SST variability in the Pacific. From Figs. 4.7c and d and from the POP analyses (Table 4.1) it can be seen that the SST variability in the eastern Indian Ocean that is associated with interannual SST variability in the Pacific (i.e. in the control experiment) is related to a relatively high explained variance in the HC field in the Indian Ocean. This implies that SLP anomalies in the Indo-Pacific region related to the interannual SST variability in the Pacific, at both the dominant and the secondary timescales of ENSO, are associated with the major forcing of the waves. Furthermore, the interannual variability of the fields in the Indian Ocean is consistent with a cycle only if ENSO is included in the simulations.

Table 4.1: Statistics of the POP analyses of heat content (HC) anomalies as simulated in the two experiments with ECHO-G model. T= period of the POP mode, EV= variance explained by the POP mode.

	Control Experiment	Non-ENSO experiment
pop1	T=17 months EV=12%	T=16 months EV=6%
pop2	T=30 months EV=16%	————

a) Control exper./ regression with respect to z_1^I

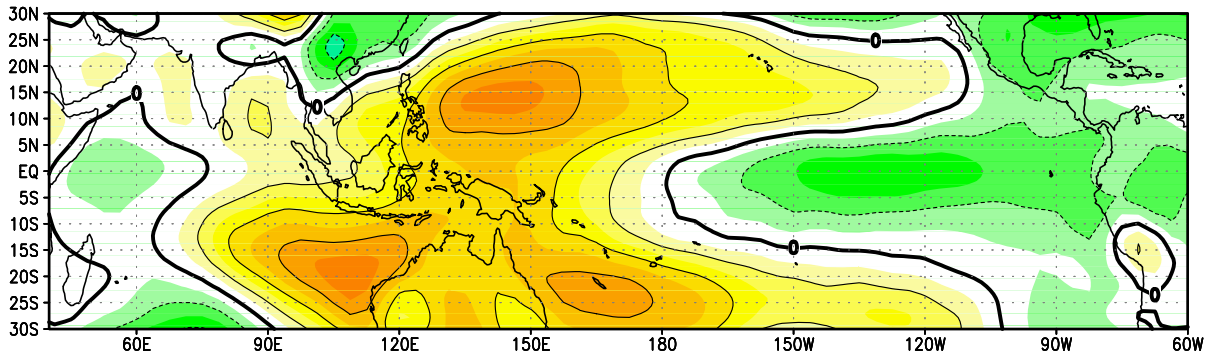

b) Control exper./ regression with respect to z_2^I

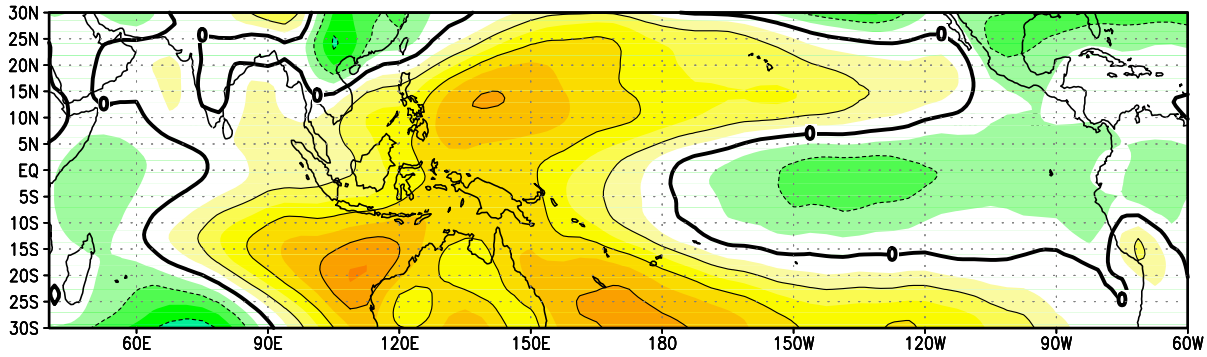

c) Non-ENSO exper./ regression with respect to $z_{1'}^I$

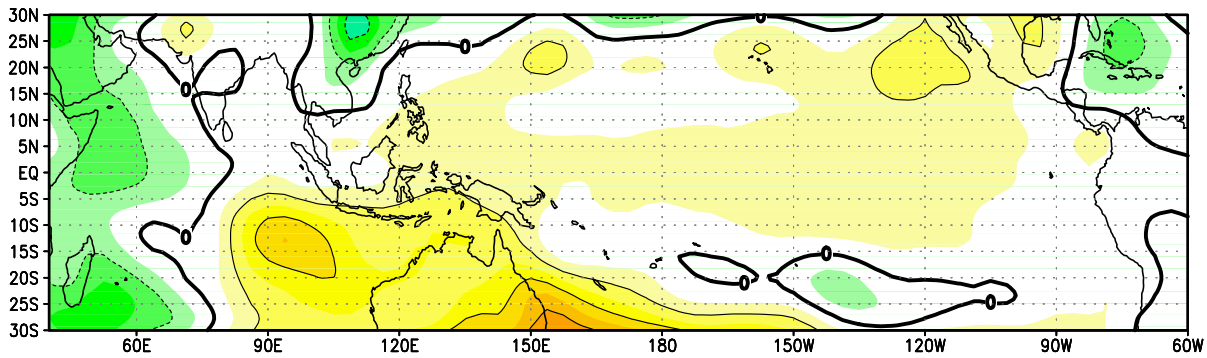

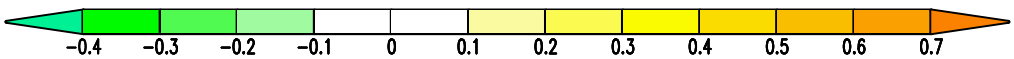

Figure 4.10: Regression maps of mean sea level pressure anomalies associated to the precursor patterns of the POP pairs shown in Fig. 4.3 for the control experiment and Fig. 4.4 for the non-ENSO experiment. (a) Pattern that goes along with p_1^I (left panel in Fig. 4.3 a). (b) Pattern that goes along with p_2^I (left panel in Fig. 4.3 b). (c) Pattern that goes along with $p_{1'}^I$ (left panel in Fig. 4.4 a).

4.6 Relationship between equatorial and off-equatorial Rossby waves and role of ENSO

It has been reported that equatorially trapped Rossby waves cause warming in the western Indian Ocean (Webster et al. 1999; Murtugudde et al. 2000) and that equatorially trapped Rossby waves and Rossby waves in SIO have been observed in the same years (XASM). In this section, the relationship of equatorially trapped to off-equatorial Rossby waves it is examined, and how they, in general, relate to HC variability at other latitudes. Also, it is investigated if ENSO plays a role in this relationship.

4.6.1 Equatorial western heat content variability

Equwe: an index for heat content in the equatorial western region

To track the variability associated with equatorial and near-equator Rossby waves in the two experiments an index, referred to as Equwe index (Equwe), is constructed from the monthly HC anomalies averaged over 5°S to 5°N, 50°E to 60°E. Figure 4.11 shows the standard deviation of the Equwe index as a function of calendar month for the two experiments and the SODA dataset. The standard deviation values of Equwe are approximately half of the values of the Soce index (Fig. 4.6a). In the control experiment, Equwe shows strong seasonal changes, with an increase in standard deviation of 40% from July to December. The Equwe index for the SODA dataset also shows strong seasonal changes. However, Equwe in SODA and in the control experiment have differences in phase and strength. For SODA (control experiment), the minimum occurs in November (July) and the maximum in January (December). The Equwe standard deviation values in SODA are larger (smaller) from January to March (August to December) than the corresponding values in the control experiment. With respect to the non-ENSO experiment, the Equwe values are, in general, smaller than the ones in the control experiment and seasonal changes are less pronounced. In this experiment, the minimum occurs in June and the maximum in March. The Equwe variability in the non-ENSO experiment, compared to the one in the control experiment, is drastically reduced from November to February. This implies that ENSO strongly increases the equatorial western HC variability in these months.

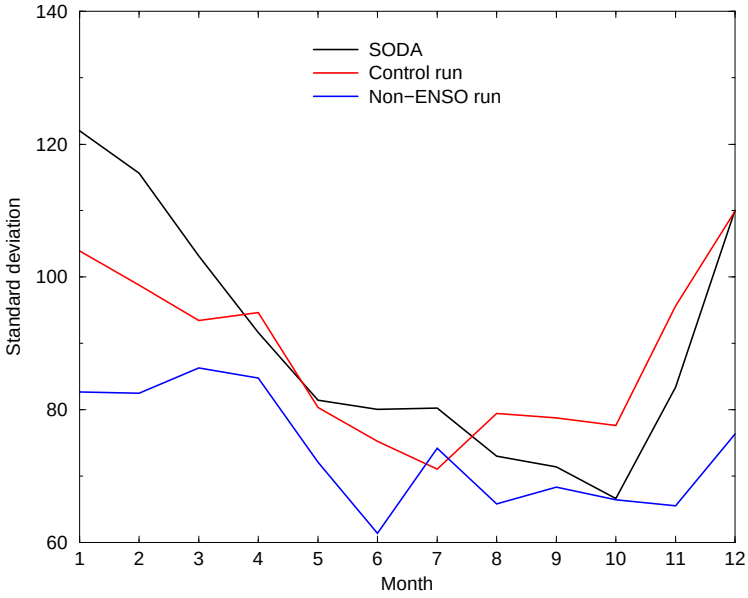

Figure 4.11: Standard deviation of heat content (m°C) anomalies averaged in the equatorial western Indian Ocean (Equwe index) as a function of calendar month.

Off-equatorial HC covariability with Equwe

To illustrate how the equatorial western HC anomalies covary with off-equatorial HC anomalies, a crosscorrelation is performed between HC along latitudes 10°S and 10°N and the December values of the Equwe index. For the control experiment, the crosscorrelations at both latitudes (Fig. 4.12a for latitude 10°S and Fig. 4.12c for latitude 10°N) show westward propagation, which is indicative of Rossby waves. There are, however, differences between the crosscorrelation maps: at 10°N, the magnitude of the correlations is smaller and positive anomalies in the middle part appear earlier. On the other hand, for the non-ENSO experiment, the correlations at both latitudes (Fig. 4.12b for latitude 10°S and Fig. 4.12d for latitude 10°N) are small. As they are not larger than 0.2 it is difficult to recognize any propagating or standing structure. Thus, in presence of ENSO in the Pacific, it is possible to recognize off-equatorial westward copropogation with equatorial HC anomalies. In absence of ENSO, there is neither copropagation nor covariability of equatorial and off-equatorial HC anomalies.

Sea level pressure associated with western equatorial HC variability

In this section, it is investigated why there is covariability of equatorial and off-equatorial HC anomalies in the control experiment but not in the non-ENSO experiment. Figure 4.13

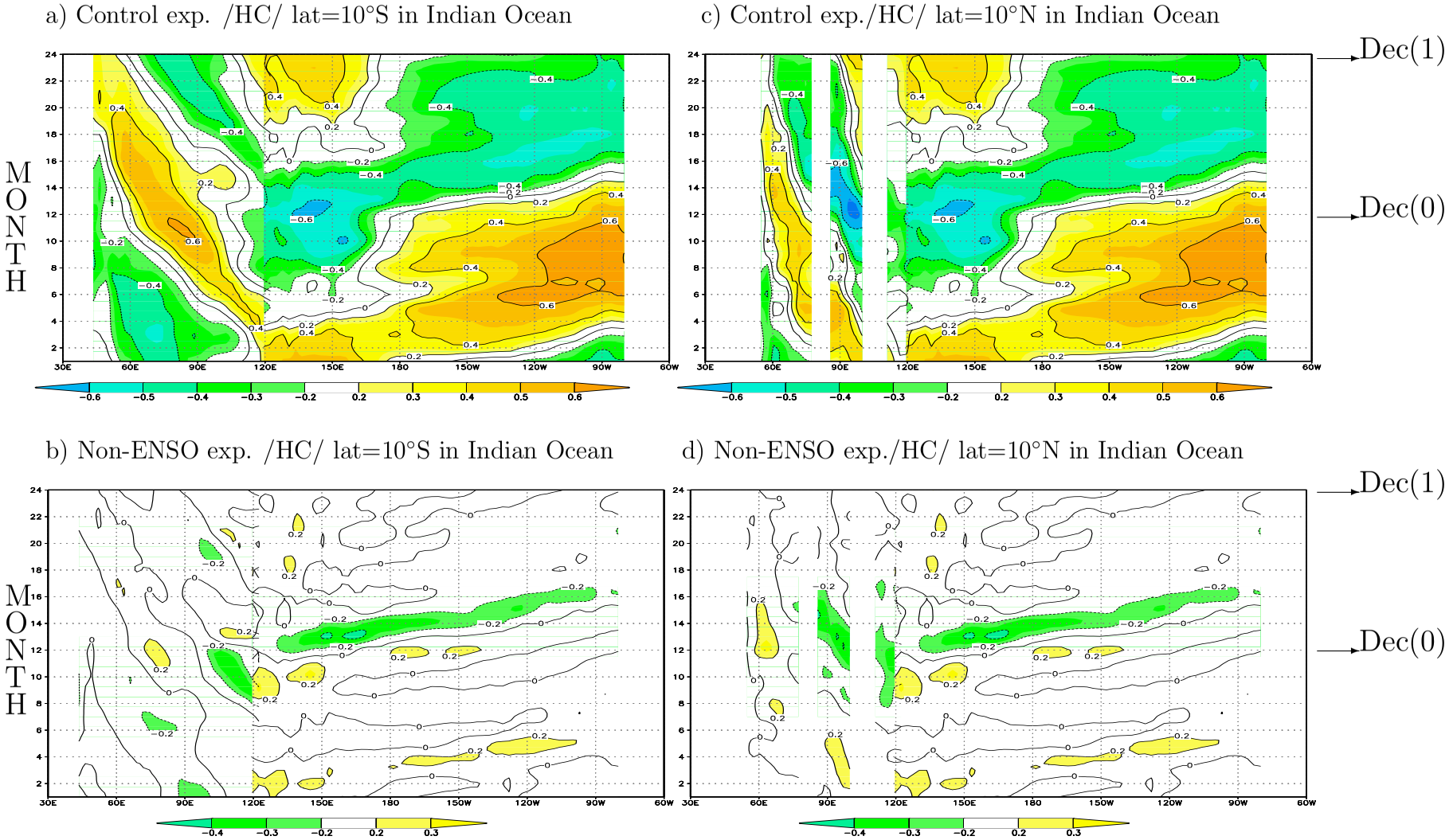

Figure 4.12: Lagged correlations of HC anomalies at latitudes 10°S and 10°N in the Indian Ocean with the Equwe-Dec index as a function of longitude and calendar month, for both the control and the non-ENSO experiments. The left panels (a and b) are for correlations of HC anomalies at 10°S. The right panels (c and d) are for correlations of HC anomalies at 10°N. The top panels are for the control experiment and the bottom plots are for the non-ENSO experiment. HC correlations in the Pacific Ocean sector are for anomalies at the equator, and are included to allow a comparison of the correlation magnitudes in the Indian Ocean and Pacific regions.

shows the SLP regression patterns associated with the Equwe index for both the control (Fig. 4.13a) and the non-ENSO (Fig. 4.13b) experiments. For the control experiment, a structure similar to the Southern Oscillation is found in the associated SLP regression pattern with respect to the Equwe index (Fig. 4.13a) and in the SLP regression patterns associated with pop1 and pop2 (Figs. 4.10a and b). This similarity implies that the link between the HC variability in the equatorial region and the HC variability in the SIO region is, at least partially, established through the anomalous surface winds induced by the Southern Oscillation. These winds can produce ocean Rossby waves, Ekmann pumping and advection at both sides of the equator in the Indian Ocean since the Southern Oscillation has a lobe of SLP anomalies at both sides of the equator.

The Southern Oscillation pattern obtained by regression with Equwe and z_1^I (Figs. 4.13a and 4.10a and b) is characterized in the Indian Ocean region by positive sea level pressure anomalies east of 60°E. The positive SLP anomalies north of the equator are less intense than the ones south of the equator. This asymmetry in intensity of positive SLP anomalies of the Southern Oscillation pattern could explain the asymmetry in intensity of the ENSO-forced off-equatorial Rossby waves observed by XASM. However, although in the Indian Ocean region east of 60°E there is an asymmetry in the intensity of the SLP anomalies in the Southern Oscillation pattern, SLP anomalies exist at both sides of the equator over the whole band of latitudes from 30°S to 25°N. Thus, the Southern Oscillation spatial distribution in the Indian Ocean includes positive SLP anomalies over the equator and north of the equator, which are completely absent in the regression patterns for the non-ENSO experiment (Fig. 4.13b). For the non-ENSO experiment, the associated regression SLP pattern with respect to Equwe shows a predominance of negative SLP anomalies, which extend into the Asian continent. Only in the southeastern region west of 90°E and north of 5°S there is some indication of weak positive anomalies.

Comparing the regressions with respect to Equwe and $z_{1'}^I$ time series (Figs. 4.13 and 4.10) for the non-ENSO experiment, it is noticed that relative high positive SLP anomalies east of 80°E south of 5°S are present only for the regression with respect to $z_{1'}^I$. These positive SLP anomalies were found to be associated with WSC anomalies forcing the SIO Rossby waves (see section 4.5). This dissimilarity in the eastern half of the basin of the SLP patterns associated with the equatorial and SIO HC variability suggests that the absence of a link through the wind field in the non-ENSO experiment is associated with

a lack of covariability of equatorial western HC with the HC in the SIO region. On the other hand, for the control experiment, there is a link through the wind field and it is the Southern Oscillation, which assures wind forcing east of 60°E over the whole band of latitudes from 30°S to 25°N, which is an important determinant of the covariability of equatorial western HC with off-equatorial HC.

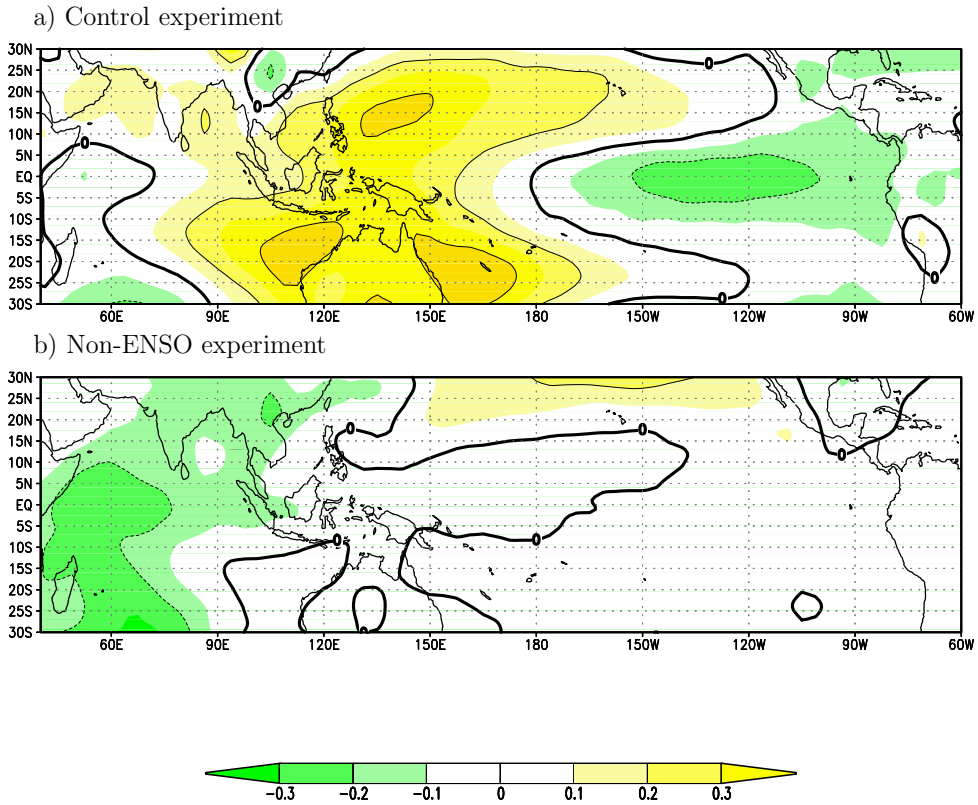

Figure 4.13: Regression patterns of sea level pressure anomalies (in Pa) associated with the Equwe index. (a) For the control experiment and (b) for the non-ENSO experiment.

4.6.2 Seasonal covariability according to Soce and Equwe indices

As it was shown in section 4.6.1, there is covariability of the western equatorial HC with off-equatorial HC in presence of interannual variability in the Pacific and that, such covariability do not occur in absence of interannual variability in the Pacific. Furthermore, in section 4.6.1 it was shown that the spatial distribution of the SLP anomalies involved in the Southern Oscillation is a main determinant of the covariability of equatorial HC with the off-equatorial HC.

In this section, the seasonal variability of some oceanic and atmospheric fields associated with the HC variability in two regions is presented through regression and composite maps. The regions are the equatorial western Indian Ocean region and the SIO region, which are represented by the Equwe-Dec and Soce-Dec indices, respectively. The fields are wind stress, SST, z20, net downward heat flux and SST tendency. The aim is to examine the relationship of the seasonal variability of the fields to the HC variability in the two regions and the contribution of surface flux forcing and ocean dynamics to the generation of SST anomalies.

Figure 4.14 shows the seasonal regression maps of SST, wind stress, and z20 anomalies for the control experiment and Fig. 4.15 shows the regression maps for the non-ENSO experiment. The upper panels of Figs. 4.14 and 4.15 show the regression maps with respect to the Soce-Dec index, and the bottom panels of Figs. 4.14 and 4.15 show the regression maps with respect to the Equwe-Dec index. The SST, wind stress, and z20 anomalies are averaged over the boreal fall (SON(0): September-October-November) of the year 0, the boreal winter (DJF(0/1): December-January-February), and the boreal spring (MAM(1):March-April-May) of the year 1.

Figures 4.16 and 4.17 show the composite patterns for the positive phase of the Soce index. The composites for the two experiments are obtained by averaging the seasonal anomalies corresponding to the events for which the Soce index is larger than 1.5 standard deviation. The SST seasonal tendency is defined as the difference between the first-month SST anomalies of two consecutive seasons: for example, the SST tendency for the boreal summer season (SON) is the difference between the anomalies in December and the anomalies in September.

The joint role of ocean dynamical mechanisms, such as advection by ocean currents, mixing, upwelling, Ekman effects, and the propagation of modal structures due to ocean dynamics is inferred from both the composite and regression analyses. The quantitative assessment of the effect of ocean dynamics, NDHF and changes in the mixed layer depth on the SST requires a heat budget analysis of the mixed layer. Since the quantities that enter into the model's mixed layer equation were not available, the description here is a first approximation to this assessment.

In the control experiment, the regression maps with respect to Soce (Figs. 4.14 a, c and e) and the ones with respect to Equwe (Fig. 4.14b, d, and f) show similar features over

the three seasons. This is consistent with the fact that in this experiment both indices are correlated (Fig. 4.12). In the non-ENSO experiment, by contrast, the regression maps show different spatial structures. The regression maps for the two experiments also differ with regard to the magnitude of SST anomalies. In the control experiment, SST anomalies with absolute value greater than +0.1 °C predominate. In the non-ENSO experiment, SST anomalies between +0.1 and -0.1 °C prevail.

a) Analysis for the control experiment:

In the region between 10°S and 10°N, the regression maps for SON (Figs. 4.14a and b) show a tongue of cold SST anomalies in the eastern half that penetrates westward along the equator, accompanied by negative thermocline depth anomalies, which suggests equatorial upwelling induced by the easterlies. The z20-SST-wind pattern is similar to that of the analyses by Saji et al. (1999) and XASM. This pattern is indicative of a Bjerkness-type feedback along the equator (XASM). In the western half, positive z20 anomalies colocated with positive SST anomalies prevail. The composite analysis for SON (Fig. 4.16a) shows that both the positive and the negative SST anomalies in the equatorial region are accompanied by SST-tendency anomalies with the same sign and NDHF anomalies with the opposite sign. This suggests that in the band of latitudes from 10°S to 10°N the SST anomalies are caused by oceanic processes such as Rossby waves, anomalous Ekman pumping, anomalous advection, anomalous vertical and horizontal mixing. Similarly, positive SST and SST-tendency anomalies and negative NDHF anomalies prevail in the western zones of the Arabian Sea and the Bay of Bengal, which indicates that also in these zones oceanic processes determine the SST anomalies. However, in the Arabian Sea the role of oceanic processes may be overemphasized, because the model shows high correlations between HC and SST that are not shown by the observations (Fig. 4.2). In the region south of 10°S and west of 90°E positive anomalies of SST, SST-tendency and NDHF prevail, which indicates that the anomalies fluxes are contributing, at least partially, to the formation of the SST anomalies.

The distribution of SLP anomalies on each side of the equator involved in the Southern Oscillation is manifested in SON. In this season, the equatorial region between 10°N and 10°S is characterized by wind stress anomalies over the whole band of longitudes. The magnitude of these wind stress anomalies increases polewards. These wind anomalies force Rossby waves at both sides of the equator, which contribute to the formation of

positive SST anomalies in the SIO upwelling region where the mean thermocline depth is shallow. Although z20 anomalies are forced on both sides of the equator, the magnitude of positive thermocline depth anomalies in the west is larger to the south.

For DJF(0/1) (Figs. 4.14c and d) and MAM(1) (Figs. 4.14e and f) the regression maps show a basin-wide warming. Such basin-wide warming has been noted in several studies, for example, Yu and Rienecker (1999) reported SST anomalies exceeding 1°C over most of the Indian Ocean north of 20°S for March of 1998, the final stage of a very strong positive ENSO extreme. In DJF(0/1) in the region north of 15°S and west of 75°E positive HC anomalies prevail whose north-south contrast is higher compared to the one in SON. In the region north of 5°S and east of 75°E negative HC anomalies prevail. With respect to SST, although there is basin-wide warming, different processes are causing the anomalies. In both the zone between the equator and 10°N and 60°E and 100°E and the zone south of 15°S positive SST-tendency and NDHF anomalies (Figs. 4.16b) prevail. This indicates that in these regions the warming in this season is at least partially due to increased NDHF, which is caused by weakening winds and reduced latent heat loss. The increased NDHF in the subregion located between the equator and 10°N and east of 80°E is consistent with the results by Venzke et al. (2000), who showed that solar radiative flux is an important agent in changing the SST in this region. In the zone located between 15°S and the equator and west of 100°E, the warming is caused by oceanic processes. These results are consistent with the ocean modelling study by Murtugudde et al. (2000) on the oceanic processes associated with the 1997–1998 El Niño event. The authors found that the warming in the western region from 15°S to 5°S was primarily due to meridional advection and decreased entrainment cooling caused by a downwelling Rossby wave packet centered at 8°S. The warming in the equatorial western region was caused by horizontal mixing.

In MAM(1), an important factor generating positive SST tendency anomalies and basin-wide warming (Figs. 4.14e and f and, Fig. 4.16c) is the increased NDHF in the central part of the SIO, the region between the equator and 15°S and 60°E and 100°E. This is consistent with the results by Venzke et al. (2000). Using a coupled GCM, they showed that NDHF is important in determining the large-scale changes of the Indian Ocean SST that occur about four months after the Niño3 SST anomalies peak. In the band of latitudes between the equator and 15°S, the degree of influence of positive NDHF

anomalies on the basin-wide warming depends on the range of longitudes considered. Two main zones are distinguished over this band of latitudes: the zone east of 70°E and the zone west of 70°E. In the first zone, the SST anomalies are produced by surface heat fluxes. In MAM(1), Rossby wave activity do not contribute to the positive SST anomalies in this zone, since negative z20 anomalies reveal a structure of upwelling. On the other hand, in the second zone, the Rossby waves do contribute to the positive SST anomalies since positive z20 anomalies exhibit a structure of downwelling and they are located in the upwelling zone with a shallow thermocline, where the thermocline can produce SST changes. Between 60°E and 70°E, both downwelling Rossby waves and NDHF contribute to SST anomalies, and in the zone west of 60°E, the contribution of the downwelling Rossby waves is higher since the NDHF anomalies are negative in this region. In the zone west of 70°E between 5°S and 15°S, there are indications of ocean-atmosphere coupling that involves the positive z20 anomalies induced by the SIO Rossby waves, since the positive z20 and SST anomalies (Figs. 4.14e and f) are colocated with anticyclonic WSC anomalies (Fig. 4.18) that in their turn reinforce the positive z20 anomalies.

b) Analysis for the non-ENSO experiment:

The regression patterns of the z20 anomalies with respect to both Soce and Equwe indices for three seasons (Fig. 4.15) are characterized by a moving east-west contrast of positive z20 anomalies in the west and negative z20 anomalies in the east. The magnitude of the negative z20 anomalies is smaller than the magnitude of the positive anomalies. For both SON(0) (Figs. 4.15a and b) and DJF(0/1) (Figs. 4.15c and d), the negative z20 anomalies in the east cover all latitudes north of 10°S. In MAM(1) (Figs. 4.15e and f), negative z20 anomalies off the equator are accompanied by weak positive anomalies over the equator. The tendency for westward propagation of positive z20 anomalies in the three seasons is reminiscent of downwelling Rossby waves.

The regressions for z20 anomalies with respect to the Soce index are characterized by an asymmetric latitudinal distribution: positive z20 anomalies are found basically south of the equator. On the other hand, the regression patterns for z20 anomalies with respect to the Equwe index show a spatial distribution roughly symmetric with respect to the equator, although the z20 anomalies are smaller in the north. Note that the difference in magnitude of the z20 anomalies in the western part shown in the regressions with respect to both Equwe and Soce indices could be produced by the asymmetric distribution of

the climatological z20 anomalies in the west. This distribution is characterized by an upwelling zone south of the equator between 2°S and 10°S, 50°E and 70°E (Fig. 4.2).

Concerning SST anomalies, in the regression maps with respect to both Soce and Equwe indices for the non-ENSO experiment predominate low SST anomalies in the three seasons, with absolute value less than 0.1°C. In the following, only regions with SST anomalies larger than this value will be considered.

The SON(0) regression pattern with respect to Soce (Fig. 4.15a) shows two regions with appreciable SST anomalies: the region off the coast of Sumatra and the region north of 5°S and west of 80°E. The regression pattern with respect to Equwe does not show appreciable SST anomalies anywhere in SON(0). In SON(0), the regression pattern with respect to Soce shows negative SST anomalies off the coast of Sumatra that are accompanied by equatorial easterlies, off-equatorial southeasterlies and negative z20 anomalies. Thus, as in the control experiment, the z20-SST-wind pattern associated with Soce-Dec in SON(0) is indicative of a Bjerkness feedback in the eastern region. The composite with respect to the Soce index (Fig. 4.17a) shows that negative SST-tendency and positive NDHF dominate in the region east of 90°E and north of 10°S, suggesting that the negative SST anomalies are produced by upwelling. The positive SST anomalies in the region north of 5°S and west of 80°E are colocated with positive SST-tendency and NDHF anomalies, implying that surface fluxes are important to form the SST anomalies over this region. Likewise, the SON(0) regression pattern with respect to Equwe (Fig. 4.15b) shows equatorial easterlies, off-equatorial southeasterlies and negative SST and z20 anomalies. However, the z20-SST-wind pattern does not seem to be indicative of a Bjerkness-type feedback, since the magnitude of the anomalies is low, in particular the SST anomalies are too low.

For DJF(0/1) the regression pattern with respect to the Soce index (Fig. 4.15c) shows that the region between 5°S and 10°S, 60°E and 70°E has positive SST anomalies, which are colocated with positive z20 and negative NDHF anomalies (Fig. 4.17). This indicates that oceanic processes such as downwelling Rossby waves form the SST anomalies. The regression pattern with respect to the Equwe index (Fig. 4.15d) shows that the region between 7°S and 7°N and west of 70°E has appreciable positive SST anomalies, which are colocated with positive z20 anomalies, which suggests that Rossby waves contribute to the SST anomalies. For MAM(1) the regression patterns with respect to both the Soce and Equwe indices (Fig. 4.15e and f) do not show appreciable SST anomalies anywhere.

Thus, for the non-ENSO experiment, although there are appreciable thermocline depth anomalies associated with the HC variability described by the Soce and Equwe indices in the three seasons, these anomalies do not necessarily imply SST changes.

In summary, the regression maps with respect to the Soce and Equwe indices show patterns that are similar in the control experiment and different in the non-ENSO experiment. The similarity in the control experiment implies a common forcing of the variability associated to each index and that ENSO is the common forcing. The ENSO signal in the Indian ocean includes both a dynamical and a thermodynamical response. Depending on the season and location it is possible to have warming either due to positive NDHF, due to oceanic processes, especially related to downwelling Rossby waves in the SIO, or due to a combination of both positive NDHF and oceanic processes.

The spatial distribution of the wind field implied by the Southern Oscillation produces a wind stress spatial distribution with anomalies roughly symmetric with respect to the equator. These wind stress anomalies force downwelling Rossby waves in the SIO region and, in general, HC anomalies, which in their turn contribute to the formation of SST anomalies.

From the analysis with the non-ENSO experiment, it was not possible to find evidence of an ENSO-independent structure of thermocline depth anomalies related to downwelling Rossby wave propagation that could be able to induce an organized space-time structure of positive SST anomalies. Positive anomalies in SST induced by Rossby wave activity were found, but they did not persist over more than one season and the atmosphere does not seem to feedback positively to these SST anomalies. Thus, no evidence was found for either *positive* or *negative* thermocline feedbacks involving SST and wind stress curl anomalies that take place in the western part of the Indian ocean and that are independent of the interannual variability in the Pacific.

For both the control and the non-ENSO experiments, it was found that the excitation of Rossby waves around 10°S is associated with negative SST and thermocline depth anomalies and easterly wind anomalies in the equatorial eastern Indian Ocean in SON(0). A similar joint development of these anomalies was found in reanalysis products by XASM and described as a Bjerknes-type feedback.

Control experiment/ SON(0):

a) Regression based on Soce-Dec

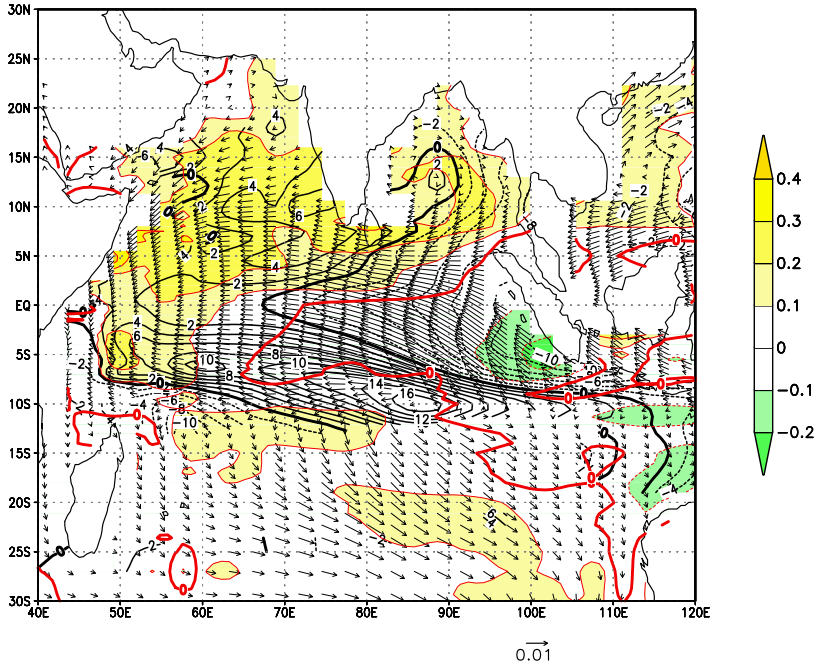

b) Regression based on Equwe-Dec

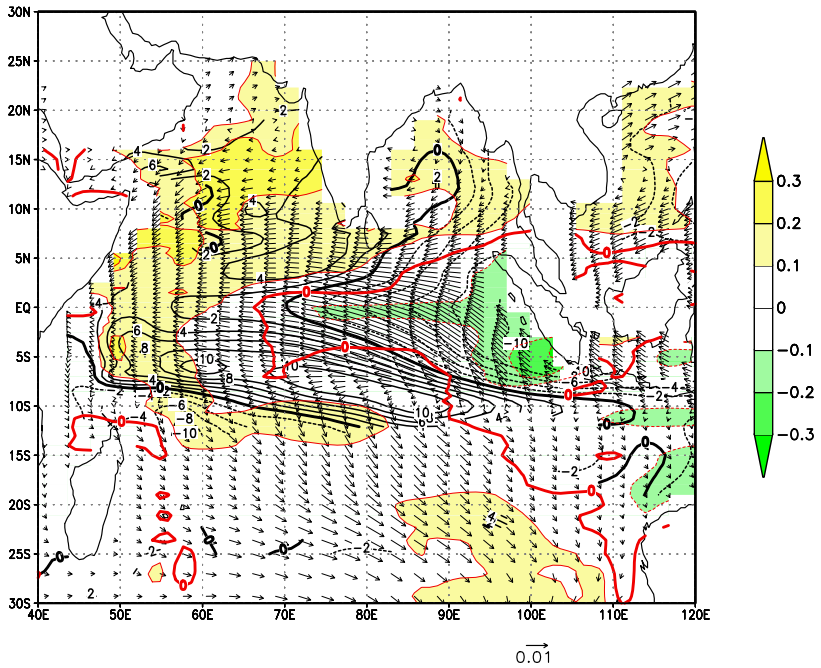

Figure 4.14: (top) Regresion coefficient of SST (shaded and red contours in $^{\circ}C$), wind stress (arrows in Nm^{-2}), and z20 (black contours in m) anomalies with respect to the Soce-Dec index. (bottom) Regresion coefficients with respect to the Equwe-Dec index. SST contour interval is 0.2. For z20 contour interval is 2. Anomalies are from the control experiment and seasonally averaged for SON.

Control experiment/ DJF(0/1):

c) Regression based on Soce-Dec

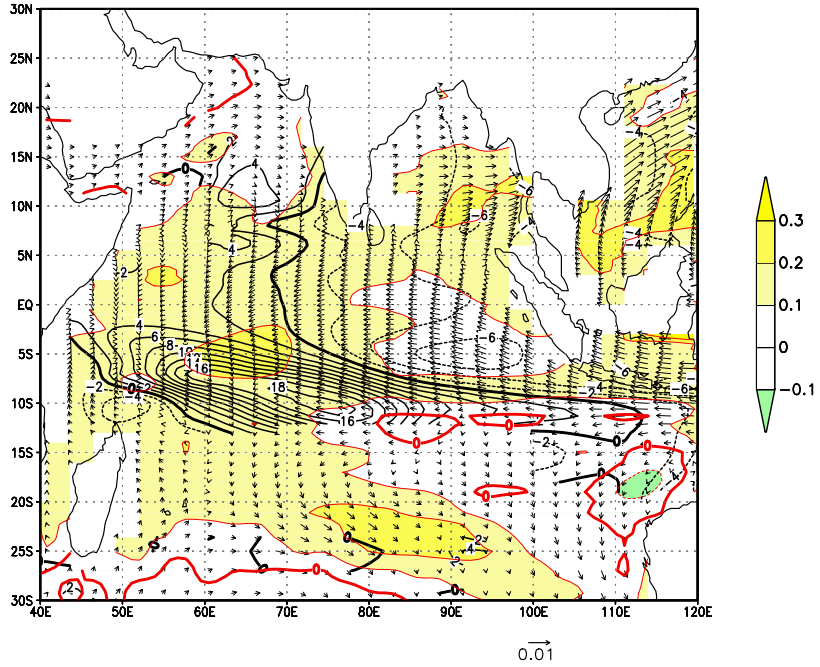

d) Regression based on Equwe-Dec

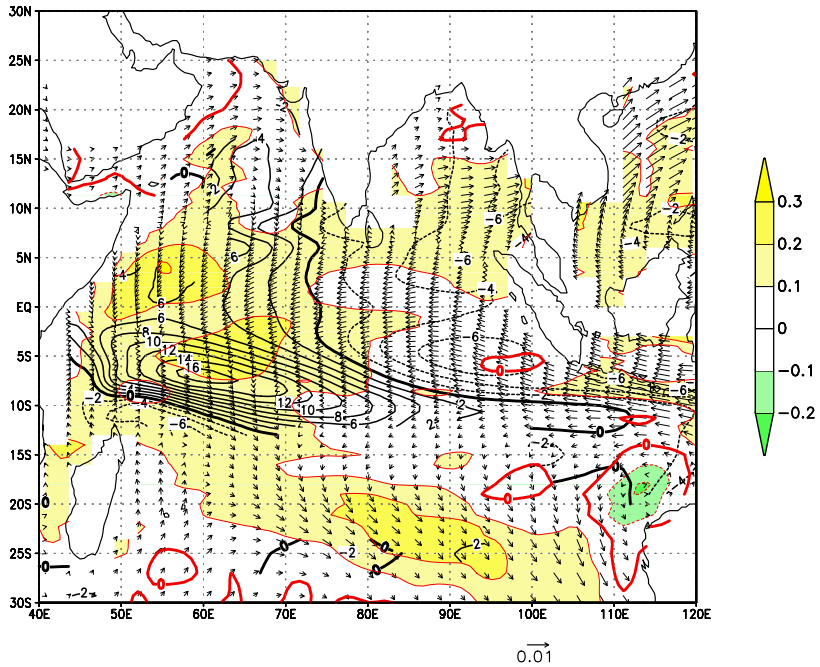

Figure 4.14: (continued) As in figure 4.14 a, except that anomalies are for DJF(0/1).

Control experiment/ MAM(1):

e) Regression based on Soce-Dec

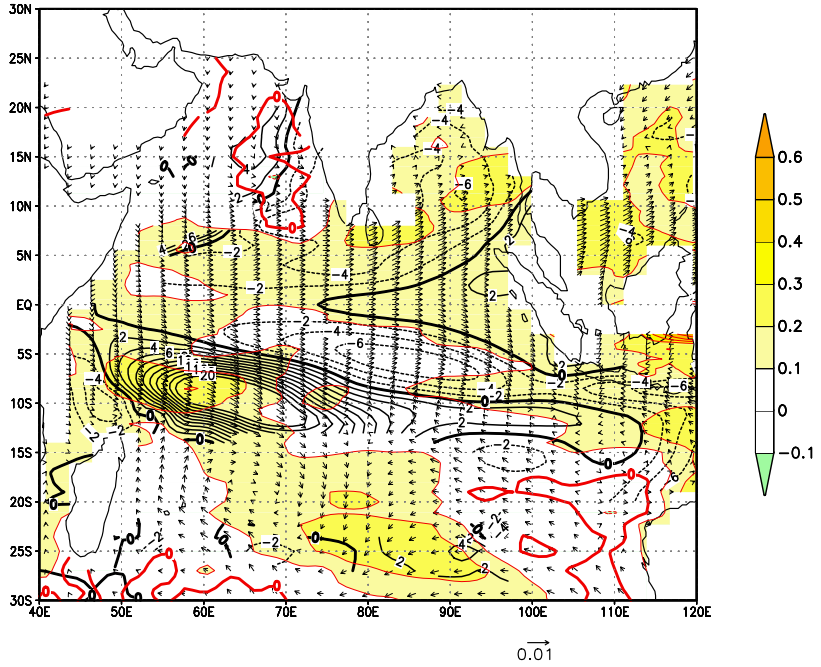

f) Regression based on Equwe-Dec

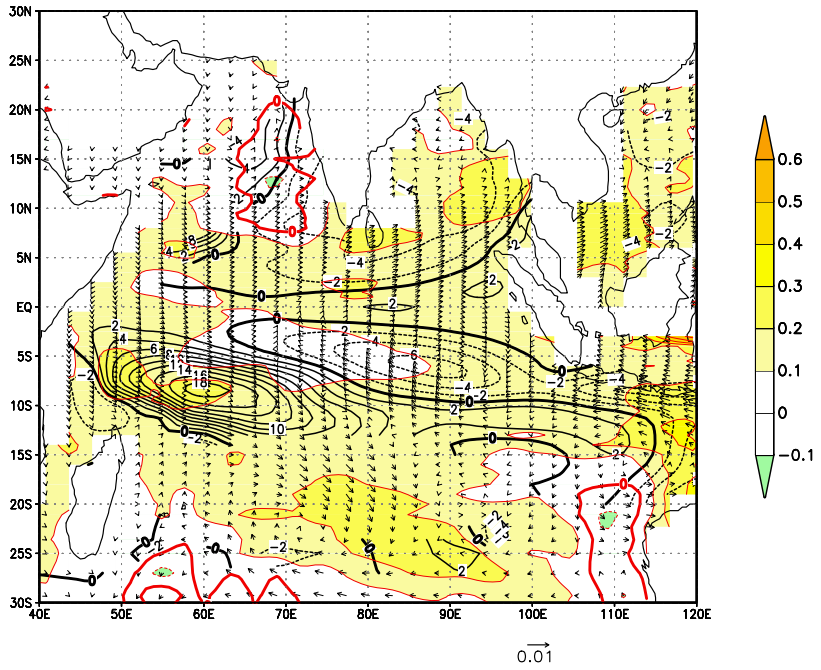

Figure 4.14: (continued) As in figure 4.14 a, except that anomalies are for MAM(1).

Non-ENSO experiment/ SON(0):

a) Regression based on Soce-Dec

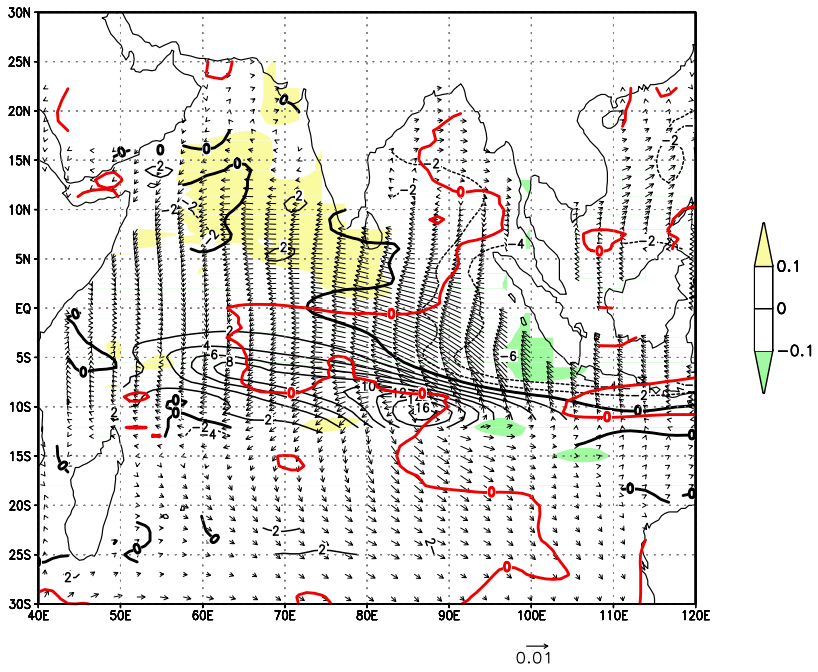

b) Regression based on Equwe-Dec

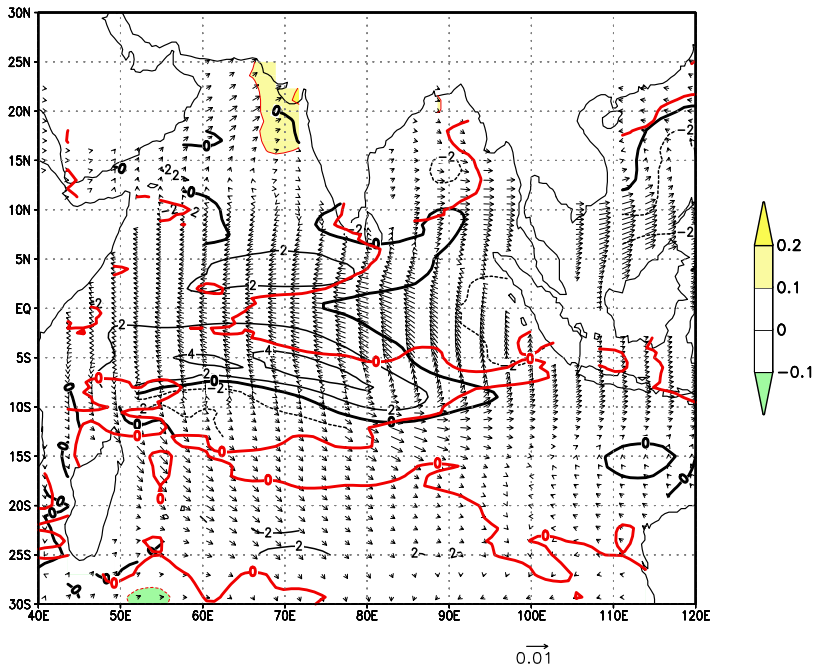

Figure 4.15: (top) Regresion coefficient of SST (shaded and red contours in $°C$), wind stress (arrows in Nm^{-2}), and z20 (black contours in m) anomalies with respect to the Soce-Dec index. (bottom) Regresion coefficients with respect to the Equwe-Dec index. SST contour interval is 0.2. For z20 contour interval is 2. Anomalies are from the non-ENSO experiment and seasonally averaged for SON.

Non-ENSO experiment/ DJF(0/1):

c) Regression based on Soce-Dec

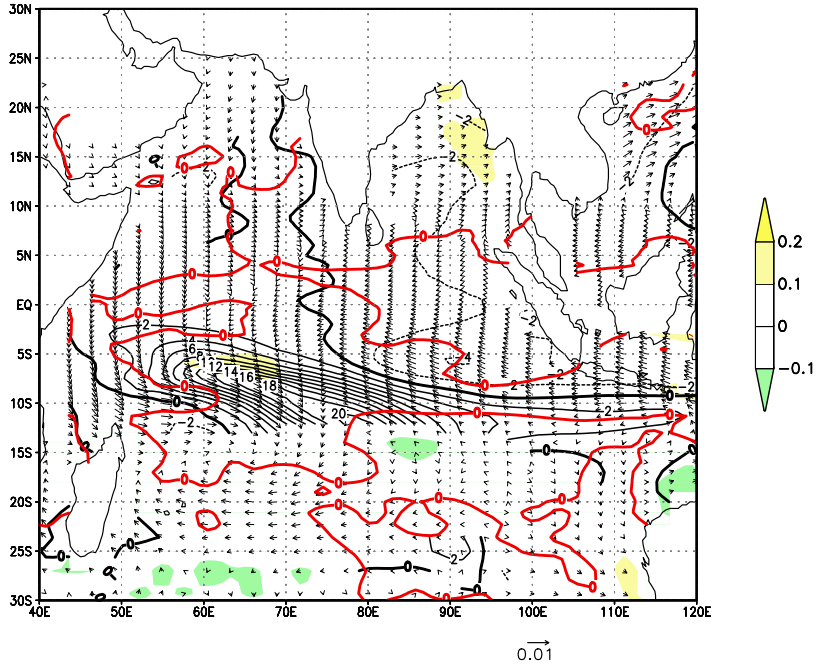

d) Regression based on Equwe-Dec

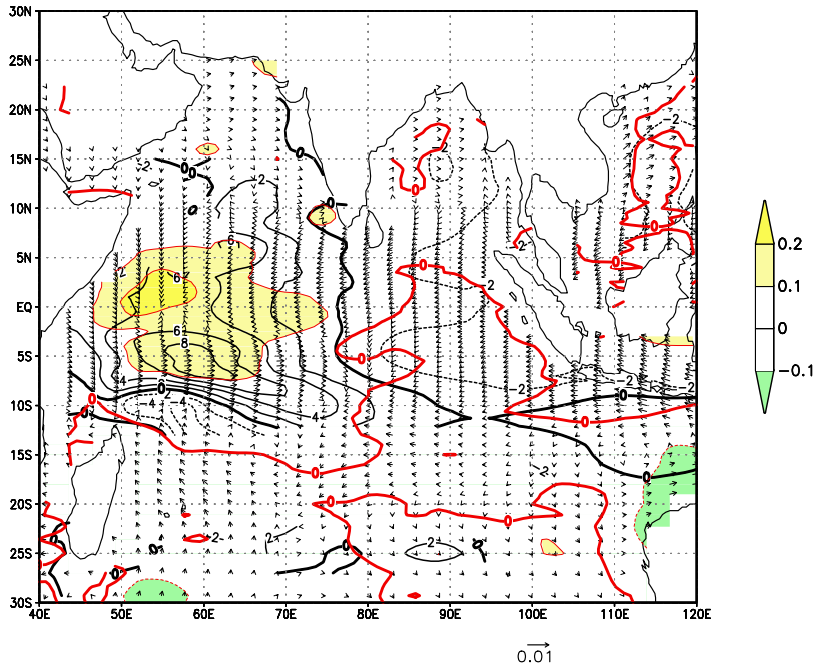

Figure 4.15: (continued) As in figure 4.15 a, except that anomalies are for DJF(0/1).

Non-ENSO experiment/ MAM(1):

e) Regression based on Soce-Dec

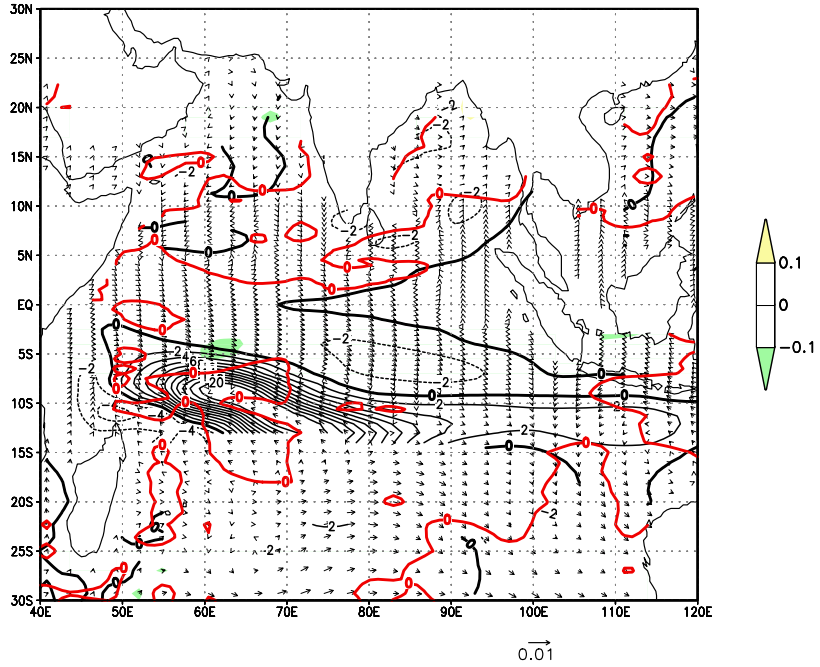

f) Regression based on Equwe-Dec

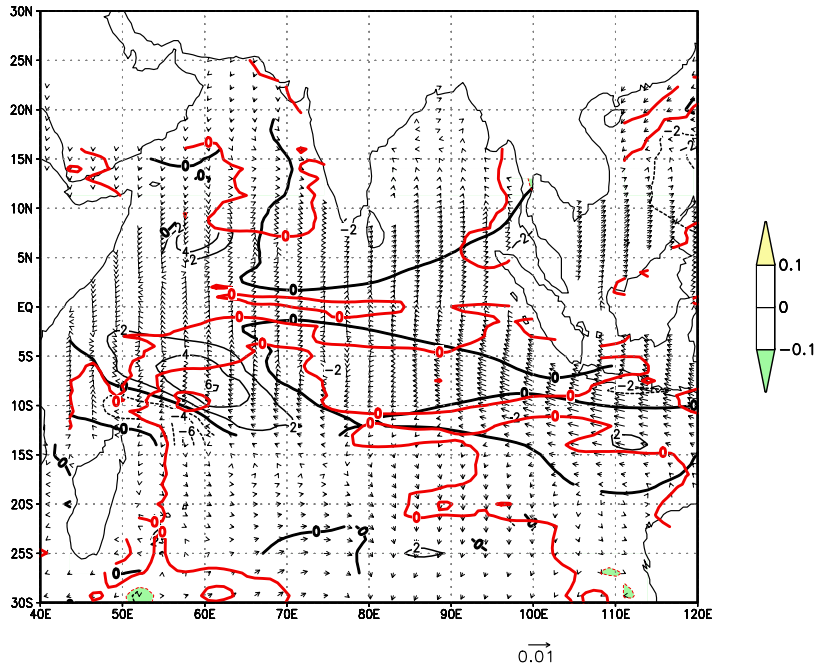

Figure 4.15: (continued) As in figure 4.15 a, except that anomalies are for MAM(1).

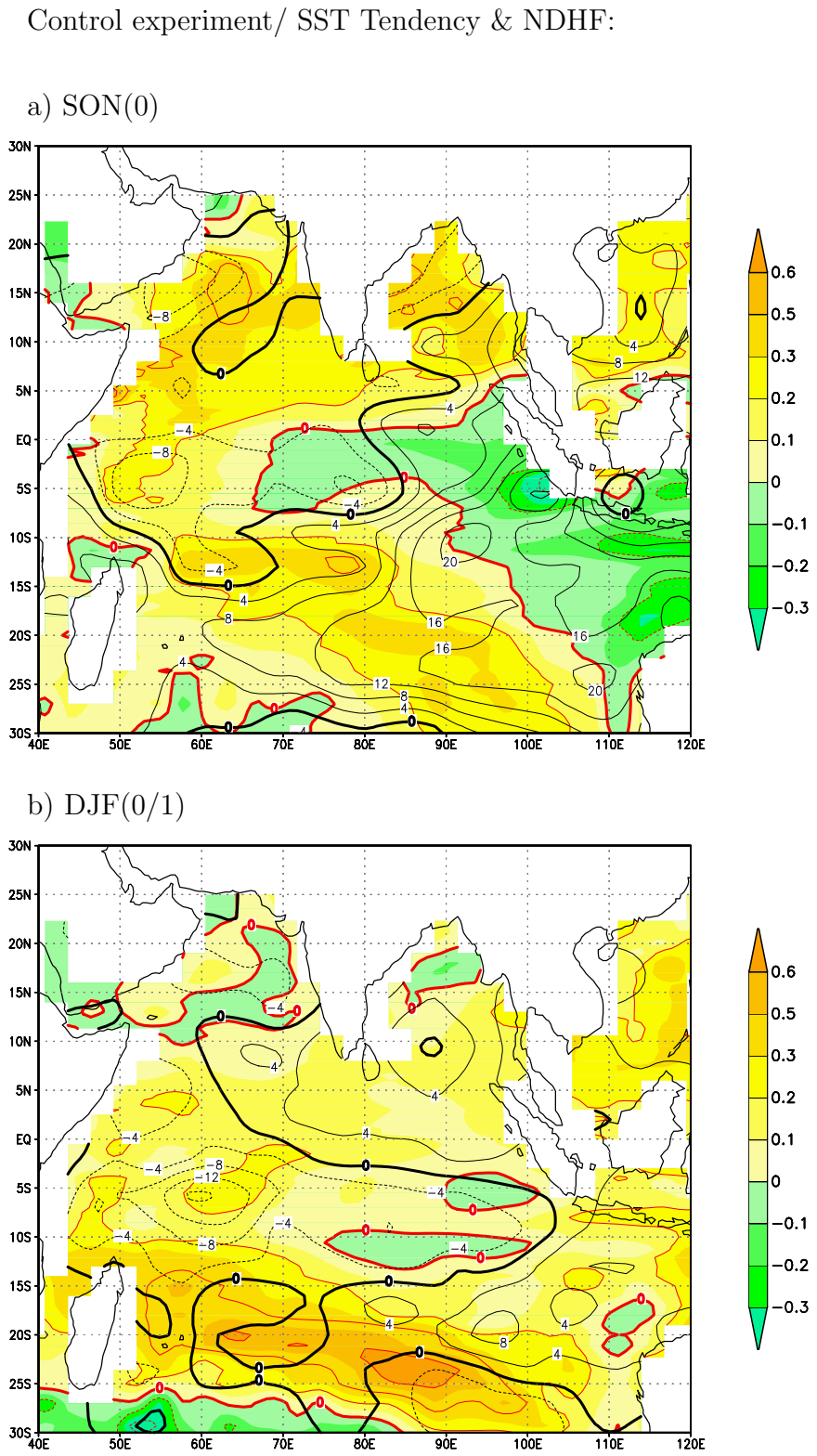

Figure 4.16: (top) Composite patterns of SST tendency anomalies (shaded and red contours in °C) and net downward heat flux (NDHF; black contours in Wm^{-2}) anomalies. For SST tendency contour interval is 0.2. For NDHF contour interval is 4. Anomalies are from the control experiment and seasonally averaged for SON. (bottom) As above, except that anomalies are for DJF(0/1).

Control experiment/ SST Tendency & NDHF:

c) MAM(1)

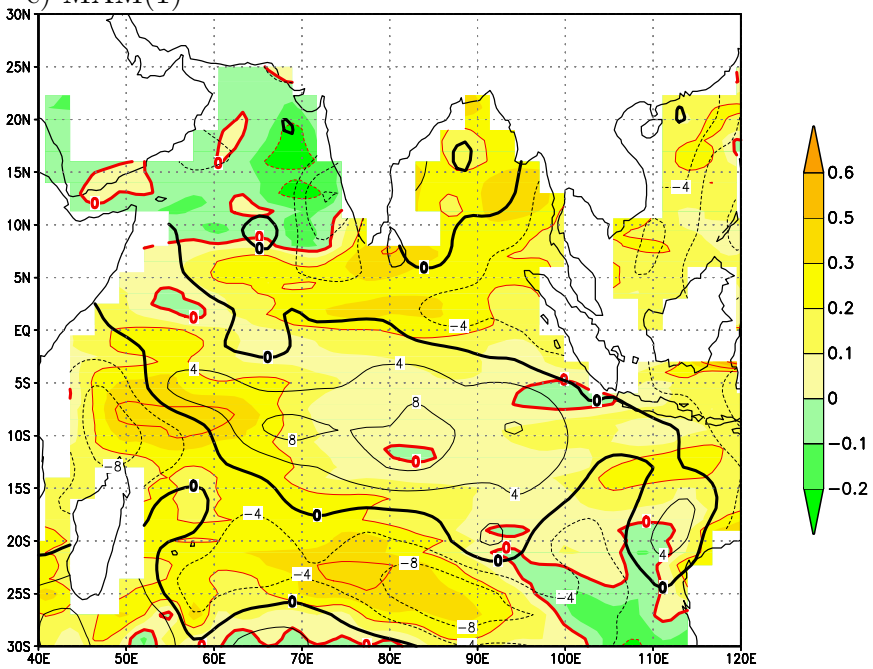

Figure 4.16: (continued) As in figure 4.16 a, except that anomalies are for MAM(1).

Non-ENSO experiment/ SST Tendency & NDHF:

a) SON(0)

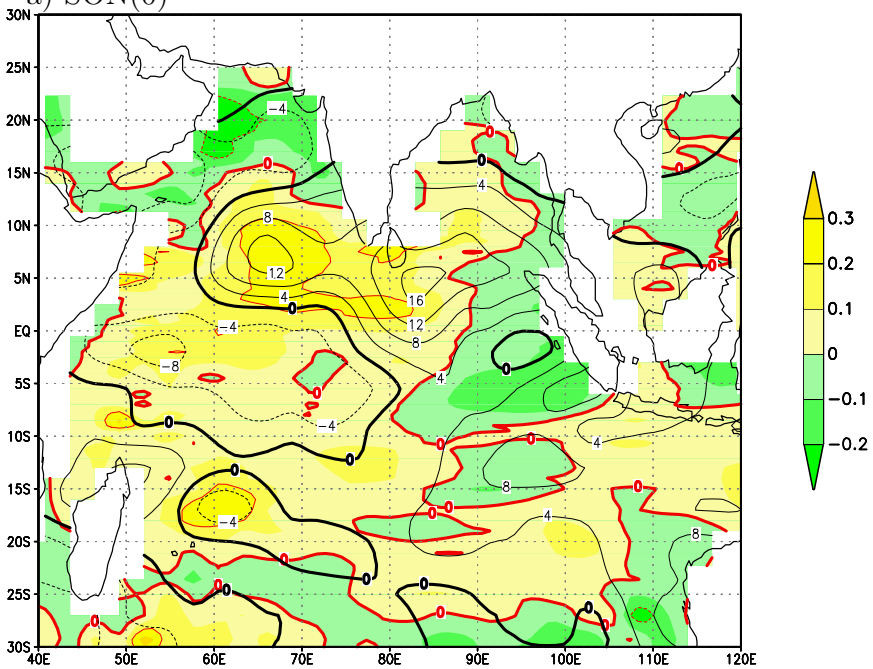

Figure 4.17: Composite patterns of SST tendency anomalies (shaded and red contours) and net downward heat flux (NDHF; black contours) anomalies. For SST tendency contour interval is 0.2. For NDHF contour interval is 4. Anomalies are from the non-ENSO experiment and seasonally averaged for SON.

Non-ENSO experiment/ SST Tendency & NDHF:

b) DJF(0/1)

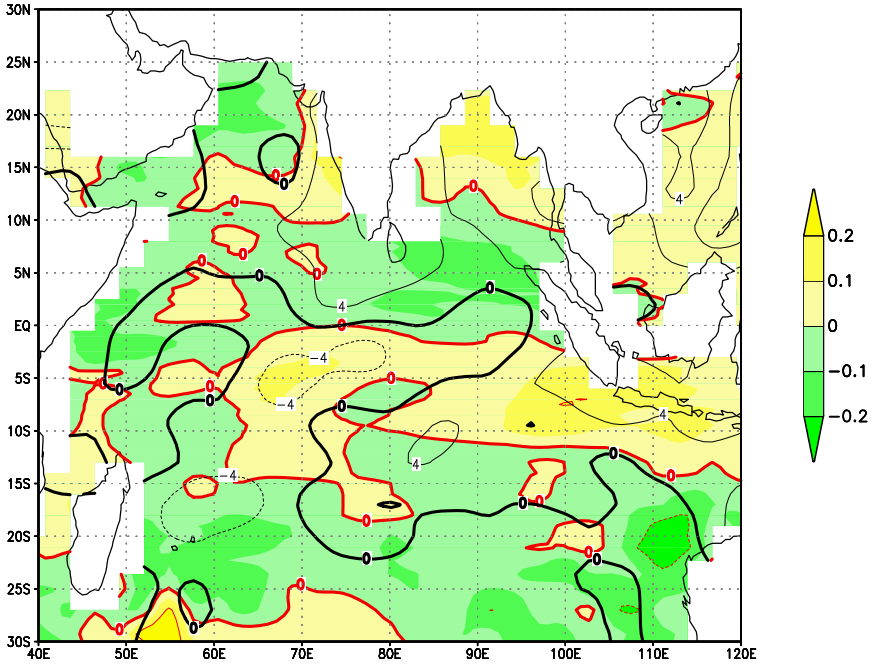

c) MAM(1)

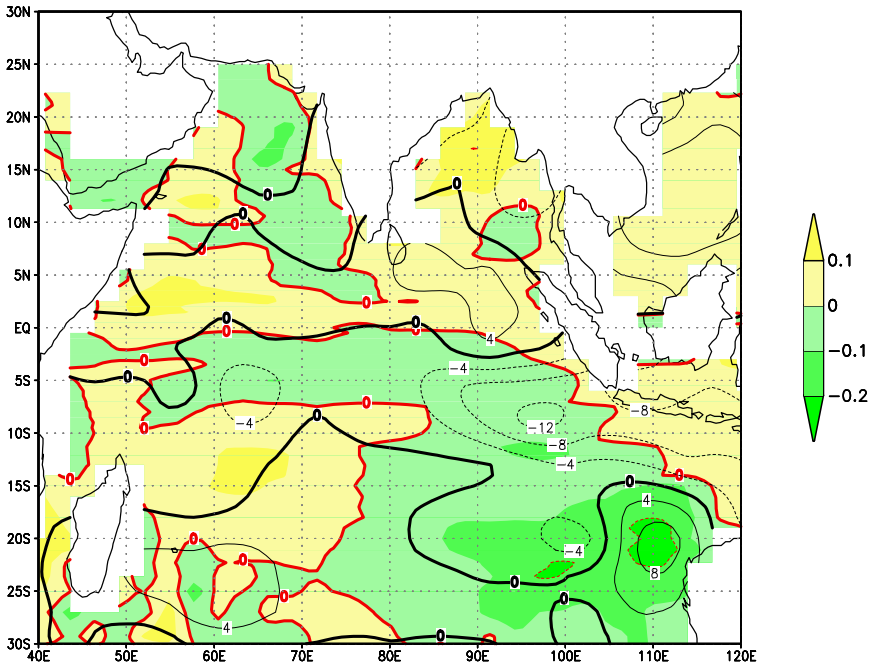

Figure 4.17: (continued) (top) As in figure 4.17 a, except that anomalies are for DJF(0/1). (bottom) As in figure 4.17 a, except that anomalies are for MAM(1).

Control experiment/ z20 & WSC/ MAM(1):

Regression based on Soce-Dec

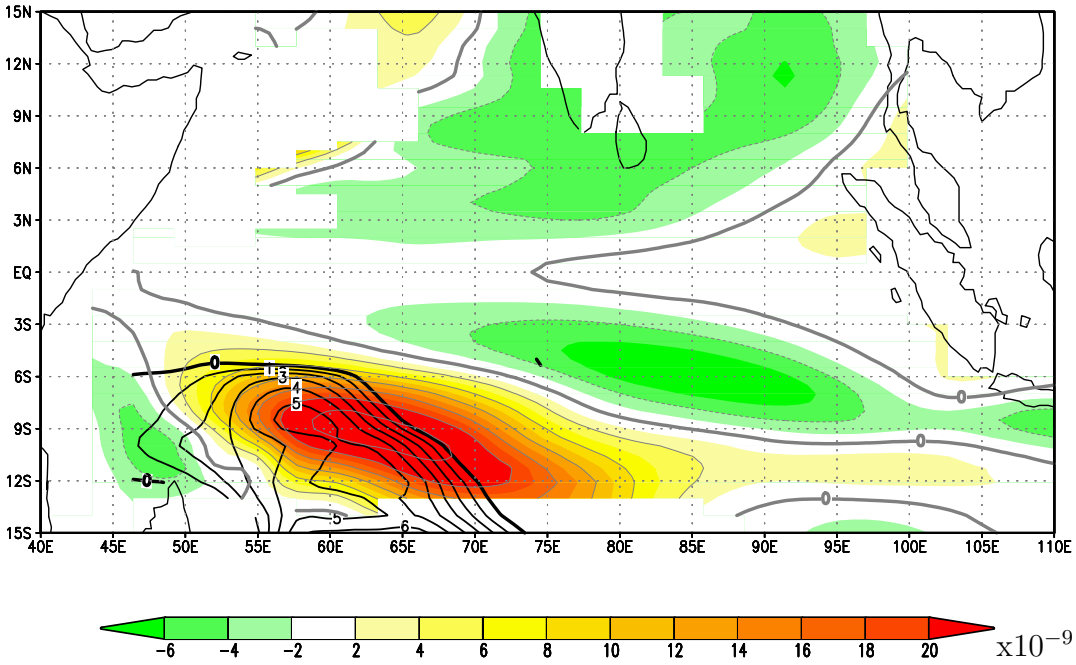

Figure 4.18: Regression coefficient of z20 (shaded and red contours) and wind stress curl (WSC; black contours) anomalies with respect to the Soce-Dec index. For z20 contour interval is 2. For WSC contour interval is 0.2. Anomalies are from the control experiment and seasonally averaged for MAM.

4.7 Summary and Conclusions

In this chapter, the interannual variability in the tropical Indian Ocean as simulated by two experiments with the CGCM ECHO-G model was analyzed, focusing in particular on interannual Rossby waves and related variability. Before analyzing the simulated interannual variability, the ability of the model to reproduce the annual mean and the interannual variance in the tropical Indian Ocean was assessed. In general, the annual mean and the interannual variance of SST, z20 and wind stress in the model are reasonably close to the reference dataset. The model, however, does not completely capture the zone off Indonesia with its strong coastal upwelling and the upwelling zone in the western tropical South Indian Ocean (SIO) is confined 10° more to the west than in the observations.

The variability related to SIO Rossby waves has been identified in the two experiments and its evolution has been described by means of a POP analysis of HC anomalies and by means of a HC index. This index, the Soce index, which is based on the POP analysis, is consistent with a thermocline depth (z20) index proposed in XASM. In particular, the December values of the Soce index (Soce-Dec) were used to perform cross-correlation and regression analyses with some oceanic and atmospheric fields to follow the time evolution of variability related to the SIO Rossby waves.

In general, the simulated start and decay of the SIO Rossby waves follow the timing of those presented in XASM. However, the copropagation of anomalies of some fields with the SIO Rossby waves and the related thermocline feedbacks develop in a different way in the control experiment and do not take place in the non-ENSO experiment. With regard to the *positive* feedback, no evidence of an overall copropagation of WSC anomalies leading to a *positive* thermocline feedback was found for the two experiments. For the control experiment, the WSC cross-correlation map shows a standing structure. For the non-ENSO experiment, there is no covariability at all of SST and WSC anomalies with the SIO wave.

With regard to the *negative* feedback, copropagation leading to a *negative* thermocline feedback is only indicated for the control experiment only. For this experiment, in the region at 10°S and west of 60°E, a region where the model exhibits open-ocean upwelling and a shallow thermocline, some copropagation of SST appears in May(1) and continues until Sep(1). This copropagation of SST with HC anomalies coincides with a weak copropagation of negative WSC anomalies and positive precipitation anomalies, which appears to be indicative of the *negative* thermocline feedback found by XASM. The inabilility of the model to simulate the copropagation realistically is likely due to a too deep annual mean thermocline.

The present study shows that the forcing mechanism for the Rossby waves in the SIO is related to positive SLP anomalies in the southeastern part of the tropical Indian Ocean. The associated atmospheric circulation anomalies are southeasterlies south of the equator and equatorial easterlies. These anomalous winds can produce negative SST anomalies in the eastern Indian Ocean through equatorial and coastal upwelling and westward propagating Rossby waves that deepen the thermocline. This study also shows that ENSO produces conditions favorable for the development of Rossby waves in the

SIO, since ENSO induces positive SLP anomalies in the southeastern part of the tropical Indian Ocean.

In presence of interannual variability in the Pacific, an atmospheric connection through the wind field exists. This connection links the variability at both sides of the equator in the Indian Ocean region. The link is the Southern Oscillation, which is characterized by positive SLP anomalies located east of 60°E and in the whole band of latitudes from 30°S to 25°N. These positive SLP anomalies generate winds, which contribute to positive NDHF anomalies in some regions and provide wind forcing on each side of the equator. This forcing is an important determinant of the covariability of equatorial western HC with off-equatorial HC variability. In other words, the spatial distribution of the SLP anomalies in the Southern Oscillation determines the coexistence of SIO Rossby waves with positive HC anomalies north of and over the equator, which contributes to the basin wide SST warming that the Indian ocean undergoes during an El Niño event. On the other hand, in absence of interannual variability in the Pacific, no evidence of a similar link was found.

ENSO is found to be the dominant forcing for the Indian Ocean HC variability and its signature in the Indian ocean includes both a dynamical and a thermodynamical response. Depending on the season and location it is possible to have warming either due to positive NDHF, oceanic processes, such as downwelling Rossby waves in the SIO, or due to a combination of both positive NDHF and oceanic processes. Additionally, the interannual variability in the Indian Ocean is only consistent with a cycle if ENSO is included in the simulations.

Even though a standing structure is dominant in the WSC crosscorrelations for the control experiment, in MAM(1) there are favorable conditions for a *positive* thermocline feedback: positive SST and thermocline depth anomalies are colocated with WSC anomalies that produce an anticyclonic circulation that contributes to increase the positive thermocline depth anomalies. For the non-ENSO experiment, since there is no covariability of SST with the SIO wave, no interaction can be produced. This has implications for the role of ENSO on the predictability of western SIO climate variability. The results here suggest that potential predictability for spring SST in the western SIO associated with SIO Rossby wave activity is provided by ENSO only. This issue needs further research and models that simulate an annual mean thermocline realistically are necessary to improve our understanding about the Indian Ocean predictability.

Finally, this study suggests that ENSO forces Rossby waves in the South Indian Ocean and, in general, has an influence on the HC variability in the tropical Indian Ocean at two different interannual timescales. Together with several recent studies (Reason et al. 2000; Allan et al. 2001), the present study highlights the fact that a better understanding of the interannual variability in the Indian Ocean can be achieved by investigating the impacts of ENSO on the whole Indo-Pacific region and by discriminating the effects of the two dominant interannual timescales of ENSO.

Chapter 5

Wind-Driven Oceanic Rossby Waves in the Tropical South Indian Ocean on Interannual Timescales: A Simple Stochastic Model

5.1 Introduction

Several observational, modeling and theoretical studies have shown that the large-scale variability of the thermocline is dominated by its low-frequency component and that the wind-driven circulation plays an important role in producing this variability. Sturges and Hong (1995) analyzed the Bermuda tide gauge record and showed that sea level variability at decadal timescales is consistent with an oceanic response, in form of baroclinic Rossby waves, to wind stress forcing across the Atlantic. Experiments with coupled general circulation models (CGCM) also suggest that the decadal variability of the midlatitude thermocline in the North Pacific is largely wind driven (e.g. Latif and Barnett 1994). Frankignoul et al. (1997, hereafter FMZ) suggested by using a simple stochastic model that Atlantic decadal variability primarily reflects the thermocline response to the stochastic atmospheric forcing. Sirven et al. (2002, hereafter SFCT) extended the FMZ model and investigated the Rossby wave response to stochastic wind stress forcing in the midlatitudes with emphasis on the impact of horizontal mixing and zonal variations of the forcing.

Studies based on upper-ocean temperatures and satellite altimetric data have detected baroclinic Rossby waves in low latitudes. In the tropical South Indian Ocean (SIO), westward propagating thermocline-depth anomalies have been detected at interannual timescales and attributed to oceanic Rossby waves (Perigaud and Delecluse 1993; Masumoto and Meyers 1998; Chambers et al. 1999; Birol and Morrow 2001).

In a study with oceanic and atmospheric data from reanalysis products, Xie et al. (2002) showed that there is an open-ocean upwelling zone in the tropical western South Indian Ocean, and that in this upwelling zone there is a strong influence of thermocline movements on sea surface temperature (SST). The thermocline effect on SST in the western tropical SIO is made possible by the presence of both upwelling and a shallow thermocline in this region. Additionally, the authors found that ENSO and processes off Sumatra, Indonesia, are the dominant forcings for the SIO thermocline variability through the forcing of Rossby waves, which propagate westward and interact with the atmosphere. The interaction consists of a switch from a *positive* thermocline feedback to a *negative* thermocline feedback. Both feedbacks include the propagation of SST and wind stress curl (WSC) anomalies with the positive thermocline depth anomalies produced by the Rossby wave. For the *positive* (*negative)* feedback, the WSC anomalies reinforce (dissipate) the thermocline depth anomalies. Thus, through the effect of the SIO Rossby waves on SST, the waves offer potential predictability for SST and tropical cyclones in the western SIO in the boreal winter and spring seasons.

Studies of the large-scale variability of the thermocline forced by stochastic wind stress have been concentrated on decadal to interdecadal variability in the midlatitudes (Frankignoul et al. 1997; Jin 1997; Sura et al. 2000; Sirven et al. 2002). In the present chapter, the stochastic model by SFCT is used to test if the interannual variability of sea surface height (SSH) related to Rossby waves in the tropical SIO can be explained by the passive response of the ocean to stochastic wind stress forcing, i.e. the day-to-day changes in wind stress forcing that are associated with random weather fluctuations. The concept of the stochastic climate model was first proposed by Hasselmann (1976) and is based on the Brownian motion analogue. According to this picture, the observed red spectrum of oceanic fluctuations is the response to stochastic atmospheric variability. Stochastic climate models have been widely applied in literature. The stochastic climate model concept has been used for the study of e.g. the decadal variability of the thermohaline circula-

tion, upper tropospheric dynamics, interannual variability of open ocean deep convection and glacial climate variability. The reader is referred to the review paper by Frankignoul (1995) to obtain more details about the stochastic climate model. It is used in the present chapter in the form of the SFCT model to study the thermocline variability at interannual timescales due to wind stress forcing.

The major conclusion in this chapter is that the SFCT model's spectral predictions of the baroclinic response to temporally white wind stress curl forcing are consistent with the sea level observational data at Cocos Island (12°S, 96.5°E) and with an experiment using a CGCM in which ENSO was suppressed. In particular, the shape and level of power of the frequency spectra of model SSH at various longitudes at 10°S are well predicted by the SFCT model. Furthermore, the predictions for sea level at Cocos Island correspond well to the observations. This suggests that a stochastic climate model is an appropriate starting point for understanding interannual changes in the tropical South Indian Ocean that are independent of the interannual variability in the Pacific.

The chapter is arranged as follows: Section 5.2 introduces the SFCT stochastic model. Section 5.3 introduces the two experiments with the CGCM ECHO-G (Legutke and Voss 1999) and presents the comparison between the theoretical predictions by the SFCT model and the interannual sea surface height variability in both experiments. Section 5.4 shows the comparison of the theoretical predictions with sea level observations at Cocos Island. The transmission of energy from the tropical Pacific to the southern Indian Ocean through coastal Kelvin waves along the western coast of Australia is examined in section 5.5. Conclusions are given in section 5.6. The work presented in this chapter has been accepted for publication in the Journal of Physical Oceanography.

5.2 The stochastic model

Since SFCT's (2002) stochastic model is essential in the present study, a brief description is presented in the following. The model consists of a time-dependent geostrophic 2.5-layer ideal-fluid model of the ventilated thermocline. The effect of the mean flow is taken into account. At the eastern boundary a no-normal flow condition is imposed and at the western boundary a no-radiation condition. The only forcing is the surface wind stress transmitted to the ocean by Ekman pumping. Western boundary dynamics are excluded;

therefore the model only applies east of the western boundary current region. A downward Ekman pumping w_e is imposed at the surface of a subtropical gyre limited to vanish at $y = y_N$ and $y = y_S$. The lightest layer of density ρ_1 and thickness h_1 is located south of the latitude y_1 ($y_S < y_1 < y_N$), where the second layer of density ρ_2 and thickness h_2 outcrops. The depth $H = h_1 + h_2$ represents the base of the thermocline. The abyss is a third layer at rest, with a density ρ_3 and an infinite depth. The last characteristic is consistent with the rigid lid condition imposed at the surface. The β plane approximation, which assumes that the Coriolis parameter varies linearly with latitude, is used. The zonal coordinate is denoted by x and the eastern and western boundaries are at x= 0 and x=$\mathrm{x}_w < 0$. For the present study, the eastern boundary is located at 110°E. The geostrophic zonal flow vanishes at the eastern boundary ($h_1 = 0$ and $H = h_2 = H_0 = 200m$ at x= 0), while a no-radiation condition is used at the western boundary. The effective depth is given by

$$\mathcal{H} = \sqrt{\frac{\gamma_1}{\gamma_2}\, h_1^2 \,+\, H^2}, \tag{5.1}$$

where $\gamma_1 = (\rho_2 - \rho_1)g/\rho_0$ and $\gamma_2 = (\rho_3 - \rho_2)g/\rho_0$ represent the reduced gravities associated with each layer and both are much smaller than gravity g. ρ_0 is a reference density. $\mathcal{H}$ characterizes the overall response of the thermocline to a variation in w_e, including the effect of the mean flow. The evolution equation for the effective depth $\mathcal{H}$ is given by:

$$\frac{\partial \mathcal{H}}{\partial \mathrm{t}} - c_1 \frac{\partial \mathcal{H}}{\partial \mathrm{x}} = \lambda w_e, \tag{5.2}$$

where λ is a constant ($\simeq 1$), $c_1 = \beta\gamma_2\lambda\mathcal{H}/f^2$ and f the Coriolis parameter.

In particular, the linearized version of Eq. (5.2) with dissipation in the long-wave approximation is used, which takes into account the influence of horizontal mixing and describes the free waves of the first baroclinic mode as:

$$\frac{\partial \mathcal{H}'}{\partial \mathrm{t}} - c_b \frac{\partial \mathcal{H}'}{\partial \mathrm{x}} = -\frac{c_b}{x_e}\mathcal{H}' + \text{wind stress forcing} \tag{5.3}$$

where $\mathcal{H}'$ represents the fluctuations of the equivalent depth around its mean and characterizes the overall response of the thermocline to a variation in the wind forcing, x is the zonal coordinate that measures the distance from the eastern boundary, c_b is the mean value of the Rossby wave phase speed at a given latitude and x_e defines an e-folding distance from the eastern boundary that represents the influence of horizontal mixing (Qiu et al. 1997). This e-folding distance is given by $\mathrm{x}_e \approx [5{c_b}^4 f^4/16\omega^4 A_h \beta^3]$, where w is the

frequency and A_h is the horizontal eddy viscosity. The x_e distance becomes infinite at low frequency and it vanishes at high frequency (SFCT), since it is defined through a bi-Laplacian dissipation.

Latitude enters Eq. (5.3) only as a parameter. Thus, the response can be calculated for every latitude separately with the appropriate values of f, β, c_b and A_h and by providing a functional form for the wind stress forcing term that gives the temporal and spatial dependence of the forcing. In the following, two general cases will be considered, zonally independent forcing (section 5.2.1) and zonally dependent forcing (section 5.2.2).

5.2.1 Zonally independent forcing

The wind stress forcing associated with the day-to-day weather fluctuations can be represented in Eq. (5.3) by the Ekman pumping fluctuations $\hat{F}(x, f, \omega) = \hat{F}(\omega) \exp[i\omega t]$. As a first order approximation, it is assumed that $\hat{F}$ is independent of the zonal coordinate x.

Additionally, the spectrum of the Ekman pumping forcing S_F is assumed to be temporally white: $S_F(\omega) = S_0$, where S_0 is a constant. Under these two conditions for the wind stress forcing the response spectrum S_R is given by

$$S_R(\omega, x) = \frac{S_0}{(\omega)^2 + \omega_d^2} \times \left[\left(1 - e^{x/x_e}\right)^2 + 4e^{x/x_e} \sin^2 \left(\frac{\omega x}{2\omega_d x_e} \right) \right], \tag{5.4}$$

where $\omega_d = c_b/x_e$.

Equation (5.4) resembles the response spectrum obtained by FMZ, although they did not take into account dissipation by zonal mixing as done in SFCT. A noteworthy fact is that the response is x-dependent even though the forcing is not.

At lower frequencies, the response spectrum flattens toward a constant level S_0

$$S_R(\omega \to 0, x) = S_0 \left(x/c_b\right)^2, \tag{5.5}$$

which increases *quadratically* with the distance from the eastern boundary. FMZ identified the baroclinic response as a red spectrum with a dominant period determined by the time for a long nondispersive baroclinic Rossby wave to cross the entire basin. This period increases with the basin width. The spectral decay at high frequencies [higher than $(10\,month)^{-1}$] is somewhat faster than w^{-2} because of the exponential term in Eq. (5.4), except for $x/x_e << -1$ when dissipation becomes dominant, in this case $S(x, w) = S_0/w^2$ (SFCT).

5.2.2 Zonally dependent forcing

In this case, the Ekman pumping forcing is represented by a superposition of harmonic components $\hat{F}(k,\ \omega)\exp[i(\omega t + kx)]$ and its corresponding wavenumber-frequency spectrum by $S_F(k,\omega) = S_F(k,0) = S_e(k)S_0$, that now depends on the zonal wavenumber k, but is still assumed to be temporally white. The response spectrum S_R under the above conditions for the wind forcing is

$$S_R(k,\ x,\ \omega) = \frac{S_e(k)S_0}{(\omega - kc_b)^2 + \omega_d^2} \times \left[\left(1 - e^{x/x_e}\right)^2 + 4e^{x/x_e}\sin^2\frac{(\omega - kc_b)x}{2c_b}\right] \tag{5.6}$$

Equation (5.6) indicates that there is a peak at the resonance frequency $\omega_r = k_0\, c_b$ of a free Rossby wave of wavenumber k_0. The speed of the Rossby waves along 10°S in the Indian Ocean is $c_b = 14\ cm\ s^{-1}$. The dominant synoptic spatial scale of atmospheric variability has a wavelength of between 4000 km to 5000 km (Holton 1992). For these values of c_b and wavelength the period is about 12 months. When Eq. (5.6) is integrated over a reduced finite number of wavenumbers around k_0, it may be possible to obtain a frequency spectrum that still has a small peak at frequency $\omega_r = k_0 c_b$. However, this resonance in a bounded ocean basin is only capable of producing a weak spectral peak in the response spectrum due to the fact that the basin boundary implicitly poses a damping effect to limit the resonance, which otherwise is unlimited for undamped Rossby waves in a globally periodic ocean. Furthermore, the weak resonant peak can be further flattened when ocean dynamic damping is acting. Thus, this weak frequency peak is potentially not sufficient to account for observed variability at the timescale related to it (Jin 1997).

If the wind stress can be considered as a continuum of zonal scales between $-k_M$ and k_M, the frequency spectrum can be computed by integrating Eq. (5.6) between these two wave numbers if an expression for $S_e(k)$ is provided.

Different expressions for $S_e(k)$ can be considered. Sirven et al. (2002) examined two kinds of spatial dependence: $S_e(k)$ is constant for a finite interval of k's or a k^{-2} dependence is assumed. Only the first case is reviewed here.

The first case consists of a wind stress curl spectrum with $S_e(k)$ being constant between $-k_M$ and k_M and equals zero outside this range:

$$S_F(k) = S_0 S_e(k) = \begin{cases} \frac{S_0}{2k_M} & \text{for k between } -k_M \text{ and } k_M \\ 0 & \text{otherwise} \end{cases} \tag{5.7}$$

At very low frequencies and for large zonal distances x (larger than 3000 km), the response spectrum is

$$S_R(x,\omega) \approx \frac{\pi S_0 |x|}{k_M {c_b}^2} \tag{5.8}$$

This implies that if the wind–stress curl spectrum is temporally white and constant for a finite interval of k's, the response frequency spectrum is white at low frequency and its level increases *linearly* with distance from the eastern boundary.

5.3 Comparison with a CGCM

The data from two experiments with the coupled ocean-atmosphere general circulation model ECHO-G are used: in one experiment, sea surface temperatures are set to climatological values in the tropical Pacific Ocean in order to suppress ENSO (non-ENSO experiment). In the other experiment, interactions are allowed everywhere (control experiment). The model performance and some details of the two experiments were already mentioned in chapter 2.

The monthly anomalies of model wind stress curl (WSC) and sea surface height (SSH) for 100 years are considered in the following analysis. For each variable, the monthly mean climatology is first calculated. Then, interannual anomalies are computed as the difference from this climatology. Additionally, the local linear trend was subtracted at each point. Heat content (HC) has been computed by integration of ocean temperatures from the surface to 206m depth. The spectra of both model data and observations are calculated using a Bartlett procedure with a Bartlett lag window.

5.3.1 Wind stress curl spectra

The frequency spectra of the WSC anomalies along 10°S at various distances in the Indian Ocean are shown for the two experiments in Fig. 5.1. The distances are measured with respect to the eastern boundary, which is located at longitude 110°E. The frequency spectra in the control experiment (Fig. 5.1a) have a peak of enhanced variability at the frequency of $(25\ month)^{-1}$, which corresponds well to the ENSO period in the ECHO-G model. This peak at interannual timescales in WSC is consistent with the idea of an oscillatory forcing of Rossby waves in the SIO due to Ekman pumping changes induced by ENSO.

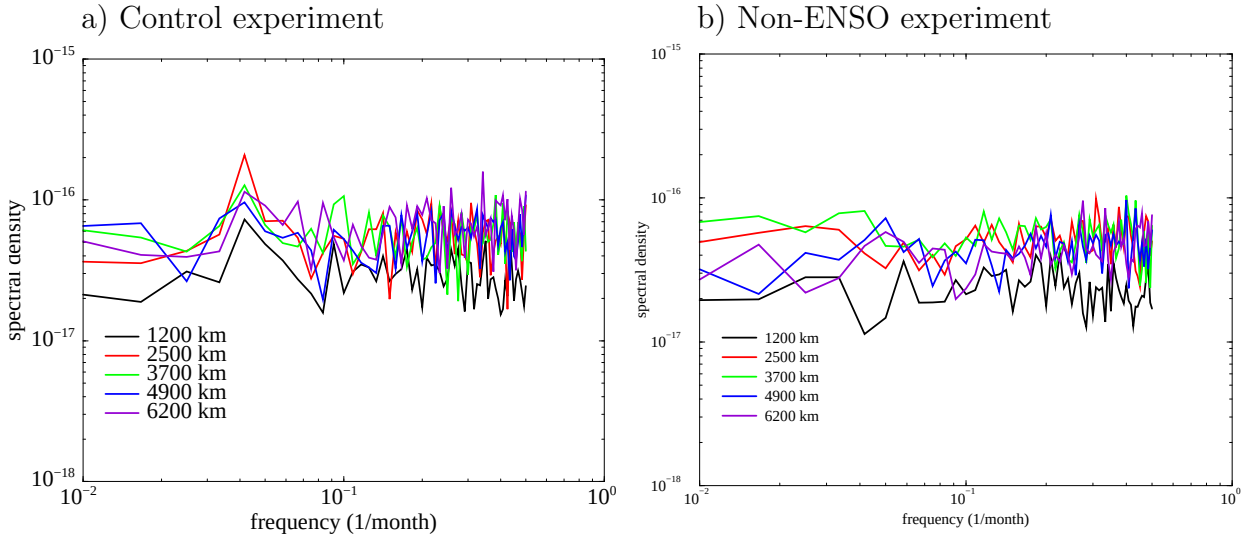

Figure 5.1: Frequency spectrum of surface wind stress curl at 10°S at various distances from the eastern boundary, which is located at 110°E. (a) For the control experiment and (b) for the non-ENSO experiment.

On the other hand, the frequency spectra in the non-ENSO experiment are essentially white (Fig. 5.1b). The white noise level tends to be a bit larger in the center of the basin, but the zonal changes are small. Thus, the forcing in the non-ENSO experiment can be considered as temporally white, such as it is assumed in the stochastic forcing theory shown in section 5.2. Therefore, focus is set on the non-ENSO experiment in the following. The propagating components (eastward, westward) of the zonal wavenumber spectrum of the WSC anomalies at 10°S in the non-ENSO experiment are shown in Fig. 5.2. The power is mainly concentrated at large scales, decaying as k^{-3} for wavelengths longer than 5500 km and as k^{-4} for shorter wavelengths. Since such a $S_e(k)$-dependence on k has not been examined before, it is necessary to derive an expression for this case. The following $S_e(k)$ dependence is proposed:

$$S_F = S_0 S_e(k) = \frac{3\sqrt{3}}{4\pi} So \frac{{k_M}^2}{{k_M}^3 + |k|^3} \tag{5.9}$$

S_F now depends on k as $|k|^{-3}$ and is still assumed to be temporally white. It is also symmetric, so that there is no privileged zonal direction.

The numerical integration of Eq. (5.6) over k with S_F defined as in Eq. 5.9 leads to a frequency spectrum, whose level increases *linearly* with the distance from the eastern boundary (not shown), in a similar way as in the case of zonally dependent forcing considered in section 5.2.1.

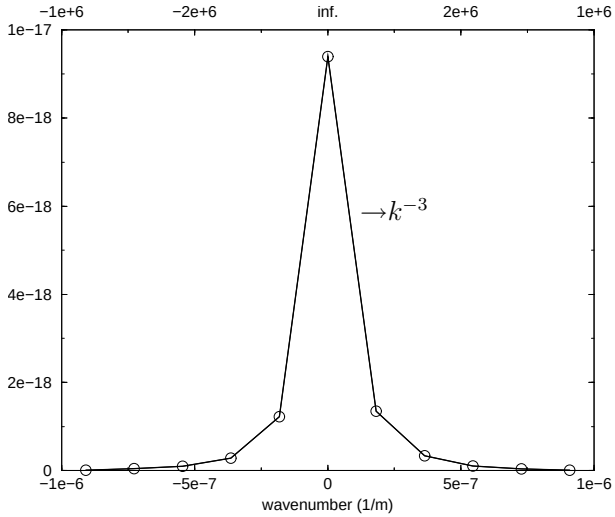

Figure 5.2: Wavenumber spectrum of surface wind stress curl at 10°S in the non-ENSO experiment [$Pa\ m^{-1}$]. Note that the upper x-axis label indicates longitude.

5.3.2 Comparison with the stochastic model predictions

In this section and in section 5.4, a quantitative comparison of the predictions for the response spectrum by the SFCT model against the spectra obtained from the non-ENSO experiment and from observations is performed. Such comparison requires the specification of the adjustable parameters that enter Eq. (5.6). The values chosen for the theoretical predictions in Figs. 5.3b and 5.4 are listed in Table 5.1. With these values, the SFCT model nicely reproduces the spectral level at high and low frequencies simulated in the non-ENSO experiment (Fig. 5.3). East of 60°E (at distances longer than ≈ 6200 km),

Table 5.1: Values for the theoretical predictions.

	Non-ENSO Experiment (10°S)	Cocos Island (12°S, 96°E)
Parameters	$f = 2.5 \times 10^{-5}\ s^{-1}$	$f = 3 \times 10^{-5}\ s^{-1}$
	$\beta = 2.25 \times 10^{-11}\ (m\ s)^{-1}$	$\beta = 2.2275 \times 10^{-11}\ (m\ s)^{-1}$
	$A_h = 2.5 \times 10^{3}\ m^2\ s^{-1}$	$A_h = 2.5 \times 10^{3}\ m^2\ s^{-1}$
Baroclinic mode	$c_b = 1.4 \times 10^{-1}\ m\ s^{-1}$	$c_b = 1.4 \times 10^{-1}\ m\ s^{-1}$
Forcing	$S_0 = 7.5 \times 10^{-19}\ m^2\ s^{-2}$	$S_0 = 9.75 \times 10^{-19}\ m^2\ s^{-2}$
	$(cycles\ per\ month)^{-1}$	$(cycles\ per\ month)^{-1}$

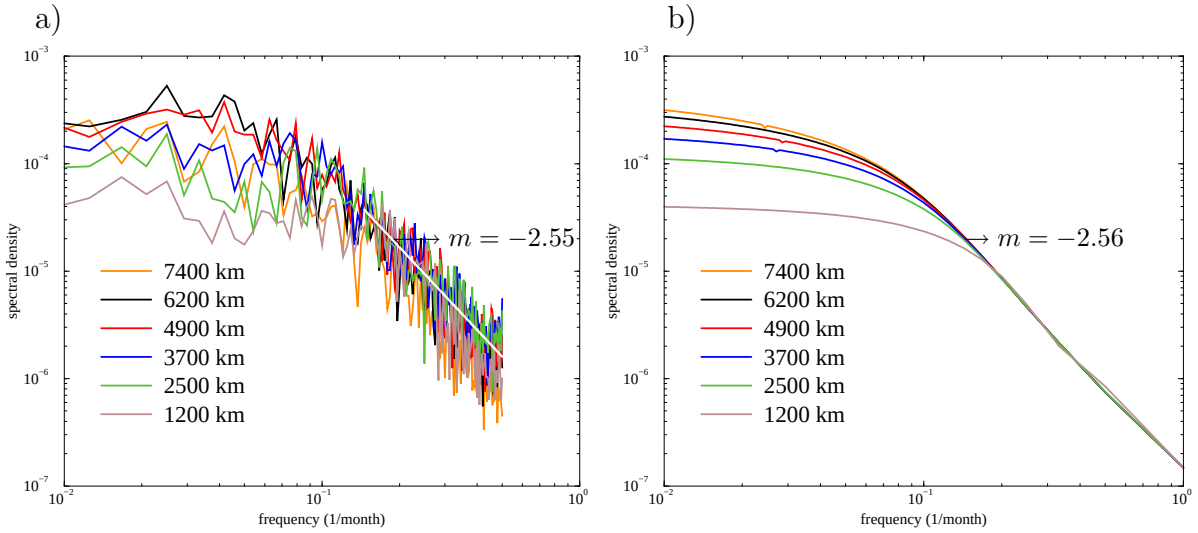

Figure 5.3: Frequency spectrum of the sea surface height at 10°S for various distances from the eastern boundary, which is located at 110°E. (a) for the non-ENSO experiment and (b) as predicted by the stochastic model. The white straight line in (a) corresponds to the amplitude average at high frequencies, which was calculated based on the spectra for the distances going from 1200 km to 6200 km and whose slope is indicated with an arrow. The slope for the predicted spectra is also indicated.

the frequency spectra of the monthly fluctuations of sea surface height (SSH) at 10°S in the non-ENSO experiment have a shape consistent with the stochastic model predictions. As shown in Figs. 5.3a and 5.3b, the power flattens at low frequencies (at periods longer than 10 months) at a level that increases with the distance from the eastern boundary. Figures 5.3a and 5.3b also show that the power decreases as $\approx w^{-2.6}$ at high frequencies, with a level that does not depend on the distance x to the eastern boundary (i.e. not dependent on the longitude). West of 60°E, the mean ocean currents are generally stronger than the currents in the open ocean regions, so that a theory for an ocean with mean zonal flow is less likely to apply.

The x-dependence of the oceanic response spectrum at low frequencies is between linear and quadratic. To document more precisely the zonal changes, Fig. 5.4 shows the SSH-power in four frequency bands centered around 1/180, 1/60, 1/32, 1/20 $month^{-1}$ as a function of longitude. The power dependence on longitude is compared in Fig. 5.4 to a parabola [Eq. (5.5), i.e. spatially and temporally white] and a straight line [Eq. (5.8) , i.e. temporally white and spatially constant for a finite interval of wavenumbers]. The straight line is obtained from a least square fit of all the points on Fig. 5.4. The typical wavelength of synoptic disturbances in the atmosphere is about 4000 km, then

$2\pi/k_M = 4000\,km$. Since S_0/c_b^2 should be the same for the straight line and the parabola and that the value of $2\pi/k_M$ is know, the parabola can be obtained substituting these values in Eq. (5.5).

Figure 5.4 shows that at periods around 20 months the level of the response frequency spectrum increases almost linearly. This illustrates that a better agreement with the non-ENSO experiment data at short periods is obtained when the spatial dependence of the forcing in Eq. (5.6) is taken into account, i.e. when zonally independent forcing is replaced by zonally dependent forcing. A similar improvement is obtained by SFCT in their study about the midlatitude variability in the North Atlantic Ocean. Figure 5.4 also shows that at lower frequencies the longitude dependence is between linear and quadratic, becoming closer to quadratic at the longest periods.

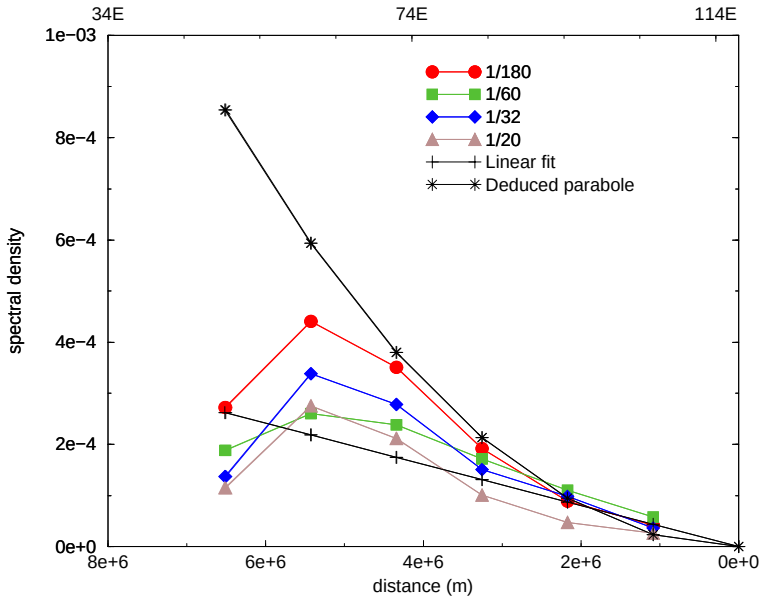

Figure 5.4: Spectral power of sea surface height anomalies at 10°S in four frequency bands centered about 1/20, 1/32, 1/60, and 1/180 $month^{-1}$ as a function of the distance from the eastern boundary, which is located at 110°E. Sea surface height anomalies are from the non-ENSO experiment. The straight line is obtained from a best linear fit and the parabola is deduced from the straight line as indicated in the text. Note that the upper x-axis label indicates longitude.

5.3.3 Discussion

The analyses presented in sections 5.3.1 and 5.3.2 suggest that a major part of the interannual variability in the tropical South Indian Ocean sea surface height (SSH) in the non-ENSO experiment is directly forced by the wind stress curl via Ekman pumping. Since the wind stress curl spectrum is essentially white at low frequencies, the atmospheric forcing can be considered as stochastic. The SFCT model predicts the shape, the level and the geographical variability of the SSH spectra resulting from the the combination of local Ekman pumping and Rossby wave propagation from the eastern boundary quite well. However, the predictions do not hold in the region west of 6200 km ($\approx 60°$E; Fig. 5.3a) where the mean current speed becomes rather strong.

In the POP analysis of the tropical Indian Ocean interannual variability shown in chapter 4, two distinct quasi-oscillatory (Q-O) modes of oceanic heat content variability with dominant periods of about 30 and 16 months were identified in the control experiment (Fig. 4.3). The 16-month Q-O mode was found in both the control and non-ENSO experiments (Figs. 4.3 and 4.4), while the 30-month Q-O mode was only found in the control experiment. The more energetic 30-month Q-O mode can be identified as the ENSO response of the Indian Ocean. The less energetic 16-month Q-O mode can be considered as ENSO-independent since it appears in both experiments. The 16-month Q-O mode in the non-ENSO experiment was seen in the thermocline but was not found in the atmosphere (Fig. 5.1b), thereby reflecting either a passive oceanic response or weak coupling in the Indian Ocean variability. The question of what determines the dominant timescale of the less energetic ENSO independent Q-O mode was considered. The analysis suggests that the dominat timescale is given by the time a long Rossby wave requires to propagate across the effective width of the basin. Thus, the mode can be considered as a fetch-limited baroclinic mode response. Like the 30-month Q-O mode, the 16-month Q-O mode in its imaginary part phase has similar spatial scales and is related to negative SST anomalies and to anomalous equatorial easterlies in the equatorial eastern Indian Ocean and anomalous southeasterlies in the southeastern Indian Ocean. These anomalous wind stresses are the major forcing for the tropical SIO Rossby waves (Xie et al. 2002).

The close relationship between negative SST anomalies in the equatorial eastern Indian Ocean and anomalous easterly winds together with positive equatorial SST anomalies in the west lead Saji et al. (1999) and Webster et al. (1999) to hypothesize that these anomalies are part of a temporally oscillatory coupled dipole mode that involves some positive air-sea feedback, is independent of ENSO and acting at interannual timescales. In the present study, no evidence of a statistically significant ENSO-independent interannual peak in the wind stress curl spectra (Fig. 5.1b) and in equatorial wind stress (not shown) could be found when using spectral analysis. Thus, the feedback implied in the equatorial SST dipole must be very weak, and the 16-month Q-O mode should not be significantly more energetic in the ocean interior than expected from the stochastic forcing approach presented here. It remains to be shown what fraction of the observed oceanic variability can be explained by stochastic forcing.

5.4 Comparison with observed data

The data used are the daily wind stress from the European Centre for Medium-Range Weather Forecast reanalysis for the period 1979-1993 (Gibson et al. 1999, ERA-15) and the daily sea level at Cocos Island located in the southeastern Indian Ocean for the period 1986-2002 supplied by the National Tidal Facility, The Flinders University of South Australia (UHSLC 2003). For both the wind stress and sea level fields, the first two harmonics of the annual cycle are calculated and the interannual anomalies are computed as the difference from those. For both fields the local linear trend was subtracted from the anomalies and then monthly means were calculated for the wind stress anomalies.

5.4.1 Wind stress spectra

The frequency spectra of ERA-15 zonal wind stress (Taux) at two locations along 0.5°S are shown in Fig. 5.5a. One location is in the Pacific at 100°W and the other one is in the Indian Ocean at longitude 100°E. Both spectra have a peak of enhanced variability at the frequency $(60\ month)^{-1}$, which corresponds to a main ENSO period reported by many authors (e.g. Latif et al. 2001). This peak in both spectra reveals that, associated with ENSO, there is an oscillatory behaviour in Taux not only in the eastern Pacific but also in the eastern Indian Ocean. This results from the Southern Oscillation, the

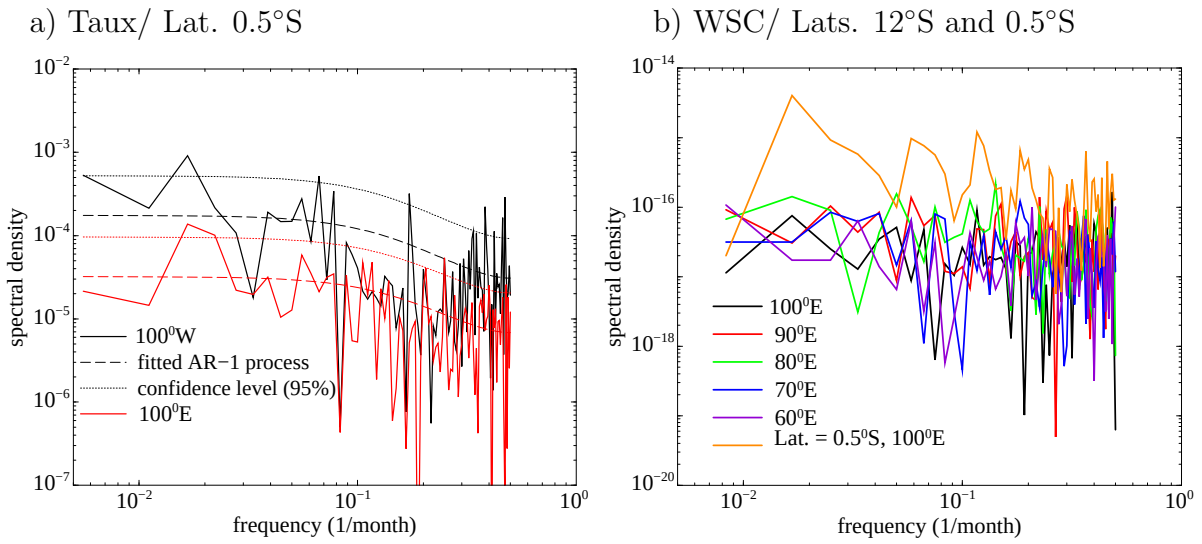

Figure 5.5: (a) Frequency spectrum of zonal wind stress (Taux) along 0.5°S at longitudes 100°E and 100°W. (b) Frequency spectra of wind stress curl (WSC) at 0.5°S, 100°E and, along 12°S at various longitudes. Wind stress anomalies are from the ERA-15 reanalysis.

atmospheric component of ENSO, which drives anomalies over the entire Indo-Pacific region. The spectrum at 100°W also shows an interannual peak at frequencies around $(16\ month)^{-1}$. This peak could be part of the biennial component of ENSO variability found by Rasmusson et al. (1990). However, the period is rather short.

Figure 5.5b shows the frequency spectra of WSC anomalies at 0.5°S and 100°E and along 12°S at various longitudes. The focus is put on WSC anomalies at 12°S, since comparisons with the sea level at Cocos Island will be presented below. Associated with the ENSO-related Taux peak at 100°E (Fig. 5.5a) there is a peak in the WSC at the same location at the frequency $(60\ month)^{-1}$ (orange curve in Fig. 5.5b). This is consistent with an ENSO related oscillatory forcing of Rossby waves in the SIO through anomalous wind stress in the equatorial and near-equatorial Indian Ocean region as seen in chapter 4.

The ENSO related wind stress anomalies extend over a band of latitudes in the Indian Ocean. In the control experiment described before, for instance, the highest correlations of zonal and meridional wind stress anomalies with the Niño3 index are found between 5°N and 10°S (not shown). The frequency spectra for WSC anomalies along 12°S are essentially white (Fig. 5.5b) and the average white noise level is approximately 10 times smaller than the average level for WSC anomalies at 0.5°S and 100°E. Since the WSC along 12°S is white the basic condition of the SFCZ model is satisfied.

The average white noise level at 10°S in the ERA-15 dataset is about 1.3 times the level ocurring in the non-ENSO experiment (Fig. 5.1b). Correspondingly, S_0 should be 1.3 times larger and the oceanic response should also be larger than in the non-ENSO experiment. Thus, for 12°S an estimate of S_0 is $9.75 \times 10^{-19}\, m^2\, s^{-2}\, (cycles\, per\, month)^{-1}$.

5.4.2 Sea level at Cocos Island

For the tropical SIO, only few oceanic time series long enough to estimate power spectra at interannual frequencies are available. However, the 17 years of observations at Cocos Island (12°S, 96.5°E) allow a quantitative comparison to the theoretical predictions of the stochastic model for the baroclinic response. Given the location of Cocos Island, the stochastic model should hold. The corresponding fetch for Cocos Island is x=1525 km. Since the WSC power for the observations is larger than in the non-ENSO experiment, the power spectrum for the sea level at Cocos Island is expected to have a larger energy level than that corresponding to the same fetch in the non-ENSO experiment.

Figure 5.6 shows that the sea level frequency spectrum is red and decays approximately

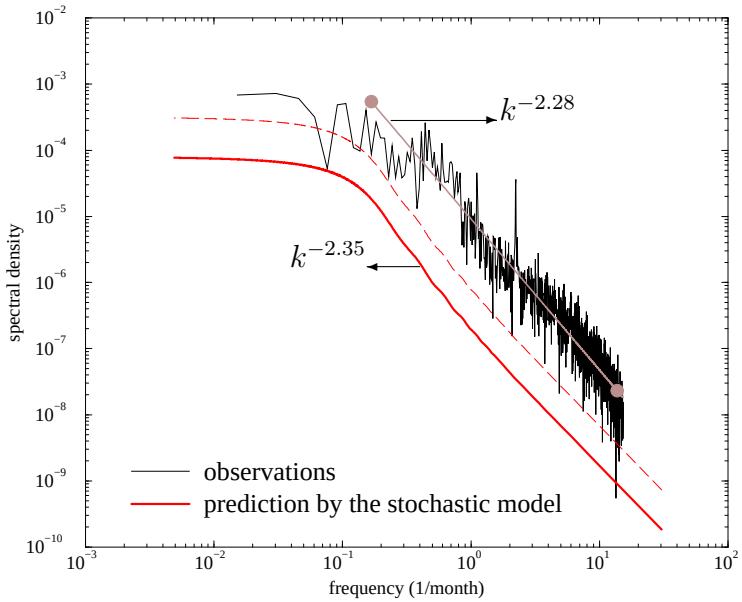

Figure 5.6: Frequency spectrum of sea level at Cocos Island. Solid black line: spectrum of the sea level data for Cocos Island supplied by the National Tidal Facility, The Flinders University of South Australia. Solid red line: prediction with the SFCT model with the parameter values listed in Table 5.1. Dashed red line: prediction with the SFCT model when S_0 is multiplied by a factor of 4. Solid brown line: best linear fit of the spectrum of sea level at Cocos Island at high frequencies

as $w^{-2.28}$ at periods less than 5 months. The prediction [integration of Eq. (5.6) with S_F such as in Eq. (5.9)] calculated with the values from Table 1 matches well the slope at high frequencies and the observed energy level at interannual timescales.

In a study about the low frequency temperature fluctuations off Bermuda, Frankignoul (1981) found that excess energy at high frequency was likely due to data noise and eddy contamination. I speculate that the excess energy in the Cocos Island observations at high frequency could be also due to eddy contamination. The good agreement of the slope suggests that the flattening at low frequencies is due to the limited distance to the eastern boundary.

In summary, the stochastic model suggests that the interannual variability at Cocos Island is to a large extent caused by stochastic wind stress forcing. It remains to be determined, however, whether the underestimation of the observed spectra can be attributed to poor parameter choices.

5.5 Energy propagation from the equatorial Pacific to the Southern Indian Ocean

Potemra (2001) showed in a study with a reduced gravity model that Rossby waves generated in the equatorial Pacific by anomalous wind stress curl, upon reaching the western boundary of the Pacific, create poleward propagating coastal Kelvin waves along the western coast of Australia, which in their turn generate offshore Rossby waves that can propagate into the interior Indian Ocean. The frequencies of the WSC forcing that allow the generation of offshore Rossby waves in the Indian Ocean are of order of several months to a year. Potemra (2001) also showed that, at interannual timescales, Rossby waves in the Pacific such as those generated during ENSO extrems mostly get reflected at the western boundary.

In this section, attention is paid to the HC variability in the southern part of the tropical Indian Ocean, with focus on the western coast of Australia. The objective is to examine if the transmission of energy from the tropical Pacific to the Indian Ocean as proposed by Potemra (2001) works in the model and to investigate the influence of ENSO in such transmission. To accomplish the objective, a POP analysis is performed for HC anomalies in the region 10°- 30°S and 40°E - 140°E which represents the southern part of the tropical Indian Ocean.

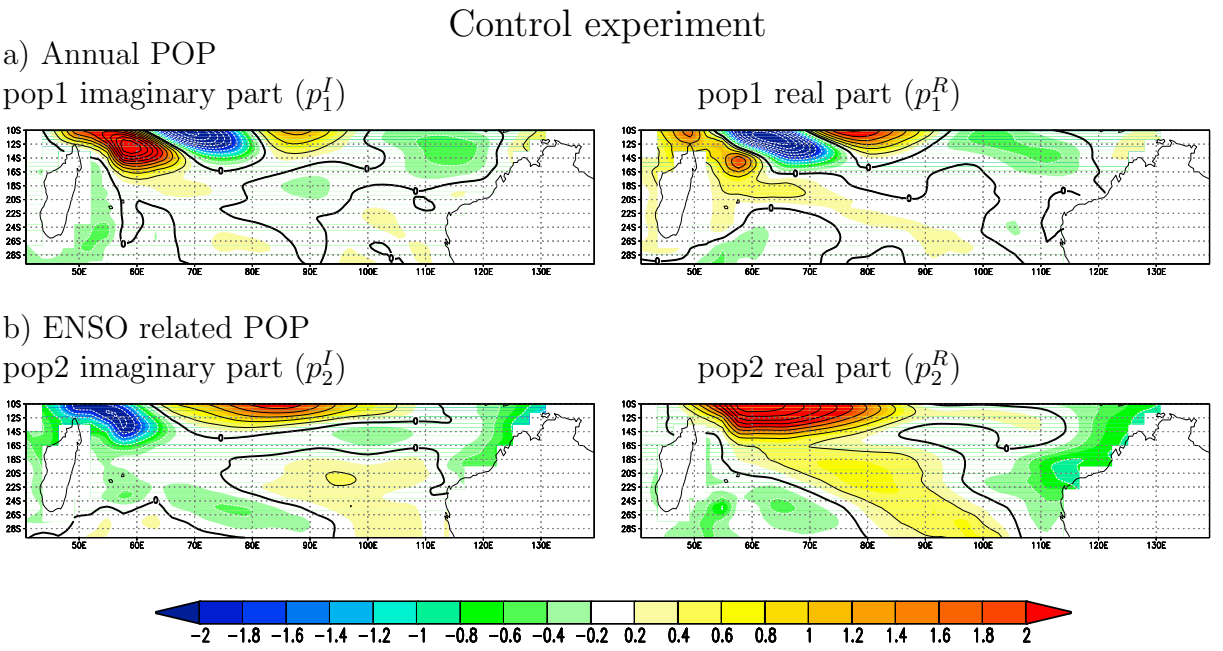

Figure 5.7: Dominant POPs of HC anomalies simulated in the control experiment. (a) pop1 and (b) pop2. Pop1 has a period of 13 months and explained variance of 7.4%. Pop2 has a period of 31.5 months and explained variance of 20.6%. The spatial domain for this POP analysis is the southern part of the tropical Indian Ocean. Contour interval is 0.2. Shaded areas denote negative values.

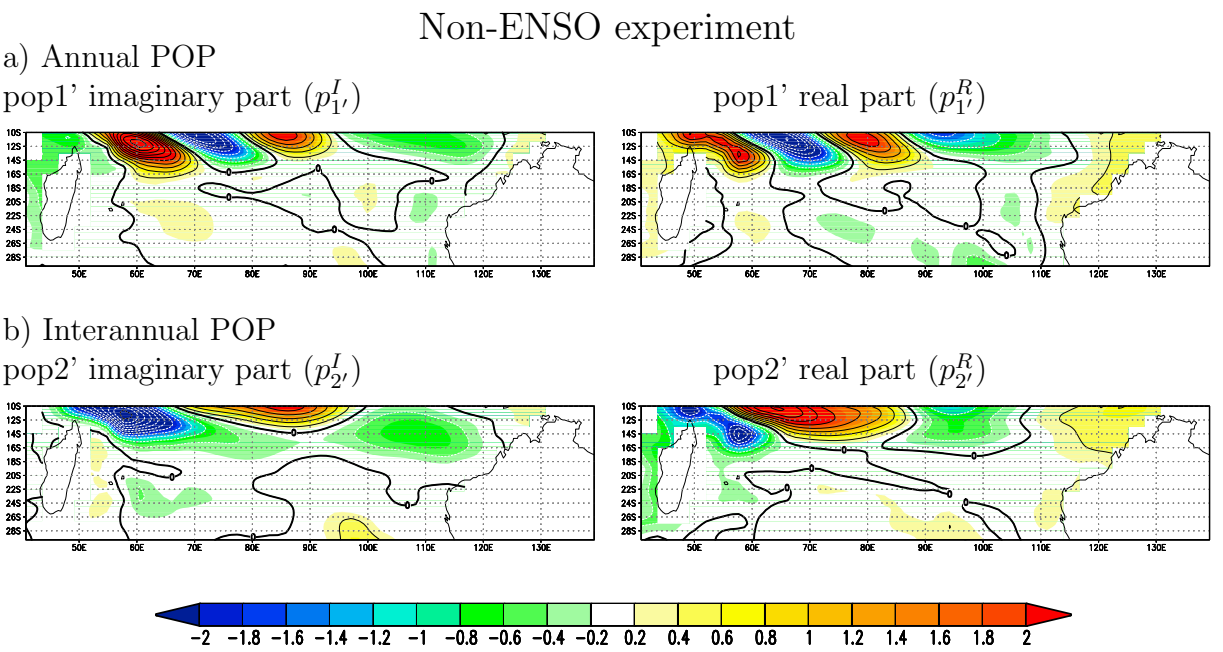

Figure 5.8: Dominant POPs of HC anomalies simulated in the non-ENSO experiment. (a) pop1' and (b) pop2'. Pop1' has a period of 11.5 months and explained variance of 7.8%. Pop2' has a period of 21 months and explained variance of 12%. The spatial domain for this POP analysis is the southern part of the tropical Indian Ocean. Contour interval is 0.2. Shaded areas denote negative values.

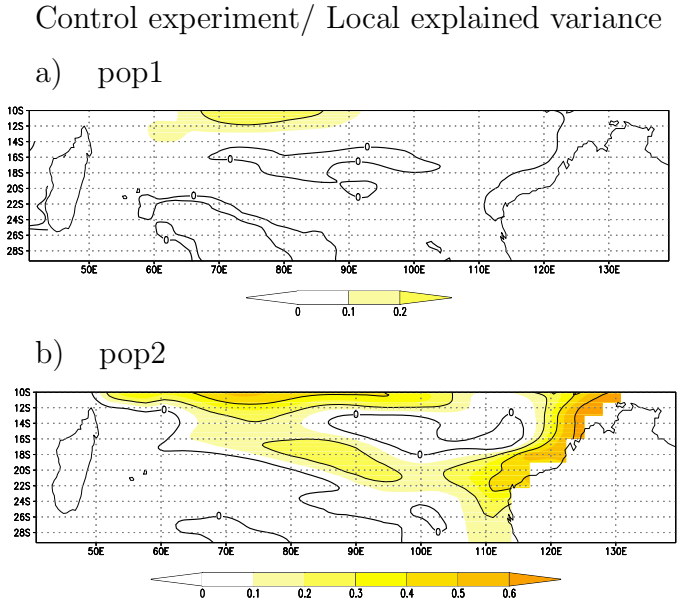

Figure 5.9: Local variance explained by the POP pairs for the control experiment shown in Fig. 5.7 (a) Local variance explained by pop1 and, (b) local variance explained by pop2. Only positive values are shown. Contour interval is 0.1.

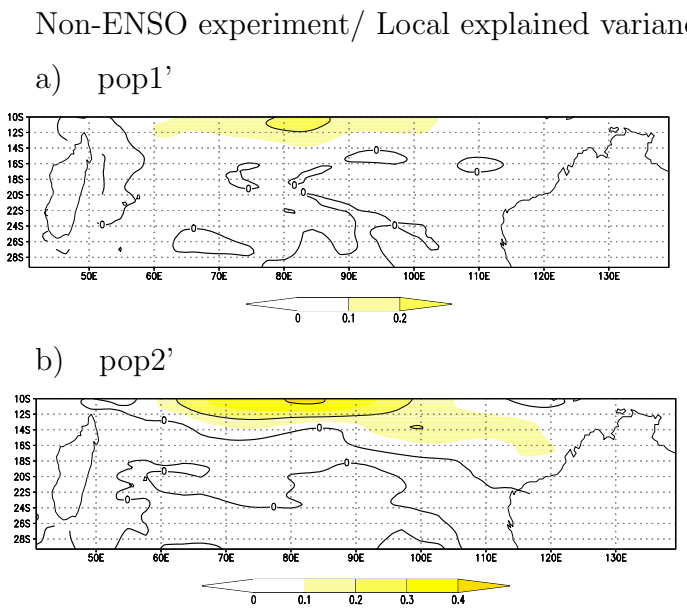

Figure 5.10: Local variance explained by the POP pairs for the non-ENSO experiment shown in Fig. 5.8 (a) Local variance explained by pop1' and, (b) local variance explained by pop2'. Only positive values are shown. Contour interval is 0.1.

For both the control and non-ENSO experiments, the POP analyses reveal two dominant Q-O modes. One mode is associated with an annual timescale and the other with an interannual timescale. The POP pairs for both experiments are reminiscent of a westward propagating signal that can be identified as Rossby wave propagation. The annual Q-O mode (Figs. 5.7a and 5.8a) explains 7.4% (7.8%) of the variance in the control experiment (non-ENSO experiment). This annual Q-O mode in the southern part of the tropical Indian Ocean was not obtained in the POP analyses for the region including also the zone north of 10°S shown in section 4.3.2 (Figs. 4.3 and 4.4). The reason for this could be that the inclusion of the zone north of 10°S gives more statistical weight to the equatorial processes and therefore to the semiannual timescale in comparison to the annual timescale.

At interannual timescales, the POP analyses for the southern part of the tropical Indian Ocean yield a Q-O mode for both experiments (Figs. 5.7b and 5.8b). However, the characteristics of the interannual POP pair in the control experiment differ from those of the POP pair in the non-ENSO experiment. For the control experiment (non-ENSO experiment), the interannual POP pair has a period of 31.5 months (21 months) that explains 20.6% (12%) of the variance. The interannual POP pair in the control experiment is associated with the ENSO phenomenon. For the control experiment, the correlation of the Niño3 index with the two time series z_2^R, z_2^I from the pop2 pair (Fig. 5.7b) amounts to 0.71 when Niño3 leads z_2^I by 5 months and to 0.71 when Niño3 leads z_2^R by 1 month. The pop2 pair for the southern part of the tropical Indian Ocean can be also associated with the pop2 for the whole tropical Indian Ocean region (Fig. 4.3b). The correlation between the two z_2^R time series for these two POPs is 0.8.

The interannual POP pair in the non-ENSO experiment (Fig. 5.7b) is associated with the pop1' pair for the whole tropical Indian Ocean (Fig. 4.4a). The spatial patterns of both interannual POP pairs look similar and the correlation between both z^R time series is 0.7.

For both experiments, the annual Q-O mode shows significant HC anomalies confined to the north of 18°S (Figs. 5.7a and 5.8a). There is an asymmetry in the zonal distribution of these anomalies. While significant HC anomalies are located west of 110°E, HC anomalies east of 110°E are up to ten times smaller. This suggest that Rossby waves are mainly produced by processes in the interior of the Indian Ocean basin at the annual

timescale. The annual Q-O mode explains up to 20% (Figs. 5.9a and 5.10a) of the variance in the region located between 10°S and 14°S and 60°E and 110°E. Thus, although the annual Q-O mode for both experiments shows some indication of coastal Kelvin waves along the northwestern coast of Australia, these coastal Kelvin waves seem not to play an important role in either the creation or the enhancement of offshore Rosby waves in the the southern part of the tropical Indian Ocean at the annual timescale.

Both the ENSO related Q-O mode in the control experiment and the interannual Q-O mode in the non-ENSO experiment (Figs. 5.7b and 5.8b) also show higher anomalies to the west of 110°E than to the east of 110°E. The interannual Q-O mode in the non-ENSO experiment explains up to 20% of the variance in the region between 10°S and 14°S and 60°E and 100°E (Fig. 5.10b). Over the same band of latitudes but east of 100°E this Q-O mode explains up to 10% of the variance. In contrast, the ENSO related mode explains more variance along the western coast of Australia: it explains up to 20% of the variance for the zone between 16°S and 26°S and up to 60% of the variance for the zone between 10°S and 16°S (Fig. 5.9b). The ENSO related mode explains up to 20% of the variance in the interior of the basin, in the region between 16°S and 21°S and 75°E and 95°E.

The spatial structure of the HC anomalies along the western coast of Australia for both the annual and interannual Q-O modes (Figs. 5.7 and 5.8) suggests that HC variability in the Indian Ocean east of 110°E could be due, at least partly, to the transmission of energy from the Pacific, due to poleward propagating coastal Kelvin waves along the western coast of Australia. The highest contribution of the coastal Kelvin waves to the HC variability along the western coast of Australia and to the generation of offshore Rossby waves is associated with ENSO (Fig. 5.9b). The interannual Q-O mode in the non-ENSO experiment (Fig. 5.10b) also shows some contribution to the HC variability in the region east of 110°E (up to 10%). In contrast, the annual mode appearing in both experiments does not explain variance east of 110°E (Figs. 5.9a and 5.10a), even though its spatial structure depicts coastal Kelvin waves propagating along the western coast of Australia. The generation of offshore Rossby waves by the coastal Kelvin waves along the western coast of Australia at interannual timescales and in particular at the ENSO timescale is not foreseen by the model predictions in Potemra (2001), which predicts the generation at timescales of the order of several months to a year.

The spatial structure of the HC anomalies in the annual and interannual Q-O modes and its zonal assimetry also suggest that although the coastal Kelvin waves can be important for the HC variability along the western coast of Australia, depending on the timescale considered, these waves are much less important for the generation of offshore Rossby waves.

In summary, it is confirmed that transmission of energy from the Pacific to the Indian Ocean occurs through coastal Kelvin waves along the western coast of Australia, as shown by Potemra (2001). In the ECHO-G model, this transmission occurs both at the annual timescale and at interannual timescales. At the annual timescale, the HC anomalies do not explain variance east of 100°E, especially not along the western coast of Australia. Thus, the coastal Kelvin waves seem not to play a significant role at the annual timescale.

At interannual timescales, the role of the waves in explaining variance along the western coast of Australia increases. The HC anomalies associated with both ENSO-independent and ENSO-related coastal Kelvin waves are locally important for the region east of 110°E. In the case of ENSO-related coastal Kelvin waves, they are also important for the generation of offshore Rossby waves in the region that stretches from 16°S to 21°S and therefore they are also important for the HC variability in the interior of the basin at these latitudes. North of 16°S, the much stronger HC anomalies away from the coast of Australia suggest that they are generated mainly by processes in the interior of the Indian Ocean.

5.6 Conclusions

In the chapter, a simple stochastic forcing model was used to explain the interannual variability in the tropical South Indian Ocean. The model is an extension of the Frankignoul et al. (1997) formulation by Sirven et al. (2002,; SFCT) and has been adapted in the present study to describe the case when wind stress curl decays at high wavenumbers as k^{-3}. In the SFCT model, the baroclinic variability is simulated using the equation for long nondispersive Rossby waves forced by wind stress curl fluctuations. The wind stress is assumed to be stochastic with a white frequency spectrum. Therefore the oceanic response represents the continuous excitation of the ocean interior by short-timescale weather fluctuations. The model considers zonally dependent forcing and dissipation and takes into

account the effect of the mean flow. At each frequency, the baroclinic response consists of a forced response plus a Rossby wave generated at the eastern boundary. The analysis presented in this chapter is statistical and based on data from the non-ENSO experiment with the ECHO-G model, wind stress data from the ERA-15 reanalysis and observational sea level data at Cocos Island. The model predicts the shape and level of the response frequency spectra and their variation with longitude and latitude.

The stochastic model predicts a spectrum with a high-frequency $w^{-\alpha}$ decay where α is a positive constant ($2 < \alpha < 3$) that levels off at low frequencies to a constant value. This is also the shape seen in the spectra for the non-ENSO experiment. Furthermore, the SFCT model correctly predicts how this spectral shape changes with longitude as a result of the varying fetch and wind stress field intensity.

Although the baroclinic response is spread over a continuum of frequencies, it can be associated with a dominant timescale that is given by the time a long baroclinic Rossby wave requires to propagate across the basin and that increases with the effective width of the basin. The stochastic model predictions for a temporally white and spatially coherent wind stress curl spectrum are also broadly consistent with the shape and level of frequency spectra of sea level measured at Cocos Island. This suggests that the stochastic model is an appropriate starting point for understanding interannual changes in the real ocean in the SIO region that are independent of ENSO in the Pacific, and in general, independent of the interannual variability in the Pacific Ocean region. On the other hand, based on the data from ERA-15 reanalysis and both experiments with ECHO-G, the present study provides evidence that the ENSO signature in the SIO region includes an oscillatory wind stress curl forcing in the east with a period corresponding to the dominant ENSO period. In summary, the results in this chapter show that basin–wide variability in the SIO heat content can be produced by two mechanisms: oscillatory forcing by ENSO-related wind stress and by temporally stochastic and spatially coherent wind stress forcing.

With respect to the transmission of energy from the tropical Pacific to the southern Indian Ocean, the results in the present study confirm that transmission occurs through coastal Kelvin waves along the western coast of Australia, as shown by Potemra (2001). In the two experiments with the ECHO-G model, this transmission occurs both at the annual timescale and at interannual timescales. Generation of offshore Rossby waves by these coastal Kelvin waves at interannual timescales and in particular at the ENSO timescale

was found, which is not foreseen by the model predictions in Potemra (2001). It was also found that at interannual timescales the coastal Kelvin waves are locally important for the region east of 110°E. In the case of ENSO-related coastal Kelvin waves, they are also important for the generation of offshore Rossby waves in the region that stretches from 16° S to 21° S. North of 16° S, the stronger HC anomalies away from the coast of Australia suggest that they are generated mainly by processes in the interior of the Indian Ocean.

Chapter 6

Concluding Remarks

6.1 Summary

6.1.1 The questions

In the past two decades it was recognized that almost all the major interannual climate fluctuations observed during the past 100 years of observational records were caused either by atmosphere–ocean, or atmosphere–ocean–biosphere interactions, and that the timescales of these fluctuations are much longer than the limits of deterministic prediction of weather. Therefore, the expectation has arisen that the expectation that the seasonal and longer time averaged atmospheric circulation can be predicted. It was also recognized that for the prediction of variability at seasonal and interannual timescales, it is necessary to predict the boundary conditions at the earth's surface such as sea surface temperature (SST), soil moisture, sea ice and snow. In particular, tropical SST anomalies have a strong effect on tropical circulation and rainfall, and can also influence the extratropical atmospheric circulation (Shukla 1993).

In view of the above–mentioned influence of SST on the tropical climate system, the assessment of the predictability of the climate fluctuations in the tropical Indian Ocean requires the investigation of the processes in the whole tropical ocean–atmosphere climate system that could lead to fluctuations of SST in the tropical Indian Ocean. Given that the El Niño–Southern Oscillation (ENSO) phenomenon involves the Indo–Pacific region, it is natural to formulate the following questions:

- What is the influence of ENSO on the Indian Ocean climate variability?

- What are the spatial and temporal characteristics of the ENSO signature in the Indian Ocean?

- What are the spatial and temporal characteristics of the ENSO independent variability?

6.1.2 The results

In this dissertation, I have used a state–of–the–art coupled ocean–atmosphere general circulation model (CGCM) as well as observational datasets and reanalysis products to propose answers to the above questions. In particular, I have analyzed results of a hierarchy of coupled model simulations. Two experiments were performed with the CGCM ECHO-G model: in one experiment, interannual ocean–atmosphere interactions have been suppressed in the tropical Pacific Ocean by setting the sea surface temperature to climatological values in this region (non-ENSO experiment), in the other experiment, interactions are allowed everywhere (control experiment). In a third coupled simulation, the ocean general circulation model is replaced by a fixed–depth mixed–layer model.

The first two coupled experiments enable the investigation of the role of ENSO in the generation of interannual variability of the tropical Indian Ocean. The last coupled experiment allows to examine the role of ocean dynamics in the generation of interannual SST variability.

Analyses of SST anomalies from the observations and from the three coupled model simulations (chapter 3) showed consistent results. In the boreal fall season, on average, the spatial ENSO signal in the tropical Indian Ocean can be seen as an east–west dipole–like pattern. The dominant SST variability in the tropical Indian Ocean is related to ENSO. Evidence of the existence of an ENSO–independent SST dipole mode with temporal oscillatory behaviour was not found. Yet, there is dipole–like SST variability in the tropical Indian Ocean that is independent of ENSO. However, this type of variability is not significantly different to an autoregressive process of the first order and does not involve ocean dynamics. This implies that the ocean is either responding passively to the atmospheric forcing by simply integrating the atmospheric noise due to the large heat capacity of the ocean's mixed–layer, in accordance with the stochastic theory of climate variability proposed by Hasselmann (1976); or that the feedback implied by the dipole–

like pattern of equatorial SST anomalies is weak and not significantly more energetic than expected from the stochastic forcing approach.

In chapter 4, it was shown that for the Rossby waves in the South Indian Ocean (SIO), the forcing mechanism is related to positive sea level pressure (SLP) anomalies in the southeastern part of the tropical Indian Ocean. The associated atmospheric circulation anomalies are southeasterlies south of the equator and equatorial easterlies. These anomalous winds can produce negative SST anomalies in the eastern Indian Ocean through equatorial and coastal upwelling and westward propagating Rossby waves that deepen the thermocline. It was also shown that ENSO produces conditions favorable for the development of Rossby waves in the SIO, since ENSO includes positive SLP anomalies in the southeastern part of the tropical Indian Ocean.

ENSO is found to be the dominant forcing for the Indian Ocean heat content (HC) variability and its signal in the Indian ocean includes both a dynamical and a thermodynamical response. Depending on the season and location it is possible to have warming either due to positive net downward heat flux (NDHF), to oceanic processes, such as downwelling Rossby waves in the SIO, or to a combination of both positive NDHF and oceanic processes. The results in this chapter suggest that ENSO forces Rossby waves in the South Indian Ocean and, in general, has an influence on the heat content variability in the tropical Indian Ocean at two different interannual timescales. Additionally, the interannual variability in the Indian Ocean was found be consistent with a cycle only if ENSO is included in the simulations.

In chapter 5, the interannual thermocline variability in the SIO and its relationship with El Niño–Southern Oscillation (ENSO) was studied. The sea surface height (SSH) response to stochastic wind stress forcing predicted by the stochastic model by Sirven et al. (2002) (SFCT model) was compared with the SSH anomalies simulated in the non-ENSO experiment. The major conclusion in this chapter is that basin–wide variability in the SIO thermocline can be produced by two mechanisms: periodic forcing by ENSO–related wind stress and by stochastic wind stress forcing.

Previous studies have shown that transmission of energy from the tropical Pacific to the southern Indian Ocean occurs through coastal Kelvin waves along the western coast of Australia. The results in this chapter confirm the ocurrence of such energy transmission. In the ECHO-G simulations this transmission occurs both at the annual timescale and at

interannual timescales. The generation of off–shore Rossby waves by these coastal Kelvin waves at interannual timescales and in particular at the ENSO timescale was found, which was not foreseen by previous model predictions.

6.2 Outlook

Much work remains before the interannual variability in the tropical Indian Ocean and the links between it and other components of the climate variability are fully understood. Several additional interesting studies could also be done with the hierarchy of CGCM simulations used in this study:

- A study of the relationship between the Indonesian throughflow (ITF), the variability at interannual and longer timescales in the Indo–Pacific Basin, and ENSO. This is relevant to address the interannual changes in surface heat flux, heat and mass transport and their relationship with the tropical climate system.
- A study of the relationship between the Indian and Asian–Australian monsoon systems, the Madden–Julian Oscillation, the variability at interannual and longer timescales in the tropical Indian Ocean region, and ENSO. This is relevant to address the forcing of coupled variability in the equatorial Indian Ocean region.

Other essential items and avenues for further research on this topic include:

- Expansion of historical data archives.
- Large uncertainties exist in data of net downward heat flux (Röske 2001). An improved analysis of this field is essential to quantify the roles of dynamics and thermodynamics in the Indian Ocean and to improve CGCMs.
- More detailed studies of the interannual climate variability in the Indian Ocean region, with emphasis on the quantitative assessment of the contributions by dynamics and thermodynamics of the mixed–layer.
- Many CGCMs have problems in simulating the climatology in the equatorial Pacific (Mechoso et al. 1995; Latif et al. 2001). Besides this, the models can have the same problems with respect to the Indian and Atlantic oceans. Thus, research to support model development and improvement is needed.

- Analysis of CGCM simulations that include increased atmospheric greenhouse gas concentrations, which is relevant to address the decadal changes in the relationship between the Indian monsoon, ENSO and the implications for the tropical Indian Ocean climate system.

Studies like these should help us to understand and predict the behaviour of the tropical climate system. Looking at the big progress achieved during the last two decades, the future seems promising.

Appendix A

Vertical thermal structure associated with the Rossby waves

Additional insight into the vertical characteristics of the Rossby waves and the variability related to them can be obtained through composite analysis of the vertical temperature anomalies. For the composite analyses in this chapter, the temperature anomalies are from the two ECHO-G experiments described in chapter 2. The composites were computed by averaging the temperature anomalies corresponding to the events for which the Soce index value is larger than 1.5 standard deviation, in particular for the positive phase of the Soce index. Composites were performed at 10°S (Figs. A.1, and A.2) and are from Jun(0) to Sep(1) with a time step of 3 months.

In agreement with the cross-correlation analyses with respect to Soce-Dec index, Figs. A.1 and A.2 show positive temperature anomalies propagating westward at 10°S starting at ∼105°E early in Summer, Jun(0), then travel to the west and can be traced to 55°E in Jun(1). Those positive anomalies go from the surface to depths below the thermocline, which is consistent with Rossby waves perturbing the thermocline.

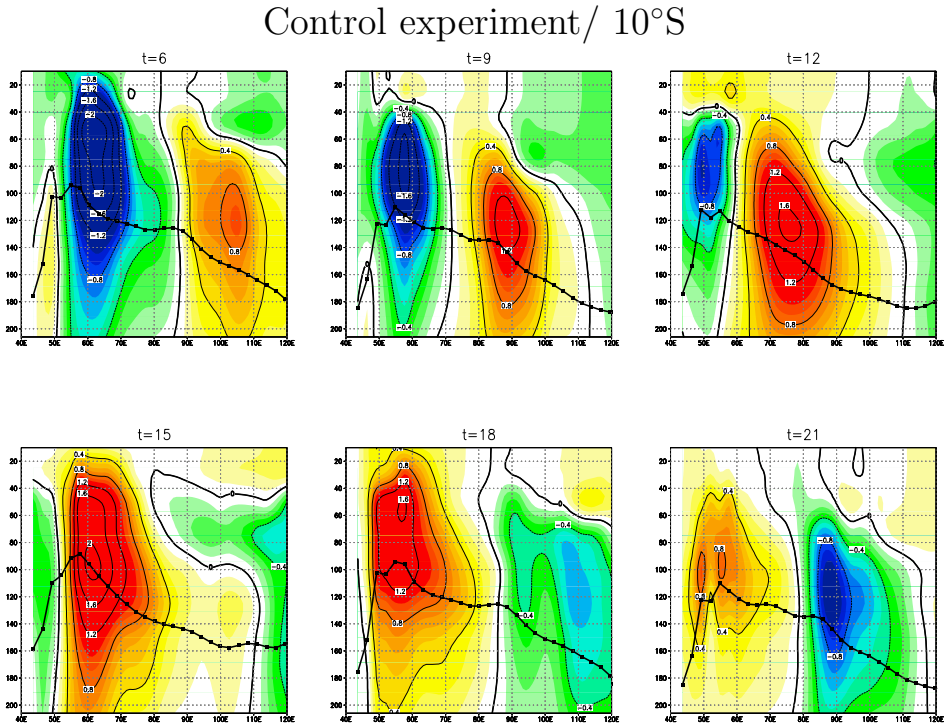

Figure A.1: Composite patterns of the vertical temperature at 10°S for the control experiment. The composites have been computed using Soce as an index of the interannual variability in the tropical Indian Ocean, and by averaging the anomalies corresponding to the events for which the Soce value is larger than 1.5 standard deviation. The black line indicates the corresponding monthly mean of the thermocline depth. The patterns are for the period between Jun(0) and Sep(1) with a time step of 3 months.

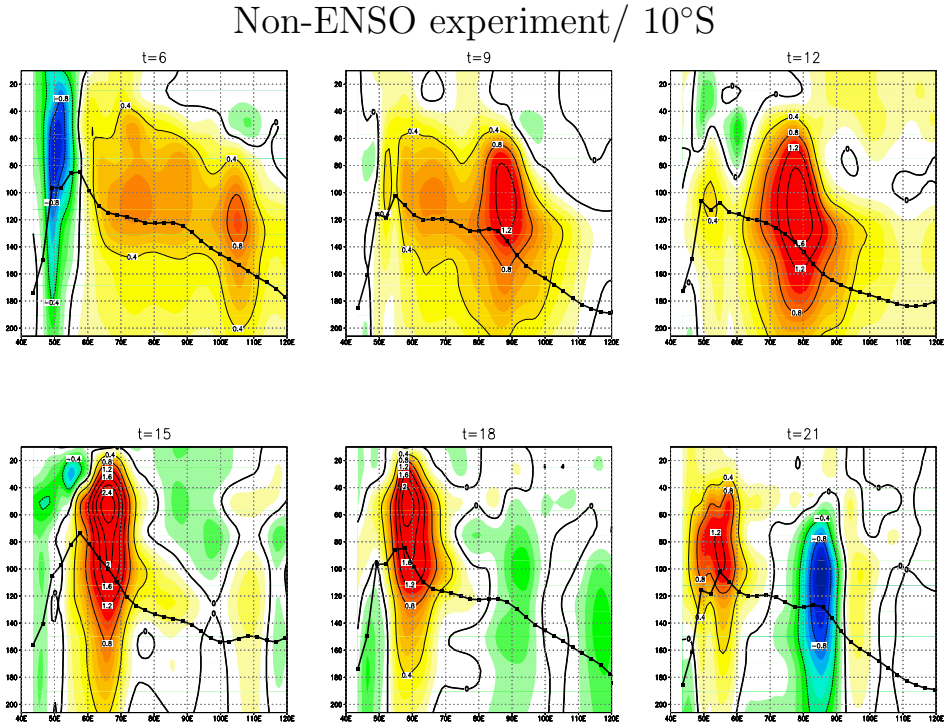

Figure A.2: Same as Fig. A.1 but for the non-ENSO experiment.

Appendix B

Local Variance Explained by the POPs

The local explained variance is the amount of variance a POP pair explains at each point as a fraction of the variance of the original data and is given by:

$$Expl.\, var. = 1 - e^2$$

where e is the relative error made by predicting the field, for example heat content (HC), using the POP pair. Since the POPs pairs are, in general, not orthogonal to each other, e^2 can be greater than 1 and the explained variance can be negative.

The percentages of local HC variance explained by the POP pairs for the two experiments are shown in Figs. B.1 and B.2. Figure B.1 shows the HC variance explained by the two interannual POP pairs found in the control experiment, pop1 and pop2, and Fig. B.2 shows the HC variance explained by the interannual POP pair found in the non-ENSO experiment, pop1'.

Control experiment:

a) Local variance explained by pop1

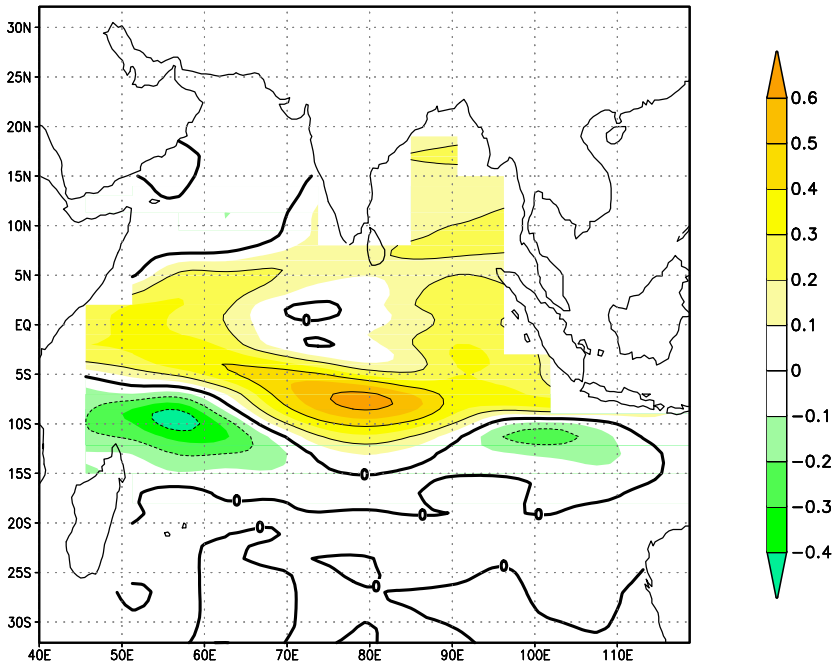

b) Local variance explained by pop2

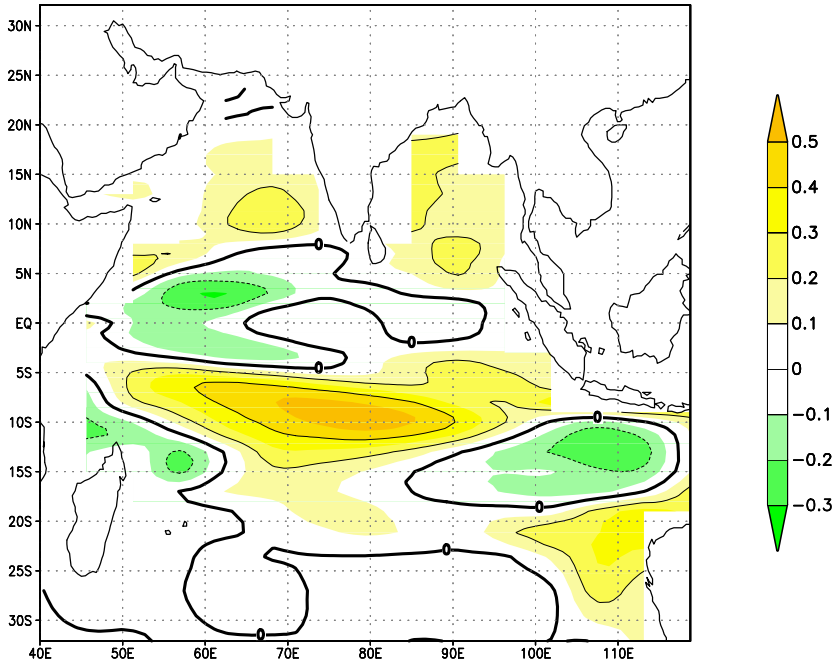

Figure B.1: Local variance explained by the POP pairs for the control experiment shown in Fig. 4.3. (a) Local variance explained by the pop1 and (b) local variance explained by the pop2.

Non-ENSO experiment:

Local variance explained by pop1'

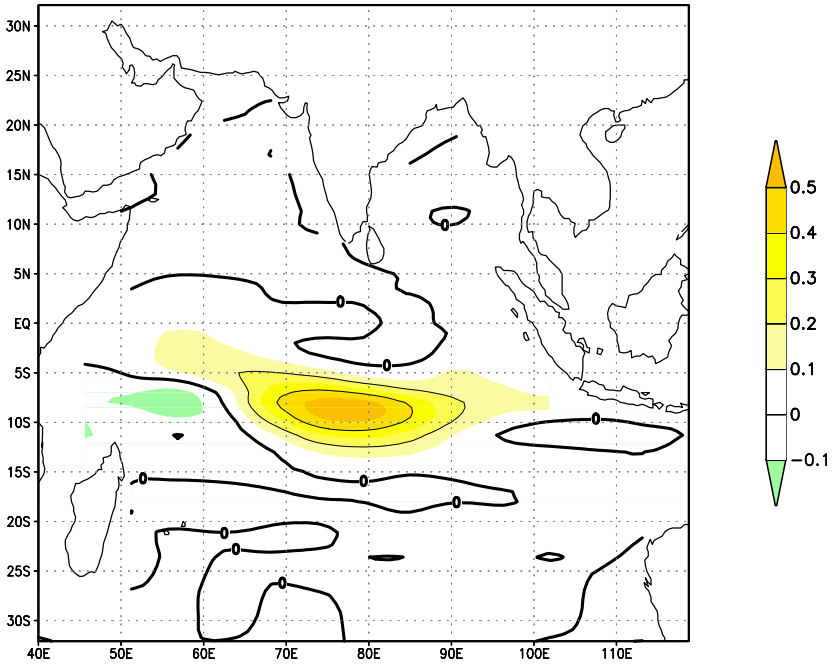

Figure B.2: Local variance explained by the pop1' pair for the non-ENSO experiment shown in Fig. 4.4.

Acknowledgments

I am very grateful to Prof. Dr. Mojib Latif, my advisor, for making this thesis possible, for his expert advise and support during this research. I am also very grateful to Prof. Dr. Klaus Hasselmann for giving me the opportunity to accomplish this Ph. D. at the Max-Planck-Institut für Meteorologie.

I am grateful to Prof. Dr. Klaus Fraedrich for the examination of this work.

The participation in several conferences and schools gave me invaluable personal and scientific experiences. I am very grateful to Prof. Dr. Mojib Latif, the Abdus Salam International Centre for Theoretical Physics (ICTP), the Nordisk Institut for Teoretisk Fysik (NORDITA) and the Helmholtz Institute for Supercomputational Physics who made possible the participation in these events. My work was supported by the scholarship program of the Instituto Colombiano para el Desarrollo de la Ciencia y la Tecnología - Francisco José de Caldas (COLCIENCIAS), the Max-Planck-Gesellschaft scholarship program for the promotion of the international scientific cooperation, the German Ocean CLIVAR programs and the German DEKLIM and PROMISE projects. All computations were performed with the computing facilities of the Deutsches Klimarechenzentrum (DKRZ).

I wish to thank all my colleagues at the Max-Planck-Institut für Meteorologie and the colleagues at the Abteilung Experimentelle Meteorologie der Universität Hamburg for the stimulating and pleasant working atmosphere. Especially, I would like to thank Drs. Stefan Hagemann, Noel Keenlyside and Reiner Schnur who carefully read and contributed to improve an earlier version of this thesis. Furthermore, I am very grateful to Frank Röske for fruitful discussions. For their kind friendship, scientific discussions and technical advice, I am very grateful to Simon Blessing, Katja Lohmann and Drs. Stefan Hagemann, Johann Jungclaus, Simon Marsland and Keith Rodgers.

Last but not least, I thank P. Stefan Seibert ofm, Margarita, Rigoberto, my mother, brother, sister, relatives and friends for the encouragement and support they continously gave me.

Bibliography

Allan, R., D. Chambers, W. Drosdowsky, H. Hendon, M. Latif, N. Nicholls, I. Smith, R. Stone, and I. Tourre: 2001, Is there an Indian Ocean dipole, and is it independent of the El Niño - Southern Oscillation? *CLIVAR Exchanges 6*, 18–22.

AVISO: 1998, *AVISO user handbook: sea level anomalies, AVI-NT-011-311-CN*. Tech. rep., CLS Space Oceanography Division, Tolouse, France, 3.1 edition.

Baquero-Bernal, A., M. Latif, and S. Legutke: 2002, On dipolelike variability of sea surface temperature in the tropical Indian Ocean. *J. Climate*, 1358–1368.

Birol, F. and R. Morrow: 2001, Sources of the baroclinic waves in the Southeast Indian Ocean. *J. Geophys. Res.*, **106**, 9145–9160.

Carton, J. A., G. Chepurin, X. Cao, and B. Giese: 2000, A simple data assimilation analysis of the global upper ocean 1950-95. Part I: Methodology. *J. Phys. Oceanogr.*, 840–858.

Chambers, D., B. D. Tapley, and R. H. Stewart: 1999, Anomalous warming in the Indian Ocean coincident with El Niño. *J. Geophys. Res.*, 7991–8014.

Chang, P., B. Wang, T. Li, and J. L.: 1994, Interactions between the seasonal cycle and the Southern Oscillation - frequency entrainment and chaos in a coupled ocean–atmosphere model. *Geophys. res. Lett*, **21**, 817–820.

Dommenget, D. and M. Latif: 2002, A cautionary note on the interpretation of EOFs. *J. climate*, 216–225.

Eckert, C. and M. Latif: 1997, Predictability of a stochastically forced hybrid coupled model of El Niño. *J. Climate*, **10**, 1488–1504.

Folland, C. K., D. Parker, A. Colman, and R. Washington: 1999, *Beyond El Niño: decadal and interdecadal climate variability*, Springer-Verlag, Berlin, chapter : Large scale modes of ocean surface temperature since the late nineteenth century. 73–102.

Frankignoul, C.: 1981, Low-frequency temperature fluctuations off Bermuda. *J. Geophys. Res.*, **86**, 6522–6528.

— 1995, *Application of statistical techniques*, Springer–Verlag, Berlin, chapter Climate spectra and stochastic climate models. 29–51.

Frankignoul, C., P. Müller, and E. Zorita: 1997, A simple model of the decadal response of the ocean to stochastic wind stress forcing. *J. Phys. Oceanogr.*, **27**, 1533–1546.

Gibson, J. K., P. Källberg, S. Uppala, A. Hernandez, A. Nomura, and E. Serrano: 1999, ECMWF Re-analysis Project report series, 1. ERA-15 description. Version 2, 73 pp.

Glantz, M. H. and N. E. Katz, R. W. Nicholls: 1991, *Teleconnections linking worldwide climate anomalies*. Cambridge Univ. Press, New York.

Goddard, L. and E. Graham: 1999, Importance of the Indian Ocean for simulating rainfall anomalies over eastern and southern Africa. *J. Geophys. Res.*, **104**, 19 099–19 116.

Guilyardi, E., J. Slingo, S. Gualdi, P. Delecluse, and A. Navarra: 2003, Understanding El Niño in coupled GCMs: the benefits of a modular approach. *Proceedings of the EGS-AGU-EUG Joint Assembly, Nice, France*, 222.

Hasselmann, K.: 1976, Stochastic climate models. Part I: theory. *Tellus*, **28**, 473–485.

— 1988, PIPs and POPs: the reduction of complex dynamical systems using principal interaction and oscillation patterns. *J. Geophys. Res.*, 11015–11021.

Hastenrath, S., A. Nicklis, and L. Greischar: 1993, Atmospheric–hydrospheric mechanisms of climate anomalies in the western equatorial Indian Ocean. *J. Geophys. Res.*, **98 (C11)**, 20 219–20 235.

Holton, J. R.: 1992, *An Introduction to Dynamic Meteorology, International Geophysics Series*. R. Dmowska and J. R. Holton, Ed., Vol. 48, Academic Press, 511 pp.

Jin, F.-F.: 1997, A theory of interdecadal climate variability of the North Pacific ocean-atmosphere system. *J. Climate*, **10**, 1821–1835.

Jin, F.-F., J. Neelin, and M. Ghil: 1996, El Niño/Southern Oscillation and the annual cycle: subharmonic frequency locking and aperiodicity. *Physica D*, **98**, 442–465.

Kalnay, E., M. Kanamitsu, R. Kistler, W. Collins, D. Deaven, L. Gandin, M. Iredell, S. Saha, G. White, J. Woollen, Y. Zhu, M. Chellia, W. Ebisuzaki, W. Higgins, J. Janowiak, K. C. Mo, C. Ropelewski, J. Wang, A. Leetmaa, R. Reynolds, R. Jenne, and D. Joseph: 1996, The NCEP/NCAR 40-year reanalysis project. *Bull. Amer. Meteor. Soc.*, 437–471.

Klein, S. A.: 1999, Remote sea surface temperature variations during ENSO: evidence for a tropical atmospheric bridge. *J. climate*, **12**, 917–932.

Latif, L., K. sperber, J. Arblaster, P. Braconnot, D. Chen, A. Colman, U. Cubash, C. Cooper, P. delecluse, D. DeWitt, L. Fairhead, G. Flato, T. Hogan, M. Ji, M. Kimoto, A. Kitoh, T. Knutson, H. Le Treut, T. Li, S. Manabe, O. Marti, C. Mechoso, G. Meehl, S. Power, E. Roeckner, J. Sirven, L. Terray, A. Vintzileos, R. Voß, B. Wang, W. Washington, I. Yoshikawa, J. Yu, and S. Zebiak: 2001, ENSIP: the El Niño simulation intercomparison project. *Clim. Dyn.*, **18**, 255–276.

Latif, M., D. Anderson, T. Barnett, M. Cane, R. Kleeman, A. Leetmaa, J. O'Brien, A. Rosati, and E. Schneider: 1998, A review of the predictability and prediction of ENSO. *J. Geophys. Res.*, **103**, 14 375–14 393.

Latif, M. and T. P. Barnett: 1994, Causes of decadal climate variability in the North Pacific/North American sector. *Science*, **266**, 96–99.

— 1995, Interactions of the tropical oceans. *J. Climate*, **8**, 952–964.

Latif, M., D. Dommenget, M. Dima, and A. Grötzner: 1999, The role of Indian Ocean sea surface temperature in forcing East African rainfall anomalies during December-January 1997/98. *J. Climate*, 3497–3504.

Lau, N.-C. and M. J. Nath: 2000, Impact of ENSO on the variability of the Asian-Australian monsoons as simulated in GCM experiments. *J. Climate*, **13**, 4287–4309.

— 2003, Atmosphere-ocean variations in the Indo-Pacific sector during ENSO episodes. *J. Climate*, **16**, 3–20.

Legutke, S. and R. Voss: 1999, The Hamburg atmosphere-ocean coupled circulation model ECHO-G. Technical Report 18, German Climate Computer Centre (DKRZ), Hamburg, 62 pp.

Marsland, S., S. Latif, and S. Legutke: 2003, Antarctic circumpolar modes in a coupled ocean-atmoshere model. *Ocean Dyn.*, in press.

Masumoto, Y. and G. Meyers: 1998, Forced Rossby waves in the southern tropical Indian Ocean. *J. Geophys. Res.*, **103**, 27 589–27 602.

McPhaden, M. J., A. J. Busalacchi, R. Cheney, J.-R. Donguy, K. S. Gage, D. Halpern, M. Ji, P. Julian, G. Meyers, G. T. Mitchum, P. P. Niiler, J. Picaut, R. W. Reynolds, N. Smith, and K. Takeuchi: 1998, The tropical ocean-atmosphere observing system: A decade of progress. *J. Geophys. Res.*, **103**, 14 169–14 240.

Mechoso, C. R., , A. W. Robertson, N. Barth, M. K. Davey, P. Delecluse, P. R. Gent, S. Ineson, B. Kirtman, M. Latif, H. Le Treut, T. Nagai, J. D. Neelin, S. G. H. Philander, J. Polcher, P. S. Schopf, T. Stockdale, M. J. Suarez, L. Terray, and J. J. Thual, O. and. Tribbia: 1995, The seasonal cycle over the tropical Pacific in coupled ocean–atmosphere general circulation models. *Mon. Wea. Rev.*, **123**, 2825–2838.

Meyers, G.: 1996, Variation of Indonesian Throughflow and El Niño – Southern Oscillation. *J. Geophys. Res*, **101 (C5)**, 12 255–12 263.

Murtugudde, R. and A. Busalacchi: 1999, Interannual variability of the dynamics and thermodynamics of the tropical Indian Ocean. *J. Climate*, **12**, 2300–2326.

Murtugudde, R., J. P. J. McCreary, and A. Busalacchi: 2000, Oceanic processes associated with anomalous events in the Indian Ocean with relevance to 1997-1998. *J. Geophys. Res.*, **105**, 3295–3306.

Neelin, D., D. S. Battisti, A. C. Hirst, F.-F. Jin, Y. Wakata, T. Yamagata, and S. E. Zebiak: 1998, ENSO theory. *J. Geophys. Res.*, 14 261–14 290.

Penland, C. and P. Sardeshmukh: 1995, The optimal growth of tropical sea surface temperature anomalies. *J. Climate*, **8**, 1999–2024.

Perigaud, C. and P. Delecluse: 1993, Interannual sea level variations in the tropical Indian Ocean from Geosat and shallow water simulations. *J. Phys. Oceanogr.*, **23**, 1916–1934.

Philander, S. G. H.: 1990, *El Niño, La Niña, and the Southern Oscillation*. Academic Press.

Potemra, J. T.: 2001, Contribution of equatorial Pacific winds to southern tropical Indian Ocean Rossby waves. *J. Geophys. Res.*, **106**, 2407–2422.

Qiu, B., W. Miao, and P. Müller: 1997, Propagation and decay of forced and free baroclinic waves in off-equatorial oceans. *J. Phys. Oceanogr.*, **27**, 2405–2417.

Rasmusson, E. and T. Carpenter: 1982, Variations in tropical sea surface temperature and surface wind fields associated with the Southern Oscillation/El Niño. *Mon. Wea. Rev.*, **110**, 354–384.

Rasmusson, E., X. Wang, and C. F. Ropelewski: 1990, The biennial component of ENSO variability. *J. Mar. Sys.*, **1**, 71–96.

Reason, C., R. Allan, J. Lindesay, and T. Ansell: 2000, ENSO and climatic signals across the Indian Ocean basin in the global context: part I, interannual composite patterns. *Int. J. Climatol.*, 1285–1327.

Reverdin, G., D. Cadet, and D. Gutzler: 1986, Interannual displacements of convection and surface circulation over the equatorial Indian Ocean. *Quart. J. Roy. Meteor. Soc*, **112**, 43–67.

Roeckner, E., K. Arpe, L. Bengtsson, M. Christoph, M. Claussen, L. Dümenil, M. Esch, M. Giorgetta, U. Schlese, and U. Schulzweida: 1996, The atmospheric general circulation model ECHAM4: model description and simulation of present-day climate. Technical Report 218, Max-Planck Institut für Meteorologie, Hamburg, 90 pp.

Ropelewski, R. W. and M. S. Halpert: 1989, Precipitation patterns associated with the high index phase of the Southern Oscillation. *J. Climate*, **2**, 594–614.

Röske, F.: 2001, An atlas of surface fluxes based on the ECMWF re-analysis –a climatological dataset to force global ocean general circulation model. Technical Report 323, Max–Planck–Institut for Meteorology, report No. 323, Max–Planck–Institut for Meteorology.

Saji, N. H., B. Goswami, P. Vinayachandran, and T. Yamagata: 1999, A dipole mode in the Indian Ocean. *Nature*, 360–363.

Schnur, R., G. Schmitz, N. Grieger, and H. von Storch: 1993, Normal modes of the atmosphere as estimated by Principal Oscillation Patterns and derived from Quasi-Geostrophic Theory. *Journal of Atmospheric Sciences*, **50**, 2386–2400.

Shukla, J., ed.: 1993, *Prediction of interannual climate variations*, volume 6 of *I: Global environmental change*. Springer-Verlag, Berlin.

Sirven, J., C. Frankignoul, G. de Coëtlogon, and V. Taillandier: 2002, Spectrum of wind-driven baroclinic fluctuations of the ocean in the midlatitudes. *J. Phys. Oceanogr.*, **9**, 104–127.

Smith, N.: 1995, Ocean data analysis and prediction experiments at BMRC. *International Workshop on Numerical Prediction of Oceanic Variations*, 197.

Smith, N., J. Blomley, and G. Meyers: 1989, The BMRC/CSIRO oceanic thermal analysis project. *Tropical Oceans - Atmosphere Newsletter*, **51**, 7–12.

Sturges, W. and B. G. Hong: 1995, Wind forcing of the Atlantic thermocline along 32°N at low frequencies. *J. Phys. Oceanogr.*, **25**, 1706–1715.

Sura, P., F. Lunkheit, and K. Fraedrick: 2000, Decadal variability in a simplified wind-driven ocean model. *J. Phys. Oceanogr.*, **30**, 1917–1930.

Terray, L., S. Valcke, and A. Piacentini: 1998, The OASIS coupler user guide, version 2.2. Technical Report TR/CMGC/98-05, CERFACS, 77 pp.

Tourre, Y. and W. White: 1997, Evolution of ENSO signals over the Indo-Pacific domain. *J. Phys. Oceanogr.*, 683–696.

Trenberth, K., G. W. Branstator, D. Karoly, A. Kumar, N.-G. Lau, and C. Ropelewski: 1998, Progress during TOGA in understanding and modeling global teleconnections associated with tropical sea surface temperatures. *J. Geophys. Res.*, **103**, 14 291–14 324.

UHSLC: 2003. The data are available from the University of Hawaii Sea Level Center website at URL: <http://ilikai.soest.hawaii.edu/uhslc/>.

Venzke, S., M. Latif, and A. Villwock: 2000, The coupled GCM ECHO-2, part II: Indian Ocean response to ENSO. *J. Climate*, **13**, 1371–1383.

von Storch, H., T. Bruns, I. Fischer– Bruns, and K. Hasselmann: 1988, Principal oscillation pattern analysis of the 30-60 day oscillation in a GCM equatorial troposphere. *J. Geophys. Res.*, **93**, 11 022–11 036.

Wallace, J. M., E. M. Rasmusson, T. P. Mitchell, V. E. Kousky, E. S. Sarachik, and H. von Storch: 1998, On the structure and evolution of ENSO–related climate variability in the tropical Pacific: lessons from TOGA. *J. Geophys. Res.*, **103**, 14 241–14 259.

Webster, P., A. Moore, J. Loschnigg, and R. Leben: 1999, Coupled ocean-atmosphere dynamics in the Indian Ocean during 1997-1998. *Nature*, 356–360.

Webster, P. J., V. O. Magaña, T. N. Palmer, J. Shukla, R. A. Tomas, M. Yanai, and T. Yasunari: 1998, Monsoons: processes, predictability, and the prospects for predictions. *J. Geophys. Res.*, **103**, 14 451–14 510.

Wolff, J.-O., E. Maier-Reimer, and S. Legutke: 1997, The Hamburg Ocean Primitive Equation Model. Technical Report 13, German Climate Computer Centre (DKRZ), Hamburg, 98 pp.

Xie, S.-P., H. Annamalai, F. A. Schott, and J. P. J. McCreary: 2002, Structure and mechanisms of South Indian Ocean climate variability. *J. Climate*.

Xu, J. S. and H. von Storch: 1990, Principal oscillation pattern - prediction of the state of ENSO. *J. Climate*, 1316–1329.

Yu, L. and M. M. Rienecker: 1999, Mechanisms for the Indian Ocean warming during the 1997-1998 El Niño. *Geophys. Res. Lett.*, **26**, 735–738.

Zorita, E., F. González-Rouco, and S. Legutke: 2002, Testing the Mann et al. (1998) approach to paleoclimate reconstructions in the context of a 1000-yr control simulation with the ECHO-G coupled climate model. *J. Climate*, **16**, 1368–1390.

Zwiers, F. W. and H. von Storch: 1995, Taking serial correlation into account in tests of the mean. *J. Climate*, **8**, 336–351.

MPI-Examensarbeit-Referenz:

Examensarbeit Nr. 1-79 bei Bedarf bitte Anfragen:
MPI für Meteorologie, Abtlg.: PR, Bundesstr. 53, 20146 Hamburg

Examensarbeit Nr. 80 November 2000	**Vertikalmessungen der Aerosolextinktion und des Ozons mit einem UV-Raman-Lidar** Volker Matthias
Examensarbeit Nr. 81 Dezember 2000	**Photochemical Smog in Berlin-Brandenburg: An Investigation with the Atmosphere-Chemistry Model GESIMA** Susanne E. Bauer
Examensarbeit Nr. 82 Juli 2001	**Komponenten des Wasserkreislaufs in Zyklonen aus Satellitendaten – Niederschlagsfallstudien-** Klepp Christian-Philipp
Examensarbeit Nr. 83 Juli 2001	**Aggregate models of climate change: development and applications** Kurt Georg Hooss
Examensarbeit Nr. 84 Februar 2002	**Ein Heterodyn-DIAL System für die simultane Messung von Wasserdampf und Vertikalwind: Aufbau und Erprobung** Stefan Lehmann
Examensarbeit Nr. 85 April 2002	**Der Wasser- und Energiehaushalt der arktischen Atmosphäre** Tido Semmler
Examensarbeit Nr. 86 April 2002	**Auswirkungen der Assimilation von Meereshöhen-Daten auf Analysen und Vorhersagen von El Niño** Sigrid Schöttle
Examensarbeit Nr. 87 Juni 2002	**Atmospheric Processes in a young Biomass Burning Plume - Radiation and Chemistry** Jörg Trentmann
Examensarbeit Nr. 88 August 2002	**Model Studies of the Tropical 30 to 60 Days Oscillation** Stefan Liess
Examensarbeit Nr. 89 Dezember 2002	**Influence of Sub-Grid Scale Variability of Clouds on the Solar Radiative Transfer Computations in the ECHAM5 Climate Model** Georg Bäuml
Examensarbeit Nr.90 Mai 2003	**Model studies on the response of the terrestrial carbon cycle to climate change and variability** Marko Scholze
Examensarbeit Nr.91 Juni 2003	**Integrated Assessment of Climate Change Using Structural Dynamic Models** Volker Barth

MPI-Examensarbeit-Referenz:

Examensarbeit Nr. 1-79 bei Bedarf bitte Anfragen:
MPI für Meteorologie, Abtlg.: PR, Bundesstr. 53, 20146 Hamburg

Examensarbeit Nr.92 Juli 2003	**Simulations of Indonesian Rainfall with a Hierarchy of Climate Models** Edvin Aldrian
Examensarbeit Nr.93 Juli 2003	**ENSO Teleconnections in High Resolution AGCM Experiments** Ute Merkel
Examensarbeit Nr.94 Juli 2003	**Application and Development of Water Vapor DIAL Systems** Klaus Ertel

---

Beginn einer neuen Veröffentlichungsreihe des MPIM, welche die vorherigen Reihen "Reports" und "Examensarbeiten" weiterführt:

„Berichte zur Erdsystemforschung" , „Reports on Earth System Science", ISSN 1614-1199
Sie enthält wissenschaftliche und technische Beiträge, inklusive Dissertationen.

Berichte zur Erdsystemforschung Nr.1 Juli 2004	**Simulation of Low-Frequency Climate Variability in the North Atlantic Ocean and the Arctic** Helmuth Haak
Berichte zur Erdsystemforschung Nr.2 Juli 2004	**Satellitenfernerkundung des Emissionsvermögens von Landoberflächen im Mikrowellenbereich** Claudia Wunram
Berichte zur Erdsystemforschung Nr.3 Juli 2004	**A Multi-Actor Dynamic Integrated Assessment Model (MADIAM)** Michael Weber
Berichte zur Erdsystemforschung Nr.4 November 2004	**The Impact of International Greenhouse Gas Emissions Reduction on Indonesia** Armi Susandi
Berichte zur Erdsystemforschung Nr.5 Januar 2005	**Proceedings of the first HyCARE meeting, Hamburg, 16-17 December 2004** Edited by Martin G. Schultz
Berichte zur Erdsystemforschung Nr.6 Januar 2005	**Mechanisms and Predictability of North Atlantic - European Climate** Holger Pohlmann
Berichte zur Erdsystemforschung Nr.7 November 2004	**Interannual and Decadal Variability in the Air-Sea Exchange of CO2 - a Model Study** Patrick Wetzel


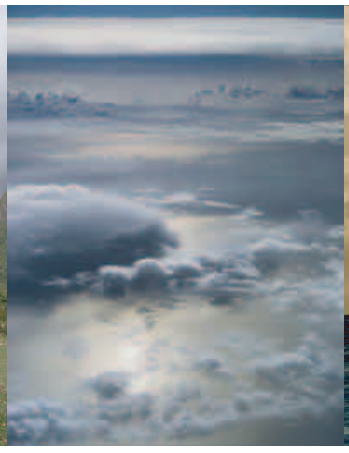


ISSN 1614-1199